ESA/SCI(2018)1
December 2018

SMILE

Solar wind Magnetosphere Ionosphere Link Explorer

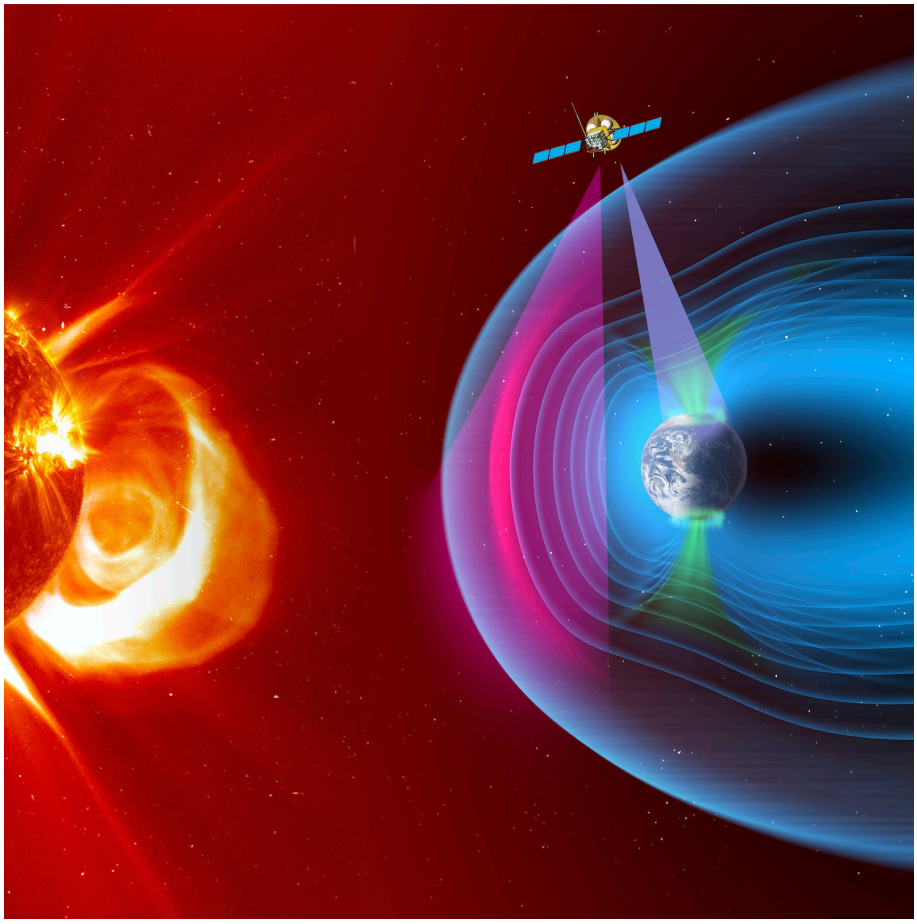

Definition Study Report

European Space Agency

The front page shows a sketch of the solar wind – magnetosphere interaction and the field of views of the Soft X-ray Imager (pink) and the Ultra-Violet Imager (purple). The Light Ion Analyser and the flux-gate Magnetometer measure in-situ the ion distribution function and the magnetic field (Credit: ESA/ATG medialab).

SMILE Definition Study – Mission Summary	
Cosmic Vision Theme	How does the solar system work?
Key scientific goals	Investigate the dynamic response of the Earth's magnetosphere to the solar wind impact via simultaneous in situ solar wind/magnetosheath plasma and magnetic field measurements, X-ray images of the magnetosheath and magnetic cusps, and UV images of global auroral distributions. Imaging of the magnetosphere and auroras for more than 40 hours continuously.
Top level science questions	• What are the fundamental modes of the dayside solar wind/magnetosphere interaction? • What defines the substorm cycle? • How do Coronal Mass Ejection (CME)-driven storms arise and what is their relationship to substorms?
Payload	• LIA (Light Ion Analyser) is a top-hat analyser for detection of protons and alphas. Energy range 50 eV-20 keV. • MAG (Magnetometer) is a flux-gate magnetometer with two sensors on a 3m boom. • SXI (Soft X-ray Imager) is a lobster-eye telescope that employs CCD detectors to image X-rays with energies from 0.2-2.5 keV within a wide 26.5 x 15.5 degree field-of-view (FOV). • UVI (UltraViolet Imager) is a four mirror telescope imaging ultraviolet emissions with wavelengths from 155 to175 nm using a CMOS detector.
Description of Spacecraft	3-axis stabilised Mass (dry): ~ 679 kg (Platform: 547 kg, Payload module: 132 kg) Mass (with propellant): 2200 kg Dimensions at launch: 2.7 m (diameter) x 3.5 m (Z) Dimensions in orbit: 4.7 m (X) × 9.8 m (Y) × 3.5 m (Z) S-band and X-band Telemetry rate: 36 Gbit/orbit downlink (X-band)
Mission Profile	Baseline orbit: 1 x 20 Earth radii, 70-98° inclination Launch: November 2023 Launcher: As primary passenger on Vega-C or co-passenger on Ariane 62 Nominal mission duration: 3 years
Programmatic	ESA is responsible for the payload module, and two instruments (SXI and UVI provided by the ESA Member States and CSA), spacecraft test facilities, launcher, launch campaign, part of the ground stations and science operations CAS is responsible for the platform, Spacecraft testing, two instruments (MAG and LIA) and mission and science operations

Foreword

SMILE is turning into reality an aspiration, almost a dream, which a number of scientists and engineers developed and proposed over some years (MagEX, STORM, AXIOM and AXIOM-C): imaging in soft X-rays the invisible magnetic environment of the Earth, taking advantage of what had been discovered serendipitously while looking away from the Earth, that comets produce soft X-rays travelling through the solar wind. The SMILE payload complements X-ray imaging with enhanced Ultra-Violet auroral imaging and in-situ plasma and magnetic field measurements to provide a powerful combination for studying the Sun-Earth connection.

This is a facet of SMILE that makes it unique: applying well established astrophysical processes and the techniques developed to study them in extra-terrestrial targets, to the local magnetic environment of our own planet. A consequence of this, and of the combination of SMILE's payload elements for remote observing and in situ measuring, is the need to bring together communities that have been travelling mostly very separate ways this far: astrophysics, planetary science and space plasma physics. Interdisciplinary research has become very popular in recent times, with the promise that it will encourage lateral thinking and produce more substantial results. SMILE is the archetype of this; we are learning each other's science, instrument and data analysis characteristics and requirements, with the well founded expectation that the final result will be much more than the sum of the individual parts. Another facet almost unique of SMILE (there has been at least one precedent, similar to some extent, Double Star) is the determination of ESA and CAS to develop this as a joint mission from beginning to end. This has added a novel and enticing dimension which opens opportunities to both agencies and to the national teams providing the instruments of coming into contact with, of comparing, learning and contributing different ways of thinking and preparing for going to and operating in space.

Following a call issued jointly by ESA and the Chinese Academy of Science (CAS) in January 2015, SMILE was recommended in June 2015 as candidate for a collaborative science mission. ESA and CAS carried out an internal study, which set the basis for the definition of the mission science requirements, the system requirements for satellite and payload, and the preparation of the Invitation to Tender (ITT) for the ESA industrial activities. A few months later, in November 2015, the ESA Science Programme Committee selected the SMILE mission.

During 3 years the study was conducted with ESA, CAS, three European industrial contractors and the Science Study Team (SST). This report summarizes the SMILE definition study. It describes the mission architecture, including the space and ground elements, that fulfils the science requirements and therefore allows to achieve the science objectives presented in the SMILE original proposal.

The SMILE study team

Authorship, acknowledgements

This report has been prepared by members of the SMILE science study team listed below.

SMILE SST		
Name	*Affiliation*	*City, Country*
Graziella Branduardi-Raymont (Mission Co-PI)	MSSL/UCL	Holmbury St. Mary, UK
Chi Wang (Mission Co-PI)	NSSC/CAS	Beijing, China
Lei DAI (LIA PI)	NSSC/CAS	Beijing, China
Eric Donovan (UVI PI)	Calgary University	Calgary, Canada
Lei LI (MAG PI)	NSSC/CAS	Beijing, China
Steve Sembay (SXI PI)	Leicester University	Leicester, UK

The ESA and CAS teams supporting the activities are composed by:

ESA study team		
David Agnolon (Study Manager)	ESA/ESTEC	Noordwjik, The Netherlands
C. Philippe Escoubet (Study Scientist)	ESA/ESTEC	Noordwjik, The Netherlands
Walfried Raab (Payload Manager))	ESA/ESTEC	Noordwjik, The Netherlands
Chris Runciman (Payload Module Manager)	ESA/ESTEC	Noordwjik, The Netherlands
Fabio Giannini (Payload Engineer)	ESA/ESTEC	Noordwjik, The Netherlands
Kate Symonds (Mission Operations Manager)	ESA/ESOC	Darmstadt, Germany
Harri Laakso (Science Operations Manager)	ESA/ESAC	Villafranca, Spain
CAS study team		
Jing LI (Study Manager)	NSSC/CAS	Beijing, China
Jianhua ZHENG (Assistant of SMILE Chief Engineer)	NSSC/CAS	Beijing, China
Jizhou TONG (Vice System Engineer of GSS)	NSSC/CAS	Beijing, China
Zhencai ZHU (Commander of SMILE Satellite System Vice Leader of IAMC)	IAMC/CAS	Shanghai, China
Wen CHEN (Vice System Engineer of SMILE Satellite System, IAMC)	IAMC/CAS	Shanghai, China
Xiaocheng ZHU (Satellite Engineer)	IAMC/CAS	Shanghai, China
Lei HUANG (Engineer of CCC)	CCC	Beijing, China
ESA Coordinators		
Luigi Colangeli	ESA/ESTEC	Noordwjik, The Netherlands
Arvind Parmar	ESA/ESTEC	Noordwjik, The Netherlands

We also acknowledge the contribution of (by alphabetical order): M. Adamovic (CSA, Canada), M. Berthomier (LPP, France), J. A. Carter (University of Leicester, Department of Physics and Astronomy, UK), M. Collier

(NASA Goddard Space Flight Center, USA), H. K. Connor (University of Alaska Fairbanks, USA, Andrew Dimmock (IRF-U, Sweden), O. Djazovski (CSA, Canada), J. P. Eastwood (The Blackett Laboratory, Imperial College London, UK), G. Enno (University of Calgary, Canada), D. Kataria (Mullard Space Science Laboratory, UK), K. Kuntz (JHU/APL, USA), Tony Lui (JHU/APL, USA), J. Loicq (CSL, Belgium), A. Masson (ESA/ESAC, Spain), J. Manuel (CSA, Canada), T. Piekutowski (CSA, Canada), A. M. Read (University of Leicester, Department of Physics and Astronomy, UK), A. Samsonov (MSSL, UK), J.K. Shi (National Space Science Center, CAS, China), D. G. Sibeck (NASA Goddard Space Flight Center, USA), E. L. Spanswick (University of Calgary, Canada), T. SUN (National Space Science Center, CAS, China), B. Walsh (Boston University, USA), F. WEI (National Space Science Center, CAS, China), D. Zhao (ESA/ESTEC, Netherlands)

Table of contents

1 EXECUTIVE SUMMARY 8
2 SCIENTIFIC OBJECTIVES 10
2.1 Introduction 10
2.2 Global measurements of the Solar Wind-Magnetosphere Interaction 12
2.3 Open science questions 14
2.3.1 What are the fundamental modes of the dayside solar wind/magnetosphere interaction? 14
2.3.2 What defines the substorm cycle? 16
2.3.3 How do CME-driven storms arise and what is their relationship to substorms? 19
2.4 A novel method to image the magnetosphere 20
2.5 Modeling solar wind-magnetosphere interaction and field of view 23
2.5.1 MHD model 23
2.5.2 Boundary tracing 24
2.5.2.1 Tangential direction method 25
2.5.2.2 Boundary Fitting Approach 26
2.5.3 Magnetopause model comparison and propagation time through magnetosheath 27
2.5.4 SXI field-of-view simulation 28
3 SCIENTIFIC REQUIREMENTS 31
3.1 Science requirements 31
3.2 Mission requirements 33
4 PAYLOAD AND PERFORMANCE 35
4.1 The Soft X-ray Imager: SXI 35
4.1.1 SXI Instrument Description 35
4.1.1.1 SXI Telescope 35
4.1.1.2 Thermal Control System 36
4.1.1.3 Front End Electronics Assembly 36
4.1.1.4 Back End Electronics Assembly 36
4.1.2 SXI System Architecture 36
4.1.3 SXI Instrument Design 36
4.1.3.1 Optic Assembly and Straylight Baffle 36
4.1.3.2 Detector Plane Assembly and CCD Detectors 37
4.1.3.3 Radiation Shutter 37
4.1.3.4 Thermal Control System 37
4.1.3.5 Front End Electronics 37
4.1.3.6 Back End Electronics 38
4.1.4 SXI Interfaces and Resources 38
4.1.4.1 Mass 38
4.1.4.2 Power 38
4.1.5 SXI Instrument Performance 38
4.2 The Ultraviolet Imager: UVI 40
4.2.1 UVI Instrument Description 40
4.2.1.1 UVI Camera Unit (UVI-C) 40
4.2.1.2 UVI Electronics Box (UVI-E) 41
4.2.2 UVI System Architecture 41
4.2.3 UVI Instrument Design 42
4.2.3.1 Optics module 42
4.2.3.2 Detector module 43
4.2.3.3 Straylight baffle and aperture cover 43
4.2.3.4 UVI-C thermal control 43
4.2.3.5 UVI-C electronics backpack 43
4.2.3.6 UVI-E electronics 44
4.2.4 UVI Interfaces and Resources 44

4.2.4.1 Mass 44
4.2.4.2 Power 44
4.2.5 UVI Instrument Performance 44
4.2.5.1 Instrument design parameters 45
4.2.5.2 Modelled instrument performance 46
4.3 The Magnetometer: MAG 47
4.3.1 MAG Instrument Architecture 47
4.3.2 MAG Instrument Design 47
4.3.2.1 Fluxgate sensor 47
4.3.2.2 Read-out chain 48
4.3.2.3 Electronics box 48
4.3.2.4 Deployable boom 48
4.3.3 MAG Interfaces and Resources 49
4.3.3.1 Interfaces 49
4.3.3.2 Instrument budgets 49
4.3.4 MAG Instrument Performance 50
4.3.4.1 Error sources and measurement accuracy 50
4.3.4.2 Resolution 50
4.4 The Light Ion Analyzer: LIA 51
4.4.1 LIA Instrument Architecture 51
4.4.2 LIA Instrument Design 51
4.4.2.1 LIA sensor 51
4.4.2.2 LIA electronics box 52
4.4.3 LIA Interfaces and Resources 53
4.4.3.1 Interfaces 53
4.4.3.2 Instrument budgets 53
4.4.4 LIA Instrument Performance 54
5 MISSION DESIGN 56
5.1 Mission description 56
5.2 Spacecraft description 57
5.2.1 Spacecraft Design Drivers 58
5.2.2 SMILE Spacecraft at System Level 58
5.2.2.1 Mass Budget 59
5.2.2.2 Power Budget 60
5.2.2.3 Pointing Budget 60
5.2.3 The Platform 61
5.2.4 The Payload Module (PLM) 62
5.3 Integration and testing 63
6 GROUND SEGMENT 64
6.1 Ground Segment Architecture 64
6.2 Ground Segment Functional Areas and Operational Responsibilities 65
6.2.1 CAS Ground Segment 65
6.2.1.1 Ground Support System (GSS) 65
6.2.1.1.1 Mission Centre (MC) 65
6.2.1.1.2 Chinese Space Science Data Centre (CSSDC) 65
6.2.1.1.3 CAS X-band ground stations 65
6.2.1.2 Science Application System (SAS) 65
6.2.1.2.1 Strategic Planning and Operation Support Subsystem (SPOSS) 65
6.2.1.2.2 Chinese Science Operation Subsystem (CSOS) 65
6.2.1.2.3 Chinese Science Data Processing Subsystem (CSDPS) 65
6.2.1.3 Chinese Control Centre (CCC) 66
6.2.2 ESA Ground Segment 66
6.2.2.1 European Space Operations Centre (ESOC) 66

6.2.2.2 European Space Astronomy Centre (ESAC) 67
6.2.2.2.1 Science Operation Centre (SOC) 67
6.2.2.2.2 ESAC Science Data Centre (ESDC) 67
6.3 Overview of Operational Processes 67
6.3.1 Downlink processes. 67
6.3.1.1 X-band Downlink 67
6.3.1.2 S-band Downlink 68
6.3.2 Uplink process 68
6.3.3 Archive process 69
7 MANAGEMENT 70
7.1 Procurement scheme 70
7.2 Project management 72
7.2.1 ESA management 72
7.2.2 CAS management 72
7.3 Programme participation 73
7.4 Science management 73
7.5 Schedule 74
7.6 Data rights 75
8 COMMUNICATION AND PUBLIC ENGAGEMENT 76
9 REFERENCES 78
10 LIST OF ACRONYMS 81
11 ANNEX 1 82

1 Executive summary

ESA's Cosmic Vision 2015-2025 programme addresses four questions, established as being highest on the agenda of European scientific space research. One of these, 'How does the solar system work?', expresses our need to understand how the Sun creates the heliosphere, and how the planets interact with the solar wind and its magnetic field. This is not just a matter of scientific curiosity – it also addresses a clear and pressing practical problem. As our world becomes ever more dependent on complex technology – both in space and on the ground – society becomes more exposed to the vagaries of space weather, the conditions on the Sun and in the solar wind, magnetosphere, ionosphere and thermosphere that can influence the performance and reliability of technological systems and endanger human life and health.

The interaction between the solar wind and Earth's magnetosphere, and the geospace dynamics that result, comprise a fundamental aspect of heliophysics. Understanding how this vast system works requires knowledge of energy and mass transport, and a comprehension of coupling between regions and between plasma and neutral populations. Missions such as Cluster, THEMIS, Swarm, and now Magnetospheric Multi-Scale provide in situ observations with which we drill into the fundamental microscale processes that enable transport and coupling. In situ instruments on a fleet of solar and solar wind observatories now provide unprecedented observations of the external drivers. However, we are still unable to quantify the global effects of those drivers, including the conditions that prevail throughout geospace. This information is the key missing link for developing a complete understanding of how the Sun gives rise to and controls Earth's plasma environment.

Here we describe a novel self-standing mission dedicated to observing solar wind-magnetosphere coupling via simultaneous in situ solar wind/magnetosheath plasma and magnetic field measurements, X-Ray images of the magnetosheath and magnetic cusps, and UV images of global auroral distributions defining system-level consequences. The Solar wind Magnetosphere Ionosphere Link Explorer (SMILE) will complement all solar, solar wind and in situ magnetospheric observations, including both space- and ground-based observatories, to enable the first-ever observations of the full chain of events that drive the Sun-Earth connection.

Remote sensing of the cusps and magnetosheath with X-ray imaging is now possible thanks to the relatively recent discovery of solar wind charge exchange (SWCX) X-ray emission, first observed at comet Hyakutake (e.g. Lisse et al., 1996; Cravens 1997), and subsequently found to occur in the vicinity of the Earth's magnetosphere. Charge exchange is now recognised as a ubiquitous mechanism that produces X-rays throughout the Universe, and the approach proposed here allows established astronomical techniques to be applied to our own planet. In this report we describe how an appropriately designed X-ray telescope, SMILE's Soft X-ray Imager (SXI), located in a highly-inclined, high-apogee elliptical orbit, can be used to determine the nature of the dayside solar wind-magnetosphere interaction from conditions prevailing at the Earth's bow shock, magnetopause, and cusps.

Both ground-based networks and space-borne instruments have long been used to sense the system-level magnetospheric dynamics via time sequences of auroral images. SMILE's high-heritage Ultra-Violet Imager (UVI) will elucidate the consequences of the dayside interactions observed by LIA, MAG and SXI. It will provide global auroral images from one hemisphere with the temporal and spatial resolution needed to identify specific responses to dayside processes, and the sensitivity necessary to identify the polar cap boundary at all magnetic local times. The focus on dayside interactions, and need to identify the polar cap boundary at all local times, mean that these images must capture the aurora even in sunlight. For this, the UVI will employ new filter technologies and an innovative four-mirror telescope design to obtain state-of-the-art UV images. Just like meteorologists studying terrestrial weather, space physicists require in situ ground observations, numerical models, data assimilation, and remote sensing (including imaging). SMILE will provide the in situ solar wind drivers and remote sensing measurements needed to run and validate global models for solar wind-magnetosphere interactions. Consequently, this mission will play a key role in developing our ability to model and ultimately predict solar storms effects on our Earth's environment.

SMILE is a novel space mission that will revolutionise magnetospheric physics by providing simultaneous images and movies of the magnetopause, cusps, and auroral oval for up to 40 hours per orbit continuously using state-of-the-art detection techniques.

The prime science questions of the SMILE mission are:
Q1: What are the fundamental modes of the dayside solar wind/magnetosphere interaction?
Q2: What defines the substorm cycle?
Q3: How do coronal mass ejection-driven storms arise and what is their relationship to substorms?

Mission Profile: The spacecraft will be launched on a VEGA-C or shared Ariane 62 rocket and it will perform a series of manoeuvres to reach its final highly-inclined (>70°), high apogee (20 R_E), elliptical orbit. This will allow the mission to collect more than 40h of continuous cusp/magnetosheath and auroral imaging per 51h orbit. The nominal mission duration is 3 years.

Model Payload: The model payload consists of a wide field Soft X-ray Imager (SXI), an auroral Ultra-Violet Imager (UVI), a Light Ion Analyser (LIA) to measure solar wind ion distributions and a magnetometer (MAG) to measure interplanetary, magnetosheath, and magnetospheric magnetic fields. The instruments have heritage from many space plasma and X-ray observatory missions, including Cluster, IMAGE, Polar, and Solar Orbiter, and XMM-Newton, and will re-use on-going developments on CHEOPS and PLATO missions.

Spacecraft: SMILE will be three-axis stabilised, so the SXI and UVI instruments can continuously point towards their magnetospheric and auroral targets. The spacecraft will include a payload module that will operate the instruments and collect their data and a platform that will provide the power, attitude and orbital manoeuvres necessary to fulfil the mission.

Operations: The SMILE ground segment will be shared by CAS and ESA. CAS will operate the spacecraft and perform science operations for the instruments. CAS and ESA will collect data using their respective ground-stations and will archive all instrument data for further distribution to the user community.

Communication and Public Engagement: The key obstacle to effective communication of research in solar-terrestrial physics is that it involves the study of many processes that are complicated and essentially invisible to the naked eye. SMILE has the potential to revolutionise the general understanding of this area of science by providing 'X-ray' images of the magnetospheric bubble shielding our Earth from inclement solar wind conditions. A comprehensive communication and outreach programme is being prepared to take full advantage of these novel data.

2 Scientific objectives

2.1 Introduction

Heliophysicists seek to understand, and model, the processes governing the flow of solar wind mass, energy, and momentum through the Sun-Solar Wind-Magnetosphere-Ionosphere system. With this knowledge in hand, they will be able to forecast geomagnetic storms, the most hazardous space weather events in the near-Earth environment. Storms enhance the fluxes of energetic particles within the magnetosphere to levels capable of harming spacecraft electronics, drive powerful currents into the ionosphere that cause surges in electrical power line transmission, enhance exospheric densities and therefore drag on low-latitude spacecraft, and modify ionospheric densities in ways that severely impact GPS navigation and satellite communication.

The Earth's magnetic field extends into space, where its interaction with the super-Alfvénic and supersonic solar wind plasma leads to the formation of the magnetosphere. Our experimental knowledge of the magnetosphere has developed thanks to a rich history of increasingly capable satellite missions, exemplified in Europe by the four satellite Cluster mission (Escoubet et al., 2001), the Chinese-European Double Star project (Liu et al., 2005), the US Time History of Events and Macroscale Interactions during Substorms (THEMIS) (Angelopoulos et al., 2008), Van Allen probes (Mauk et al., 2013) and the Magnetospheric Multi-Scale (MMS) mission (Burch et al., 2015), and the Japanese Geotail (Mukai et al., 1994) and Arase-ERG (Miyoshi et al., 2018) missions. These missions, like their predecessors, have explored the magnetosphere in situ, making incredibly precise local measurements of the various plasma processes that control the behaviour of the magnetosphere.

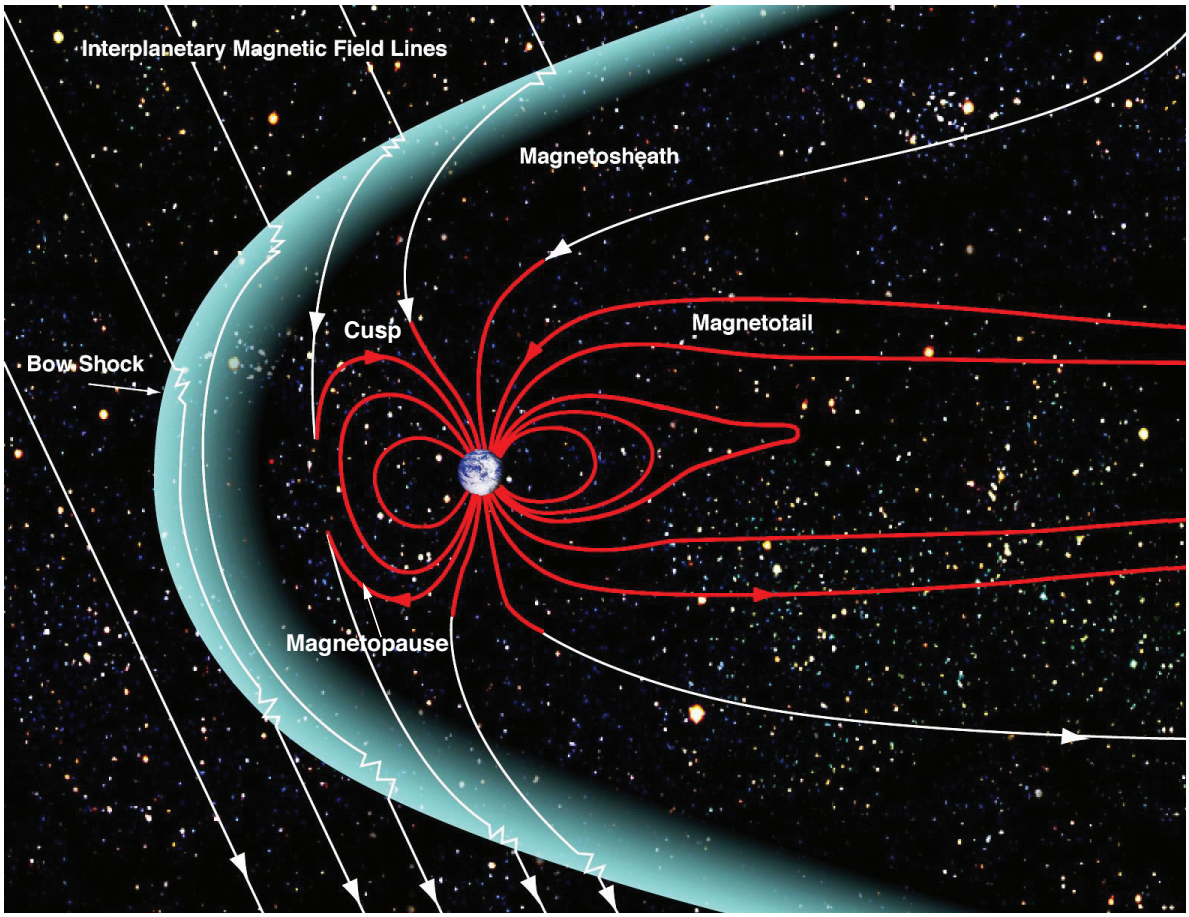

Figure 1: The Earth's magnetosphere. The magnetopause (at the junction of white and red field lines) represents the outer boundary of the magnetosphere, and is compressed on the dayside and elongated into a tail on the nightside. The bow shock is where the solar wind is decelerated and heated. The magnetosheath is the region located between the bow shock and magnetopause. The polar cusps are the polar regions where solar wind can enter directly in the magnetosphere.

When directed southward, interplanetary magnetic field lines (white) reconnect with Earth's magnetic field lines (red) on the dayside of the Earth (adapted from NASA/Goddard/Aaron Kaase)

Satellites working in situ have identified and explored the different 'working parts' of the magnetosphere, showing that the solar wind flow compresses the sunward side of the magnetosphere but drags the nightside out into a long magnetotail. As shown in Figure 1, a collisionless bow shock stands upstream from the magnetopause in the supersonic solar wind. The shocked solar wind plasma flows around the magnetosphere through the magnetosheath. A relatively sharp transition from dense, shocked, solar wind plasmas to tenuous magnetospheric plasmas marks the magnetopause. High latitude cusps denote locations where field lines divide to close either in the opposite hemisphere or far down the magnetotail. Weak field strengths within the cusps provide an opportunity for solar wind plasma to penetrate deep into the magnetosphere, all the way to the ionosphere.

The position and shape of the magnetopause change constantly as the Earth's magnetosphere responds to varying solar wind dynamic pressures and interplanetary magnetic field orientations. The solar wind can be interrupted by large, fast-moving bursts of plasma called interplanetary coronal mass ejections, or CMEs. When a CME impacts the Earth's magnetosphere, it temporarily deforms the Earth's magnetic field, perturbing its direction and strength, and inducing large electrical currents; this is called a geomagnetic storm and it is a global phenomenon. Figure 2 shows the magnetosphere before (left panel) and during (right panel) a geomagnetic storm. The increase of solar wind dynamic pressure during the storm compresses the magnetosphere to less than half (right panel) of its normal size (left panel). Electric currents reaching the ionosphere and producing strong auroras are also greatly enhanced during the storm (right-bottom insert on right panel).

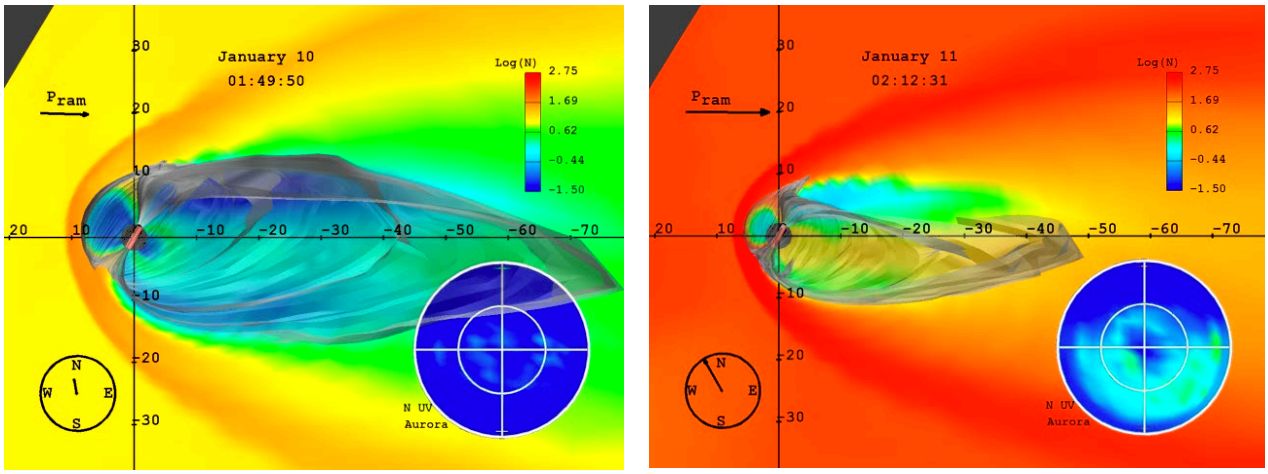

Figure 2. Magnetohydrodynamics (MHD) model simulation during a storm on 10 January 1997. Left: the magnetosphere before the storm and right: the magnetosphere during the storm. The plasma density is shown in colour in the background and the Earth's magnetic field is shown in grey. The solar wind pressure strength is indicated by the length of the P_{ram} arrow and the direction of the interplanetary magnetic field is shown in the left-bottom insert. The inserts on the right-bottom corners show the electric currents reaching the ionosphere and simulating northern hemisphere auroras (after Goodrich et al., 1998).

Due to its inherent complexity, and cross-system coupling over spatial and temporal scales ranging from the very large to the very small, the coupled magnetosphere-ionosphere system exhibits strikingly non-linear dynamic behaviour in response to the constantly changing solar wind, ultimately driven by the Sun. A basic component of magnetospheric activity is thought to be the geomagnetic substorm, where intervals of dayside reconnection under southward interplanetary magnetic field (IMF) conditions remove magnetic flux from the dayside magnetosphere and add this flux (and corresponding magnetic energy) to the magnetotail lobes (illustrated in Figure 3). This stored energy is intermittently and explosively released, and is associated with bright auroral displays in polar regions (Angelopoulos et al., 2008). The substorm is thus a non-linear global system response.

A significant breakthrough in magnetospheric physics came in the form of global auroral imaging, most notably provided by the NASA IMAGE (2000-2005) and Polar (1996-2008) missions, which offered a global context for multipoint in situ spacecraft measurements. This is most clearly illustrated by the development of the so-called Expanding-Contracting Polar Cap (ECPC) paradigm, where it is thought that the size of the auroral oval can (with certain assumptions) be used to deduce the magnetic flux content of the magnetotail lobes (e.g. Milan et al. 2012). The auroral oval increases in size as the flux content of the magnetotail increases, and decreases as it is reduced. Furthermore, the absolute location, structure and brightness of the auroral oval can be used (again with assumptions) to infer aspects of both the dayside solar wind magnetosphere interaction and the progression of nightside magnetotail dynamics through all phases of geomagnetic substorms and storms.

However, even with global auroral imaging (which is unfortunately no longer available since about 10 years), one cannot know in general where the boundaries of the magnetosphere actually lie due to the inherent uncertainty in magnetic field line mapping. Nor does one have independent confirmation of the physical processes that occur there. Only in fortuitous circumstances are spacecraft appropriately positioned to confirm that a particular process (most specifically reconnection) is occurring in a particular place, at a particular time, to unambiguously explain the auroral observations. For example the observation of a persistent dayside auroral spot by IMAGE was shown to be due to continuous reconnection poleward of the cusp, observed by Cluster (Frey et al. 2003).

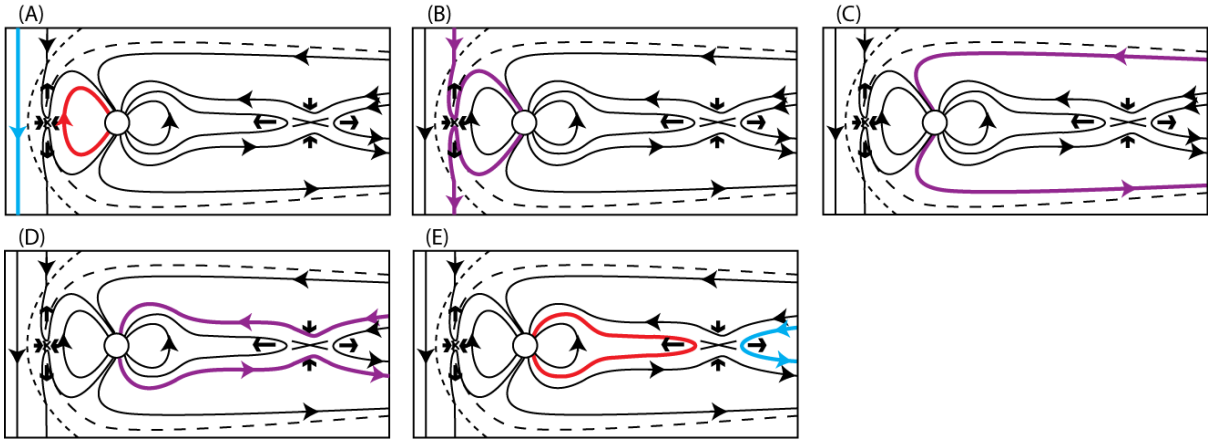

Figure 3. Cartoon showing the progression of the Dungey cycle. Under southward IMF conditions, dayside reconnection (panel A) opens magnetic flux (panel B) which convects over the poles and is stored as magnetic energy in the magnetotail lobes (panel C). This stored energy accumulates until an explosively release (panel D) returns closed flux to Earth in conjunction with dramatic auroral displays at high latitudes (panel E). Substorms may result from changes in the external driving of the magnetosphere and/or internal magnetotail instabilities. (From Eastwood et al. 2015)

2.2 Global measurements of the Solar Wind-Magnetosphere Interaction

A host of mechanisms have been proposed to explain the nature of the solar wind-magnetosphere interaction, and in particular the entry into, storage within, and release from the magnetosphere of solar wind mass, energy, and momentum (Figure 2). Proposed magnetopause entry mechanisms include solar wind pressure variations battering the magnetosphere, the Kelvin-Helmholtz (wind-over-water) instability on the magnetopause, diffusion driven by wave-particle interactions, and magnetic reconnection. Proposed magnetotail release mechanisms include a host of plasma instabilities, e.g. ballooning or cross-tail current driven instabilities, and magnetic reconnection.

In contrast to all the other mechanisms, reconnection predicts enhanced interactions during intervals of southward IMF orientation. Therefore statistical studies of remote observations demonstrating that ionospheric convection, the strength of field-aligned currents into and out of the ionosphere, the likelihood of geomagnetic substorms, and the magnitude of geomagnetic storms all increase for southward IMF orientations, point to

reconnection as the dominant mode of solar wind-magnetosphere interaction. Reconnection may be the cause or consequence of various plasma instabilities proposed to occur within the near-Earth magnetotail.

Reconnection is a microphysical process with macrophysical consequences. The need to understand the microscale physics underlying reconnection has led to the launch of multi-spacecraft missions like ISEE-1/2, AMPTE, Cluster, THEMIS, Van Allen Probes and MMS with ever decreasing inter-spacecraft separations. These missions have confirmed the presence of the accelerated plasma flows, magnetic field components normal to the magnetopause and magnetotail current sheet, streaming energetic particles, and boundary layers containing admixtures of the particle populations on both sides of reconnecting current sheets at the magnetopause and within the magnetotail, just as predicted by reconnection models.

While isolated single or closely-spaced multipoint in situ measurements can be used to identify reconnection events and study the microphysics of reconnection, they cannot be used to distinguish between models in which reconnection is predominantly patchy or global, transient or continuous, triggered by solar wind features or occurring in response to intrinsic current layer instabilities, component and occurring on the equatorial magnetopause or antiparallel and occurring on the high-latitude magnetopause. Nor can isolated measurements be used to determine the global state of the solar wind-magnetosphere interaction, as measured by the rate at which closed magnetic flux is opened or open flux closed. For all of these tasks, and many more, global observations are needed. It would, however, be a major undertaking to launch a flotilla of microsatellites capable of making in situ measurements at all relevant locations.

In the absence of any plans for such a constellation, imagers can supply the global measurements needed to understand the nature of the solar wind-magnetosphere interaction. The boundaries seen in soft X-ray (and low energy neutral atom) images correspond to plasma density structures like the bow shock, magnetosheath, magnetopause, and cusps. Thus soft X-ray imagers can be used to tract the inward erosion of the dayside magnetopause during the growth phase of geomagnetic substorms and the outward motion of this boundary following substorm onsets. The location of the magnetopause provides information concerning the amount of closed flux within the dayside magnetosphere, the rate of magnetopause erosion or recovery provides information concerning the steadiness of reconnection, while the location of the portion of the magnetopause that moves provides information concerning the component or antiparallel nature of reconnection.

Soft X-ray imagers can also be used to track the equatorward motion of the cusps during the substorm growth phase and their poleward motion following onset. Just as in the case of the magnetopause, cusp observations can be used to determine the amount of closed flux within the dayside magnetosphere, the rates of erosion and recovery, the steadiness of reconnection, and the equatorial or high-latitude location of reconnection.

Global auroral images from a high inclination, high altitude, spacecraft provide an excellent complement to soft X-ray images. The dimensions of the auroral oval indicate the open magnetic flux within the Earth's magnetotail. Poleward and equatorward motions of the dayside and nightside auroral oval provide crucial information concerning the occurrences and rates of reconnection at the dayside magnetopause and within the Earth's magnetotail. Ground-based auroral imagers frequently observe transients in the dayside aurora which can be interpreted as evidence for bursty reconnection and/or the Kelvin-Helmholtz instability. Global imagers are needed to determine the occurrence rates and extents of these transients, which in turn determine their importance to the solar wind-magnetosphere interaction. Observations of the nightside auroral oval can be used to pinpoint the time of substorm onset, determine the extent of the reconnection line in the magnetotail, and distinguish between steady, bursty, and sawtooth modes of reconnection in the magnetotail. Global auroral images can be used to test the recently proposed hypotheses that plasma flows (and aurora) originating within the dayside oval and streaming across the polar cap trigger substorm onset when they reach the nightside oval.

Finally, measurements of the solar wind plasma and magnetic field input to the magnetosphere by a monitor located near Earth are essential for the above studies, because having such a monitor reduces concerns regarding the arrival times of possible solar wind triggers for magnetospheric events and reduces concerns regarding the dimensions of solar wind structures transverse to the Sun-Earth line. In situ measurements from the same plasma and magnetic field instruments on the observing spacecraft on an elliptical polar orbit can also play a crucial role in validating the inferences concerning processes at the magnetopause and in the magnetotail that are drawn from the soft X-ray and auroral imagers.

2.3 Open science questions

Understanding and thus predicting the non-linear global system behaviour of the magnetosphere has remained both the central objective and grand challenge of solar-terrestrial physics in particular (and space plasma physics more generally) for more than 50 years.

In situ data have dramatically improved our understanding of the localised physical processes involved (reconnection, diffusion, boundary instabilities, turbulence, particle acceleration, etc.). Multi-point and multi-scale missions such as Cluster, THEMIS and, more recently, MMS proceed down this path with an ever-increasing focus on the microscopic physics of space plasmas. However, piecing the individual parts together to make a coherent overall picture, capable of explaining and predicting the dynamics of the magnetosphere at the system level has proved to be extremely difficult. This is due to the fact that it is fundamentally impossible to determine the global behaviour of a complex system with sparse in situ measurements, even with the support of increasingly sophisticated global computer models of the solar wind – magnetosphere interaction.

To address this global aspect, SMILE will explore the solar wind-magnetosphere coupling via X-ray images of the magnetosheath and polar cusps, UV images of global auroral distributions and simultaneous in situ solar wind/magnetosheath plasma and magnetic field measurements. Remote sensing of dayside magnetosheath and the cusps with X-ray imaging is now possible thanks to the relatively recent discovery of solar wind charge exchange (SWCX) X-ray emission, first observed at comets, and subsequently found to occur in the vicinity of the Earth's magnetosphere.

SMILE will answer the following science questions:

- What are the fundamental modes of the dayside solar wind/magnetosphere interaction?
- What defines the substorm cycle?
- How do CME-driven storms arise and what is their relationship to substorms?

2.3.1 What are the fundamental modes of the dayside solar wind/magnetosphere interaction?

Dayside reconnection causes plasma to flow anti-sunward through the magnetopause boundaries, the cusps, and over the polar caps. On occasions reconnection can persist for long times, both for northward and southward IMF orientations (e.g. Frey et al. 2003; Phan et al. 2004). However, reconnection can also be bursty and time dependent, generating significant structure and step motion of the magnetopause (Figure 4). For example, patchy reconnection (Russell and Elphic 1978), bursty (i.e., time dependent) reconnection from a single X-line (Scholer 1988; Southwood et al. 1988), and multiple X-line reconnection (Lee and Fu 1985; Raeder 2006; Omidi and Sibeck 2007), may produce so-called flux transfer events (FTEs) which, at the most basic level, may be thought of as time dependent structures propagating along the magnetopause.

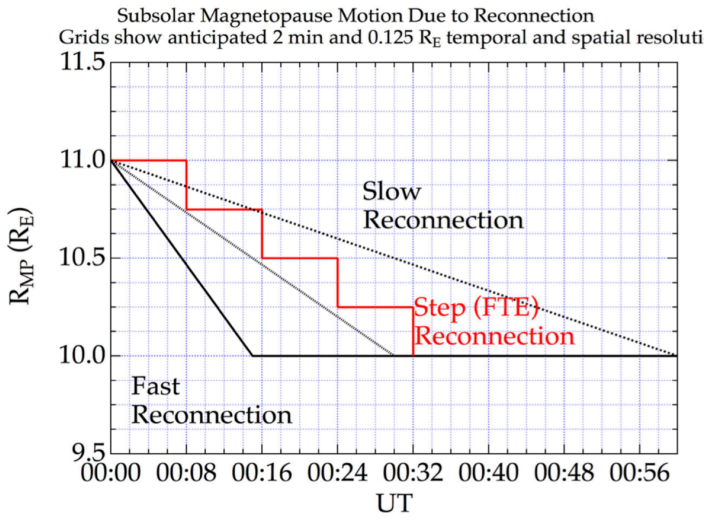

Figure 4. Location of the subsolar magnetopause as a function of time for slow reconnection (dotted line), bursty reconnection (red line), normal rate reconnection (grey line) and fast reconnection (solid line).

It is thought that steady reconnection occurs for low beta (i.e. magnetic field pressure dominated) solar wind and magnetosheath, whereas unsteady reconnection is more likely for high beta solar wind conditions. However, a simple confirmation of this hypothesis is obscured by the fact that apparently unsteady magnetopause reconnection may simply be directly driven by variations in the solar wind parameters.

The peculiar magnetic topology of the cusps means that they also play a pivotal role in magnetospheric dynamics: they are the sole locations where solar wind has direct access to low altitudes (e.g. Cargill et al. 2005). They are essentially the boundary that separates magnetic field lines that close in the dayside hemisphere from those that extend far down the magnetotail. During subsolar reconnection solar wind energy, mass and momentum are transferred through the cusp into the magnetosphere. As described above, this momentum transfer is the major driver of large-scale magnetospheric convection, reflecting again the pivotal role of these regions. Since the cusps are the endpoints of a large portion of the magnetospheric magnetic field, their structure gives information about a larger context than any other structure within the magnetosphere.

The latitudinal location of the cusp depends on the level of interconnection of the Earth's dipole with the IMF (Newell et al., 1989), i.e. the amount of recently 'opened' magnetospheric magnetic flux. When the solar wind magnetic field points southwards, magnetic reconnection at the magnetopause opens closed dayside magnetic field lines, causing the region of open field lines in the polar cap to expand to lower latitudes (Figure 5). The latitudinal position of the cusp is also an indicator of how much magnetic flux is being removed from the dayside to fuel substorm behaviour on the nightside. When the IMF turns northward, the cusps move poleward. This might be because reconnection at the dayside magnetopause stops, while reconnection within the magnetotail continues to close magnetic field lines which then convect to the dayside magnetosphere (e.g. Milan et al. 2003).

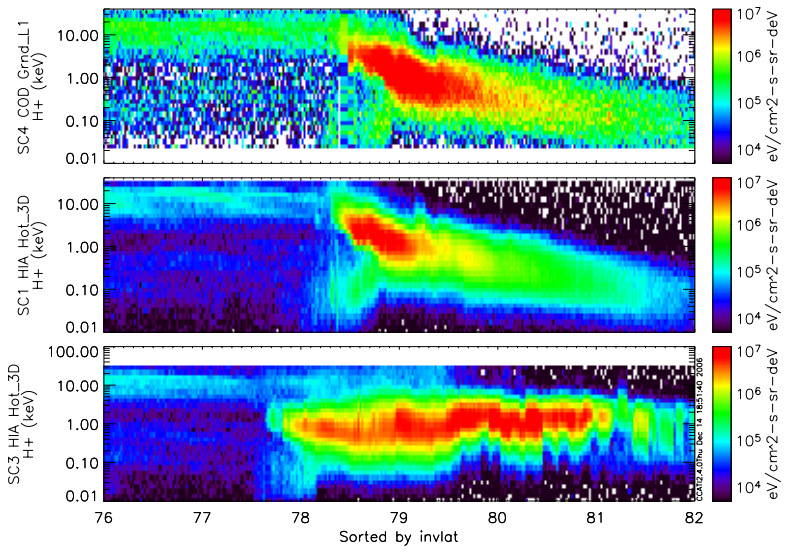

Figure 5. Crossing of the polar cusp with three Cluster spacecraft as a function of invariant latitude. The ion spectrograms are shown for Cluster 4 (top), Cluster 1 (middle) and Cluster 3 (bottom). Cluster 4 and 1 crossed the cusp when the IMF was Southward at 15:15 and Cluster 3 after the IMF turned northward at 15:23. The cusp expanded poleward after the IMF turned northward. The energy of the ions in the cusp (red area) is decreasing with increasing invariant latitude when the IMF was Southward (two top panels) and increasing with increasing invariant latitude when the IMF was northward (bottom panel) (Escoubet et al., 2008)

However, it might also occur because reconnection poleward of both cusps appends magnetosheath magnetic field lines to the dayside magnetosphere (Figure 5 bottom panel), transforming open lobe magnetic field lines into closed dayside magnetic field lines and allowing the immediate entry of dense magnetosheath particle fluxes into the magnetosphere (Song and Russell 1992). The cusps, being by definition the boundary between open lobe and closed dayside field lines, should move to lower and higher latitudes as the open field line region expands and contracts, respectively. The amount of open flux depends on the rate of reconnection both on the dayside magnetopause and in the nightside magnetotail plasma sheet. It is thus of key importance to measure how the cusp responds to northward and southward turnings of the IMF, since this is intimately related to the strength of the solar wind – magnetosphere coupling.

The cusp latitude is directly related to the level of open flux within the magnetosphere, which in turn is controlled by the main mechanism of energy transfer, the reconnection process. Although crucial in

understanding the system energetics quantitatively, the amount of energy transfer is difficult to assess with in-situ measurements because it occurs over a large area of the magnetopause. Therefore this critical parameter determining the magnitude of dynamical events accurately has only been assessed with correlative studies.

Further complexity is introduced by the east-west (or dawn-dusk) component of the IMF. The northern cusp moves duskward and the southern cusp dawnward during periods of duskward IMF orientation, and in the opposite directions during intervals of dawnward IMF orientation (e.g. Newell et al. 1989; Taguchi et al. 2009). We understand these changes in terms of magnetic reconnection: when the IMF points duskward, antiparallel reconnection is expected in the post-noon northern hemisphere and pre-noon southern hemisphere. Plasma enters the magnetosphere from the cusp along the newly reconnected magnetic field lines, which then move anti-sunward in response to pressure gradient forces, but often initially move towards local noon under the influence of curvature forces (e.g. Smith and Lockwood 1996).

Finally, the solar wind dynamic pressure may play a role in determining cusp latitude. LEO observations from e.g. DMSP and simulations predict that enhanced (reduced) pressures may cause the cusp to move equatorward (poleward) (e.g. Newell and Meng, 1994; Yamauchi et al. 1996; Palmroth et al. 2001; Pitout et al., 2006).

Reconnection is therefore thought to cause the shape of the magnetopause to become blunter. By contrast, variations in the solar wind dynamic pressure should cause self-similar changes in magnetospheric dimensions. Thus by measuring the curvature, size and absolute location of the magnetopause and the location (latitudinal position), size, and shape of the cusps, it is possible to distinguish the differing effects of pressure changes and magnetic reconnection on the global magnetospheric system. This would distinguish on a global level the nature of the solar wind - magnetosphere interaction, the dominant driving mechanisms and modes of interaction.

The measurements required to address the first science objective are as follow:

- steady/unsteady solar wind variations
- steady/unsteady motion of the dayside magnetopause
- transient brightenings and equatorward leaps in the dayside auroral oval
- transient brightenings and equatorward leaps in the cusp

2.3.2 What defines the substorm cycle?

We know that southward IMF is required to increase the energy density of the magnetotail lobes, and the more prolonged the interval of southward IMF, the more energy is stored, but the precise nature of the energy loading and the role it plays in the subsequent onset of geomagnetic activity is very controversial. For example, one very fundamental question is whether each substorm requires its own interval of loading (growth phase), or whether multiple substorms can occur in response to a single growth phase.

The polar cap is an area of magnetic field lines that are open to the solar wind and is readily identified by the auroral oval which bounds it (Figure 6). Auroral oval observations provide information about the ionospheric footpoints of magnetopause processes. Specifically, the expanding-contracting polar cap paradigm utilises basic properties of the auroral oval to provide direct measurements of the state of the magnetosphere by measuring the size of the polar cap (e.g. Milan et al. 2012). The area of open flux within the polar cap changes directly in response to the amount of open flux in the magnetotail lobes, and the very dynamic changes that occur in this region are in response to different solar wind conditions.

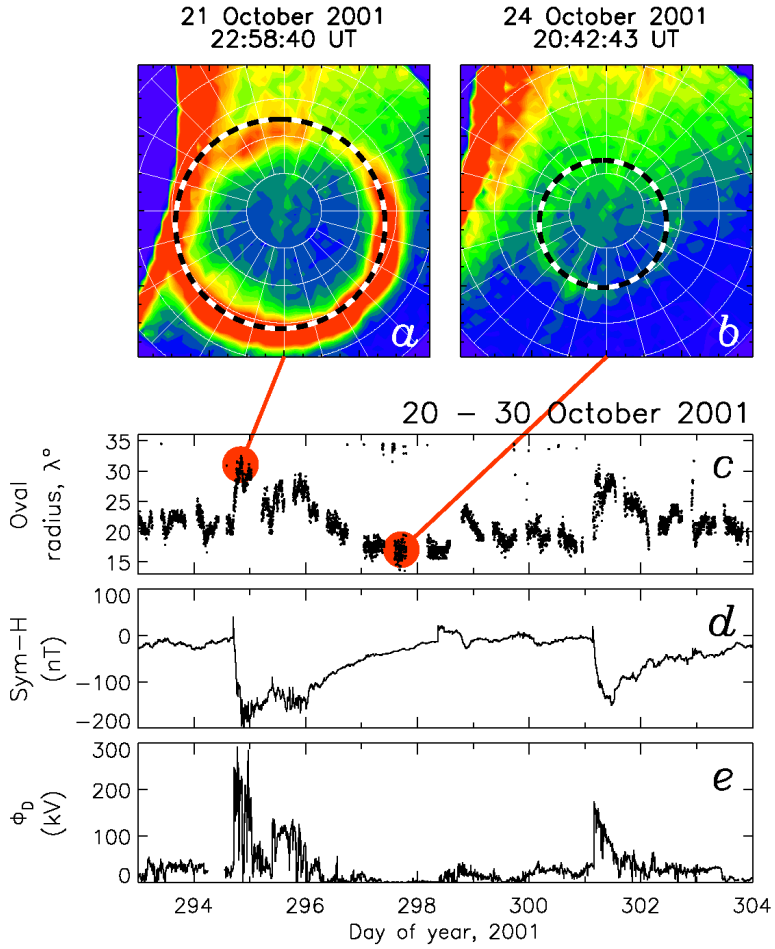

Figure 6: (a and b) Determination of the size of the polar cap from the radius of the auroral oval; (c, d, and e) time-series of the radius of the auroral oval, the Sym-H index measure of ring current intensity, and a proxy for the dayside reconnection rate derived from upstream solar wind conditions. (Milan, 2009). These measurements have necessarily been non-continuous in the past due to the orbits of previous auroral imaging missions (data gaps in panel c), hindering progress in understanding solar wind - magnetosphere coupling. Short time-scale variations in polar cap size correspond to substorms, but large discontinuities exist over some data gaps indicating that the storm behaviour is only partially captured.

The trigger that leads to substorm onset remains controversial. Is the substorm triggered by changes in IMF orientation (related to a change in shape of the magnetopause due to reconfiguration of magnetospheric currents associated with dayside reconnection) (e.g. Hsu and McPherron 2002; Lyons et al. 1997; Morley and Freeman 2007; Wild et al. 2009)? Or do solar wind dynamic pressure changes play the key role (by compressing the magnetotail) (e.g. Boudouridis et al. 2003; Hubert et al. 2006, 2009; Milan et al. 2004)? How large and rapid these driving changes must be is unknown. Another viewpoint is that the external solar wind condition provides only the general configuration of the magnetosphere for substorm expansion onset. When and where it occurs depends on the ionospheric conditions as well as internal local magnetospheric parameters. Furthermore the role of the prior history of the magnetosphere in conditioning the response is not well understood and there are reports of substorms with no obvious external drivers (Huang 2002).

Thus despite a plethora of in situ observations, fundamental questions remain unanswered. If the onset of a substorm is due to external driving, what is the nature of the driving mechanism, and how does this depend on the precise configuration of the magnetosphere?

Although the substorm is perhaps the most well-known type of magnetospheric event, other modes of magnetospheric behaviour are observed. During steady magnetospheric convection, anti-sunward ionospheric convection is observed, and so flux is being transferred from the dayside to the nightside, but the size of the polar cap does not change. Thus it is thought that reconnection at the day and night side is balanced. The solar wind drivers that enable steady magnetospheric convection are not well understood, because they can persist for more prolonged intervals where in situ satellite data are not available. During saw-tooth events, which are oscillations of energetic particle fluxes at geosynchronous orbit recurring with a period of about 2–4 h (e.g. Henderson et al., 2006), the auroral oval expands and contracts with a period of a few hours. It is not clear if this is due to an intrinsic instability/mode of dynamic behaviour or if it corresponds to a series of repeating substorms. These may simply reflect the same internal physics being driven differently by the solar wind, or they may represent fundamentally different types of behaviour.

A recent development is the awareness of a low-intensity auroral feature called auroral beads that develop in pre-breakup auroral arcs and eventually produce the initial brightening and substorm expansion onset (Henderson, 1994). This feature was not recognized earlier due to its low intensity and is shown in Figure 7. The auroral beads have specific wavelengths and corresponding exponential growth in the auroral intensity that are different from case to case, apparently dependent on the state of the magnetosphere just prior to substorm expansion onset. The characteristics of auroral beads revealed recently impose another set of rather severe observational constraints that discriminate among several potential substorm onset processes under consideration. Two potential plasma instabilities that may account for these characteristics are the ballooning instability and the cross-field current instability. The latter was recently examined and was found to account for the observed auroral bead characteristics, as illustrated in Figure 7. More recently, however, Kalmoni et al. (2018) showed that a third mechanism, kinetic Alfvén waves, could explain the temporal and spatial scales of auroral beads. Coordinated global imaging from SMILE and ground-based auroral observations around substorm expansion onset would be ideal to test these proposed plasma instabilities further. A working group on Ground-Based and Additional Science (GBAS) has been created by the science study team to coordinate SMILE observations with ground-based observatory (see section below).

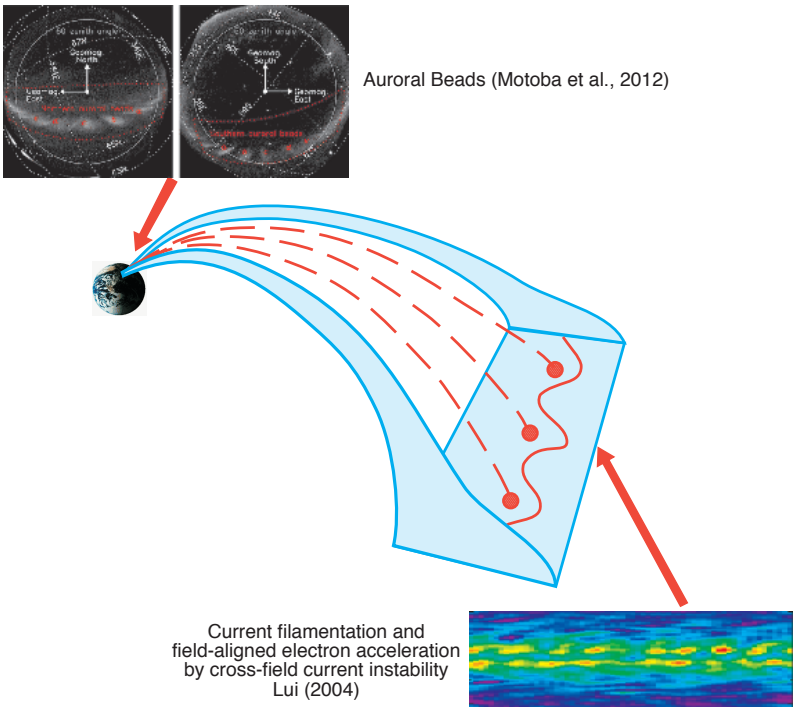

Figure 7. A schematic diagram to show (top) the conjugacy of auroral beads by ground-based observations from both Northern and Southern hemispheres, (middle) the wavelengths in the magnetospheric equatorial plane corresponding to auroral beads, and (bottom) the current filamentation and electron acceleration arising from the excitation of the cross-field current instability

Disentangling these different modes of behaviour follows on from the first question. Once a substorm is triggered, what controls its subsequent evolution? To what extent is it sensitive to changes in the solar wind conditions, and how does this sensitivity depend on the internal state of the magnetosphere (e.g. substorm phase, amount of remaining stored energy, etc.)?

The measurements required to address the second science objective are as follow:

- location and motion of the dayside magnetopause boundary,
- location and motion of the auroral oval,
- substorm brightenings of the auroral oval,
- solar wind input.

2.3.3 How do CME-driven storms arise and what is their relationship to substorms?

While intervals of southward IMF occur naturally in the solar wind, and so substorms occur on a daily basis (Borovsky et al. 1993), strong driving causing geomagnetic storms tends to occur in response to coherent solar wind structures, particularly Coronal Mass Ejections (CMEs) (Gonzalez et al. 1999) (Figure 8)

The degree to which solar wind plasma, momentum and energy enter the magnetosphere is characterized by so-called solar wind coupling functions (Gonzalez 1990; Finch and Lockwood 2007). Physically, magnetic reconnection at the dayside magnetopause is enhanced if there is a strong interplanetary magnetic field component opposite to the dayside magnetospheric magnetic field, supplemented by fast solar wind, for an extended period of time.

CMEs are transient eruptions of material from the Sun's corona into space (Forbes 2000). CMEs propagate at super-magnetosonic speeds relative to the ambient solar wind, and play a particularly important role in the dynamics of the Earth's magnetic field because they can contain long intervals of southward IMF (e.g. Gonzales et al. 1999). In general, the largest geomagnetic disturbances are associated with CMEs, with the level of activity being directly related to the flow speed, the field strength and the southward component of the magnetic field (Richardson et al. 2001).

Figure 8. Coronal mass ejection (CME), shown as an orange arch travelling toward Earth. Left insert shows the CME observed by SOHO spacecraft and right inserts shows the aurora observed from space with Polar spacecraft (top) and from ground (bottom) (credit NASA).

Sometimes CMEs don't have the expected effects associated with a geomagnetic storm. When the interplanetary magnetic field is northward the energy transmitted to the magnetosphere is more limited. However, when solar filaments are contained in CMEs, there can be some effects similar to superstorms such as the superfountain in the equatorial ionosphere, magnetotail stretching and strong joule heating in the polar ionosphere (Kozyra et al., 2014). Furthermore, Turc et al. (2014) showed that the Earth's bow shock can, under certain conditions, modify the interplanetary magnetic field direction contained in CMEs which then do not have the predicted effect on the magnetosphere.

Understanding the global CME/magnetosphere interaction is crucial to understanding precisely how the structure of the CME is responsible for the different phases of geomagnetic storms. On a practical level, storms driven by CMEs have potentially severe space weather consequences and represent a significant threat to infrastructure resilience worldwide.

Very basic questions still remain. Is the duration and magnitude of solar wind driving the sole arbiter of whether a storm will occur? What is the relationship between the storm and substorm? Are storms always a separate phenomenon, or can they be considered as being composed of multiple substorms?

Finally, although the question of how a storm starts has been central to the scientific studies of the magnetosphere for as long as measurements have been available, the question of duration is growing in importance, driven by the needs of the end-user in the space weather context (i.e. confidence in issuing 'all clear'). Does a storm end because it has exhausted the reservoir of stored magnetic energy in the magnetotail? Or does a storm stop because the solar wind driving conditions have changed? If both possibilities are observed to occur, which is the more important? And once the solar wind driving is removed, how rapidly does the magnetosphere recover? Is it more likely that the solar wind conditions will change, or is the stored magnetotail lobe energy depleted so rapidly that the changing solar wind plays only a minor role?

The measurements required to address the third science objective are the same as the ones for the second science objective but should be done during a CME-driven storm:

- location and motion of the dayside magnetopause boundary
- location and motion of the auroral oval
- substorm brightenings of the auroral oval
- solar wind input

2.4 A novel method to image the magnetosphere

Solar wind charge-exchange (SWCX) occurs when highly ionized species in the solar wind interact with neutral atoms. An electron from the neutral is transferred to the ion, initially in a highly excited state (see review in Sibeck et al., 2018). On relaxation to the ground state one or more photons are emitted, usually in the extreme ultraviolet or the soft (low energy) X-ray. The energy band below 0.5 keV is extraordinarily rich in SWCX emission lines from a large number of ionization states of a large number of species, while the 0.5-2.0 keV band is dominated by a few strong lines due to charge-exchange by O^{7+}, O^{8+}, Ne^{9+}, and Mg^{11+}. There are many sources of SWCX emission in the heliosphere, including comets and the neutral interstellar medium that flows through the solar system. Typically, the brightest source of SWCX is that due to the Earth's exosphere, which is primarily hydrogen, interacting with the shocked, compressed, solar wind in the magnetosheath.

SWCX emission due to the magnetosheath was first observed by ROSAT, though its source was a mystery at the time (*Figure 9*). ROSAT surveyed the soft X-ray sky by scanning great circles through the ecliptic poles, with each scan overlapping ~95% of the previous scan. Comparison of successive scans revealed strong temporal variations with scales of hours to days that were dubbed the "Long Term Enhancements" (LTE). A large-scale minimization routine was used to isolate the LTE, though the absolute minimum level could not be determined.

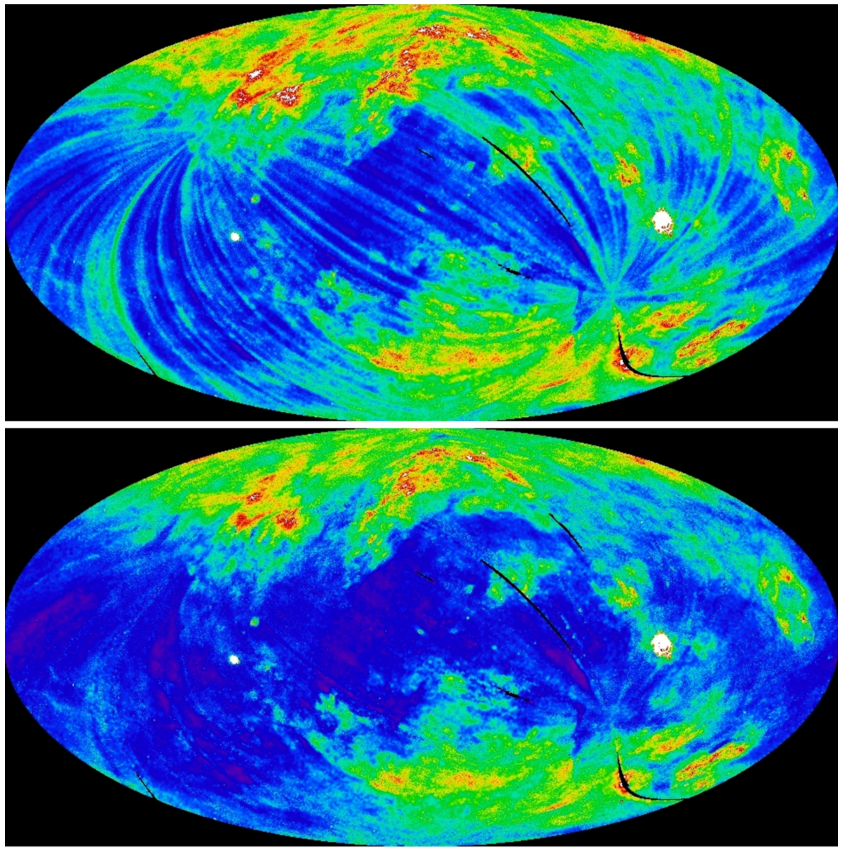

Figure 9. Upper Panel: ROSAT map of the 1 keV sky before the removal of Long Term Enhancements (LTEs). The map is in Galactic coordinates with (l, b) = (0,0) at the centre and longitude increasing to the left. The diffuse X-ray surface brightness increases from purple to white (the count rate varies from purple, ~250 counts s^{-1} $arcmin^{-2}$, to white, ~2500 counts s^{-1} $arcmin^{-2}$). Lower Panel: The same data after the subtraction of an empirical estimate for the LTE contribution (Sibeck et al., 2018).

Cravens et al. (2001) showed that the streaks occurred during intervals of enhanced solar wind ion flux. Figure 10 compares the ROSAT 1/4 keV soft X-ray light-curve from 1990 to 1991 (black) with the solar wind ion flux (solar wind density times solar wind velocity, $n_{sw}v_{sw}$) simultaneously observed by IMP-8 (Kuntz et al. 2015). Data points are averaged to 95 min, the approximate period of the ROSAT orbit. Short gaps in the ROSAT light-curve result primarily from either non-survey operations or satellite operational issues. The long gaps in the ROSAT light curve are due to the survey being accomplished in four separate time intervals. Gaps in the IMP-8 observations reflect the absence of telemetry and times when IMP-8 was within the magnetotail or magnetosheath.

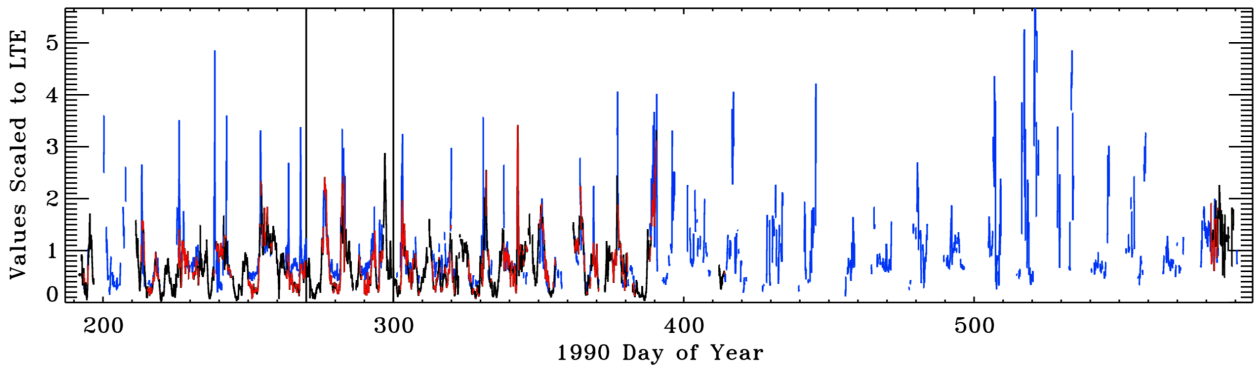

Figure 10. 1/4 keV LTE flux (black) and the solar wind flux (blue) as a function of date (Kuntz et al. 2015). The LTE flux is in units of ROSAT counts s^{-1} FOV^{-1}. The solar wind flux from IMP-8 has been scaled to match the LTE flux. Periods of LTE data for which there is also solar wind data are plotted in red. The vertical lines bound the much shorter interval considered by Cravens et al. (2001)

Inspection of Figure 10 reveals that band-integrated emissions in the 1/4 keV band track solar wind fluxes closely despite the variations in solar wind composition that occur as a function of solar wind structure. The scatter plot of LTE emission versus solar wind flux shown in Figure 11 confirms this point (Kuntz et al. 2015). Here the dotted lines bounding the distribution show the range of variations expected for identical solar wind

conditions but different look directions along each 95 min ROSAT orbit. The light-curve and scatter plots for the 3/4 keV band (not shown) do not provide any evidence for a similar correlation with solar wind fluxes, suggesting that the O line emissions that dominate the 3/4 keV band are less well correlated with the solar wind flux than the aggregate of the many lines that produce the 1/4 keV band (Kuntz et al. 2015).

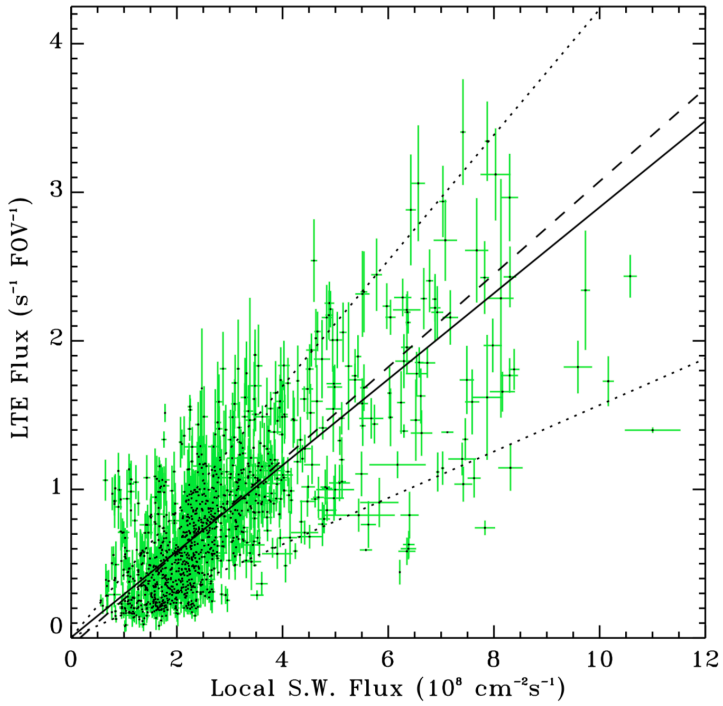

Figure 11 ROSAT observations of the 1/4 keV LTE flux versus IMP-8 observations of the local solar wind flux. The solid line is the best fit of (LTE count rate versus $n_{sw}v_{sw}$), the dashed line is the best fit minimizing the distance orthogonal to the fitted line, and the dotted lines show the relations with 0.54 and 1.46 times the best fit slope (Kuntz et al. 2015)

The SWCX flux is given by the integral along the line of sight of $\zeta(n_n n_p v_{rel})=\zeta Q$ where n_n is the density of neutral particles, n_p is the density of solar wind protons, v_{rel} is their relative velocities, and ζ contains the information about ion abundances, interaction cross-sections, branching ratios, etc. Q can be determined from MHD models of the magnetosheath and models for the exosphere. However the value of ζ for strong lines is sometimes quite uncertain, and for weak lines it is usually completely unknown. A recent comparison of the ROSAT LTE rates with the Q determined from models for the solar wind during the ROSAT observations has led to a determination of ζ for the ROSAT 1/4 keV band, which allows one to scale any MHD model of the magnetosheath to X-ray emissivity. Thus, one can feel relatively confident of the simulations of instrumental views of the magnetosheath.

Three different groups have been simulating the X-ray emission from the magnetosheath. Although there has as yet not been a detailed comparison, it is clear that useful parameters, such as the magnetopause distance can be determined for a large range of observing aspects, so long as the spacecraft is sufficiently far from the Earth. Determining the magnetopause distance is particularly interesting, not only for the science goals described above, but also given the divergent recent results from astrophysical missions.

SWCX emission from the magnetosheath has been observed by all recent astrophysical X-ray observatories. The XMM-Newton observatory is in high Earth orbit and sometimes observes through the nose of the magnetosheath (Carter et al., 2011). Given the expected SWCX X-ray brightness of the dayside magnetosheath such observations can serve as an important check on our simulations. Discrepancies when comparing predicted and observed emission strengths may be due to errors in the distances to the magnetopause predicted by the MHD models. The differences in the underlying MHD codes demonstrate the need for X-ray observations to constrain and validate the MHD results.

It should also be noted that studies of the X-ray emission from the magnetosheath require wide-field imagery, an area of current interest in astrophysics. For low to median solar wind conditions, the signal from the magnetosheath is only a few times stronger than the soft X-ray background. Thus, study of the X-ray emission from the magnetosheath requires astrophysical techniques and expertise. In return, astrophysics is deeply interested in detecting the Warm Hot Intergalactic Medium through O^{+6} and O^{+7} emission, and thus depends

upon researches such as these to characterize and remove the SWCX emission. Understanding the SWCX from the magnetosheath will necessarily require interdisciplinary study.

2.5 Modeling solar wind-magnetosphere interaction and field of view

2.5.1 MHD model

The solar wind-magnetosphere interaction can be modeled by global MHD codes, for example in our simulations (see below) we used the 3-D PPMLR (extended Lagrangian version of the piecewise parabolic method) MHD code jointly developed by the University of Science and Technology of China (USTC) and the National Space Science Center (NSSC), CAS (Hu et al., 2007). It solves the ideal MHD equations in the numerical domain extending from 30 to –300 RE along the x axis and from -150 to 150 RE in y and z directions of the geocentric solar magnetospheric (GSM) coordinate frame. The minimum grid spacing for the present simulation is 0.4 RE. The Earth's dipole tilt is set to be zero and the ionosphere is simplified as a spherical shell with a uniform Pedersen conductance and a zero Hall conductance.

The X-ray intensity for a particular line of sight can be estimated by the line integration of volume emission rate (P) [Cravens, 2000]:

$$I = \frac{1}{4\pi}\int P dr = \frac{1}{4\pi}\int \alpha n_H n_{sw} < g > dr \text{ (keV cm-2 s-1 sr-1),}$$

where α is the efficiency factor, which is taken to be 1×10^{-15} eV cm^2 in our simulations, n_H is the number density of the exospheric hydrogen and n_{sw} that of the solar wind. Integration of P over the line of sight starts from the satellite position to r =80 R_E. X-ray emission beyond 80 R_E is neglected as the density of exospheric hydrogen drops dramatically there.

We use a solar storm on Sept. 12, 2014, with an ICME reaching the Earth at ~15:20 UT, to simulate the response of the Earth's magnetosphere and its environment to the incoming solar wind. The simulated X-ray intensity for the storm event is shown in the left column of Figure 12. From the top to the bottom, the panels show the X-ray intensity from the dayside magnetosheath and cusps before (top row) and after (second row from the top) the arrival of the interplanetary shock, as well as the response of the magnetosphere to the interplanetary magnetic field turning from northward (third row) to southward (fourth row). Furthermore, the above modeled X-ray intensity is converted into observed X-ray counts using an X-ray telescope simulator. The instrument simulator models an optic which uses square-channel micropore optic (MPO) plates in a Lobster-eye configuration. The detector is a back-illuminated X-ray sensitive CCD with high quantum efficiency (QE) to soft X-rays. The simulator includes the transmission properties of an optical/UV filter required to minimise optical loading on the CCDs. The exposure time is 300 s for simulations shown here. The counts images are shown with a larger FOV than the actual instrument to illustrate the relative strength of various features.

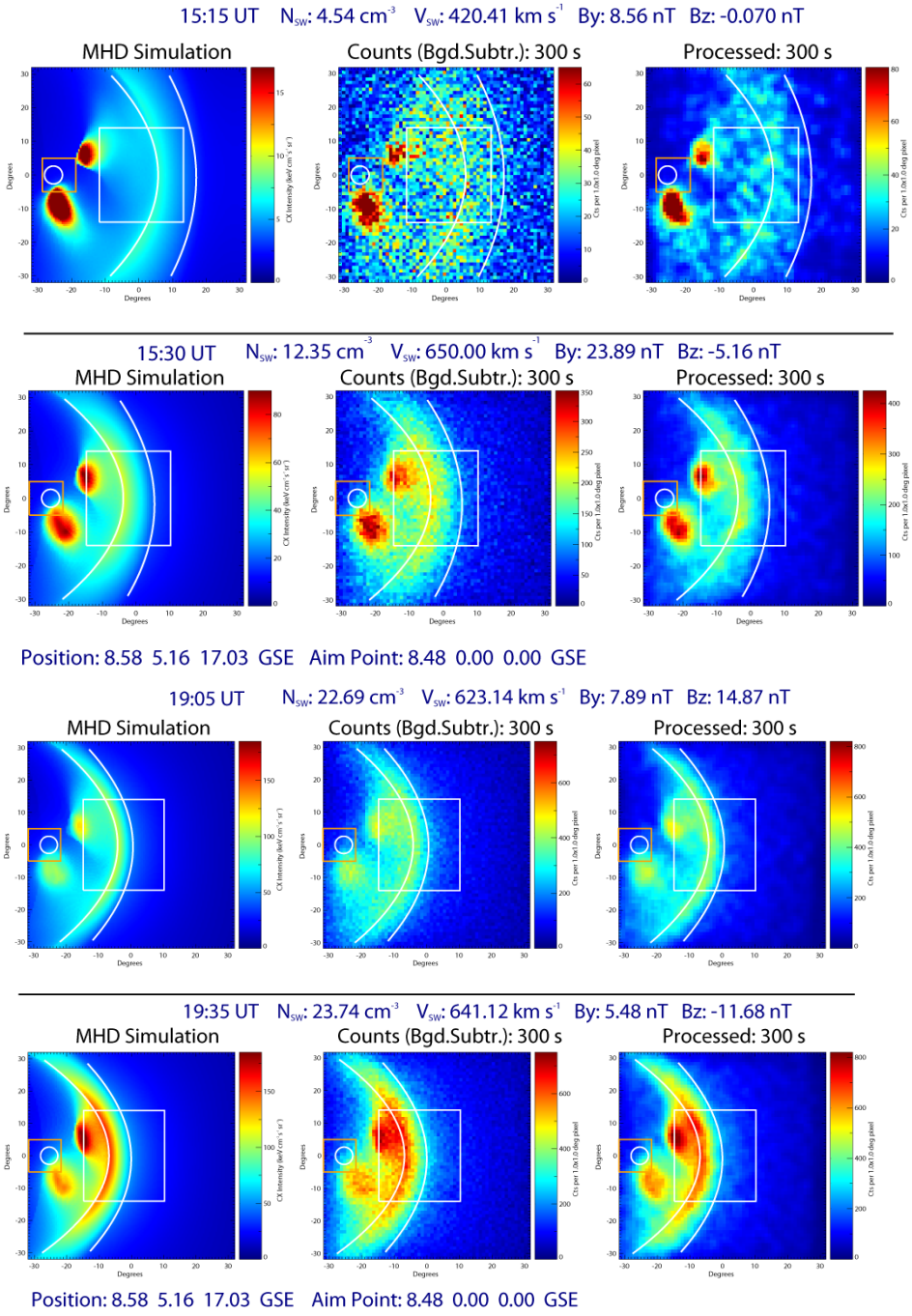

Figure 12. Simulated dayside magnetosphere before (first row) and after (second row) the arrival of an interplanetary shock, as well as its response to the interplanetary magnetic field turning from northward (third row) to southward (fourth row). The figure shows original MHD simulation data (left), the predicted soft X-ray counts (center) and the processed image (right).

After the shock arrival (2nd row from the top of Figure 12) a substantial increase of X-ray emission is observed as well as a compression of the magnetosphere due to increase of pressure at the magnetopause. After the turning of the IMF from northward to southward (4th row on Figure 12) the magnetopause is also observed to move inward, most likely due to the erosion of the dayside magnetosphere by magnetic reconnection.

2.5.2 Boundary tracing

The Earth's magnetosheath and cusps emit strong fluxes of soft X-rays due to the high solar wind density and exospheric neutral density (See Figure 12). By taking soft X-ray images of the Earth's dayside system every several minutes, we can extract location and motion of the dayside boundaries such as bow shock, magnetopause, low- and high-latitude cusp boundaries. This section briefly introduces the two boundary tracing algorithms of Collier and Connor (2018) (hereafter referred to as the Tangential Direction Approach) and Jorgensen et al., (2018) (hereafter referred to as the Boundary Fitting Approach).

2.5.2.1 *Tangential direction method*

Collier and Connor [2018] showed that the soft X-ray peak direction is tangent to the magnetopause and derived an analytical formula of the magnetopause location ($\vec{p}$) as a function of spacecraft location ($\vec{s}$) and soft X-ray peak angles (θ):

$$\vec{p} = \left| \frac{\mathrm{d}\vec{s}}{\mathrm{d}\theta} \cdot \hat{\theta} \right| \hat{r} + \vec{s}.$$

where $\hat{r}$ is a unit vector along the direction of the tangent line-of-sight, i.e., the direction of soft X-ray peak, and $\hat{\theta}$ is a unit vector perpendicular to $\hat{r}$.

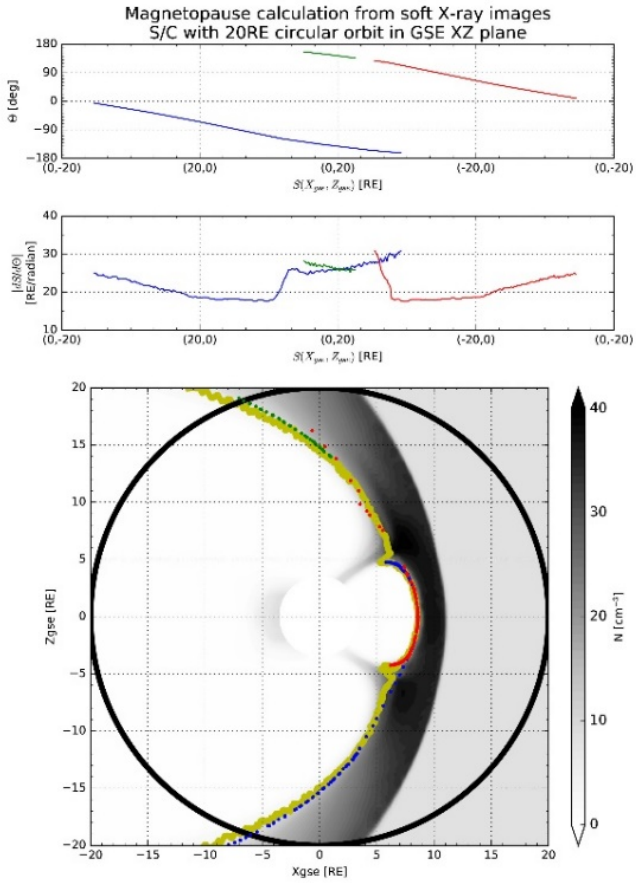

Figure 13. Demonstration of the boundary tracing algorithm of Collier and Connor [2018] for a circular orbit in the GSE XZ plane (GSE Y=0)

Figure 13 demonstrates the tangential direction algorithm by introducing a virtual spacecraft in a 20R_E circular orbit into the OpenGGCM global magnetosphere – ionosphere MHD model [Raeder et al. 2008 and references therein]. Top panel shows how the angle θ corresponding to the direction of the soft X-ray peak varies as the spacecraft orbits around the Earth. Middle panel shows how the spacecraft location with respect to the soft X-ray peak angle ($\mathrm{d}\vec{s}/d\theta$) changes during the circular orbit. During its journey, the spacecraft observes multiple soft X-ray peak angles (red, green, and blue lines) as the soft X-ray peak directions are tangent to the different parts of the magnetopause. The bottom panel shows the tracing results on the noon-midnight meridional plane where the plasma density is displayed as the black-and-white contour. The black and yellow lines represent the virtual spacecraft orbit and the magnetopause location calculated from the MHD model using maximum density gradient points along radial lines. The red, green, and blue dots indicate the magnetopause locations traced from the tangential direction method. The traced magnetopause position shows a good agreement with the MHD magnetopause. As the spacecraft orbit precesses around the Earth, the 3-D magnetopause surface can be reconstructed using the tangential direction algorithm as seen in Figure 14. The indentations of the magnetopause near the northern and southern cusps are well identified in this traced magnetopause.

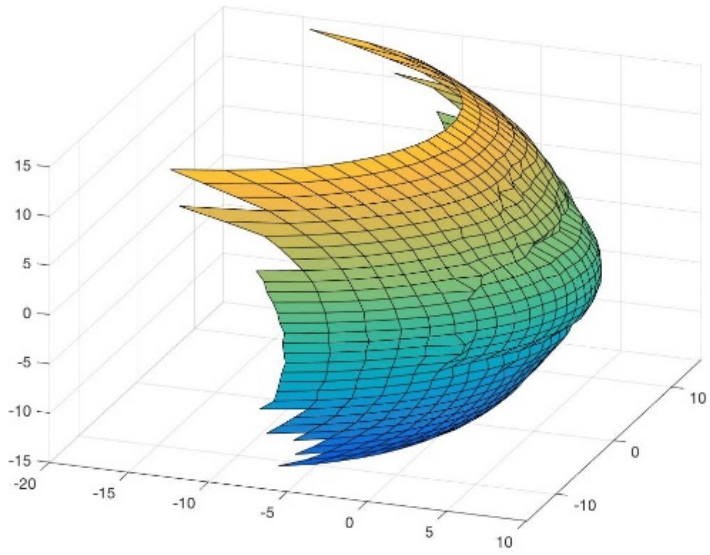

Figure 14. 3-D magnetopause constructed from the tangential direction algorithm of Collier and Connor [2018]

2.5.2.2 *Boundary Fitting Approach*

Usually, the magnetospheric system is highly dynamic, and thus the magnetopause and bow shock positions can have large variations on a short time scale. In this context, it is important to derive the 3-D magnetopause and bow shock locations from a single 2-dimensional (2-D) X-ray image. Jorgensen et al. (2018) construct a series of 2-D X-ray images based on parametric descriptions of the locations of boundaries and parametric expressions for the X-ray brightness distribution between the boundaries, and then find the best match with the 'real' X-ray image by the fitting process (After the launch of SMILE, the 'real' X-ray image would be the image observed by SXI. For the pre-study here, we use the image derived from the MHD simulation as the 'real' image).

Based on the PPMLR-MHD simulation results, we arrive at the following model about the magnetopause and bow shock:

$$r(\theta,\phi)=\frac{r_y(\theta)r_z(\theta)}{\sqrt{[r_z(\theta)\cos\phi]^2+[r_y(\theta)\sin\phi]^2}},$$

$$r_y(\theta)=r_0\left(\frac{2}{1+\cos\theta}\right)^{\alpha_y},$$

$$r_z(\theta)=r_0\left(\frac{2}{1+\cos\theta}\right)^{\alpha_z},$$

where θ is the angle from the X-axis and Φ is the rotation angle in the right-hand direction around the X-axis starting at the Y-axis. This uses the improved Shue model (Shue et al., 1997), which considers the asymmetry of the magnetopause and bow show boundaries along the north-south direction and dawn-dusk direction.

The suggested model for X-ray emissivity is:

$$F(\vec{r})=\begin{cases}0, \text{for } r<r_{MP}\\ (A_1+B\sin^8\theta)\left(\frac{r}{r_{ref}}\right)^{-(\alpha+\beta\sin^2\theta)}, \text{for } r_{MP}<r<r_{BS}\\ A_2\left(\frac{r}{r_{ref}}\right)^{-3}, \text{for } r_{BS}<r\end{cases}$$

where r_{MP} and r_{BS} are the magnetopause and bow shock positions.

The Boundary Fitting Approach then lets the 11 parameters in the expressions above to float, and find the best match with the 'real' or 'observed' X-ray image through a numerical fitting process. Figure 15 shows an example of the result. The top panel is the 'real' X-ray image, and the bottom panel is the best match found by the Boundary Fitting Approach which is quite similar to the 'real' image. The parameters $r_0{}^M$, $\alpha_y{}^{MP}$, $\alpha_z{}^{MP}$ corresponding to the bottom panel define the derived 3-D magnetopause. Applying this approach to different viewing geometries on the SMILE orbit, it is found that there is no apparent orbital bias.

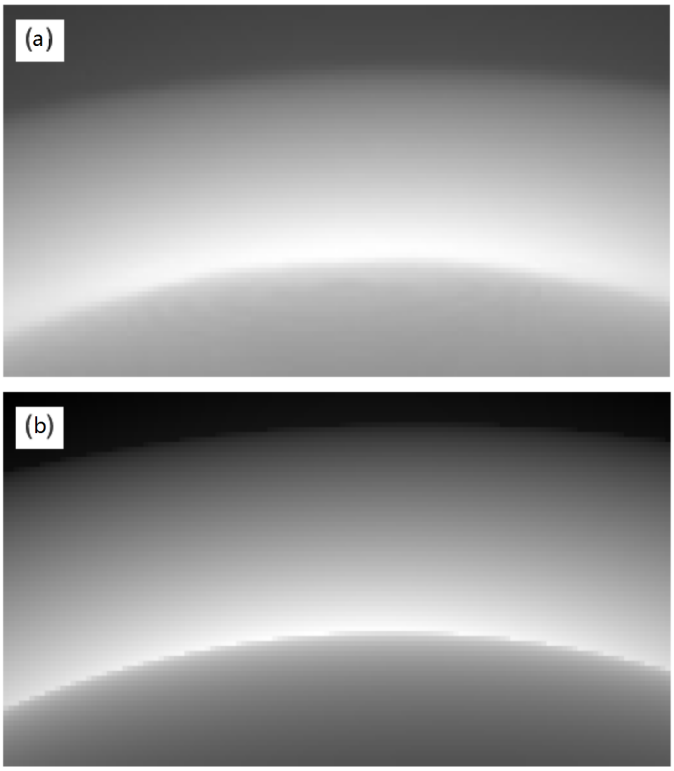

Figure 15. Demonstration of the Boundary Fitting Approach. The top panel is the 'real' X-ray image, and the bottom panel is the best match found by the Fitting Method [Jorgensen et al., 2018].

2.5.3 Magnetopause model comparison and propagation time through magnetosheath

More than 15 empirical magnetopause models have been developed in the last 30 years which define the magnetopause using different sets of spacecraft observations. Besides, the magnetopause position can be found using results of global MHD models. Samsonov et al. (2016) compared predictions of 8 empirical and 4 MHD models for typical solar wind conditions and showed that the maximum differences between the models in the magnetopause standoff distance (along the Sun-Earth line) may exceed 2 R_E and be even larger in the terminator plane. It is possible to assume an expected range of the standoff distance, however further verifications of both empirical and MHD models in their predictions of the magnetopause position would be very desirable. Samsonov et al. (2016) also estimated the effect of the ring current on the magnetopause position. Their estimation showed that the standoff distance increases by about 1 R_E in a moderate magnetic storm with Dst≈ -100 nT. The magnetopause position also depends on the Earth's dipole tilt. Samsonov et al. (2016) compared predictions of several empirical and MHD models and found that the magnetopause radial distance changes above and below the equatorial plane depending on the dipole tilt, but only Wang et al. (2013) empirical model predicts the variations of the standoff distance in dependence on the tilt.

An important problem is to calculate correctly the time of arrival of solar wind discontinuities to the magnetopause. Recently Samsonov et al. (2017, 2018) showed that the propagation time of tangential discontinuities through the magnetosheath in a typical case may be 12-14 min, i.e. about 10 min larger than from a simple estimate based on the average flow velocity in the magnetosheath. If a tangential discontinuity brings a significant density increase/decrease,

it will result in magnetospheric compression/expansion and this effect can be observed by SMILE. The magnetosheath propagation time is predicted to be even larger for a low beta solar wind such as magnetic clouds.

2.5.4 SXI field-of-view simulation

The FOV of the X-ray instrument is changing as the spacecraft moves along its orbit. A sophisticated simulator with specified orbit, visibility and FOV (Figure 16) was developed for all general Earth/orbit/magnetosheath/cusps etc. configurations (see the SMILE Website http://www.star.le.ac.uk/amr30/SMILE/ for examples of the simulator outputs). It is a very useful visualization tool, able to create movies of what can be observed from a particular orbit, and also able to calculate observability efficiencies, i.e. what percentage of the considered orbit and configuration a certain target (nose, cusp etc.) is visible or not due to the various constraints (e.g. bright Sun, bright or obscuring Earth, baffle considerations, radiation flux, etc.). Relevant environmental parameters that go into the simulator are the position and size of the cusps – here assumed to be Earth-sized and at GSE-X,Y,Z=[2.5,0.0,4.4] (North cusp) and [2.5,0.0,-4.4] (South cusp), and the position, shape and size of the magnetopause – here assumed to be a Shue-model (Shue et al. 1997) shape with α=0.6, with the nose of the magnetopause at [10.0, 0.0, 0.0]. Recently a more realistic cusp shape was introduced that uses three magnetic field lines at 10, 12 and 14 H MLT that change position with the dipole tilt and the season. The SMILE design parameters that are relevant are the FOV and orientation of both the SXI (15.5° x 26.5°, short-side along the Earth-Sun line) and the UVI (10° x 10°), the offset between these (25.4°), and the SXI Earth avoidance angle (10°).

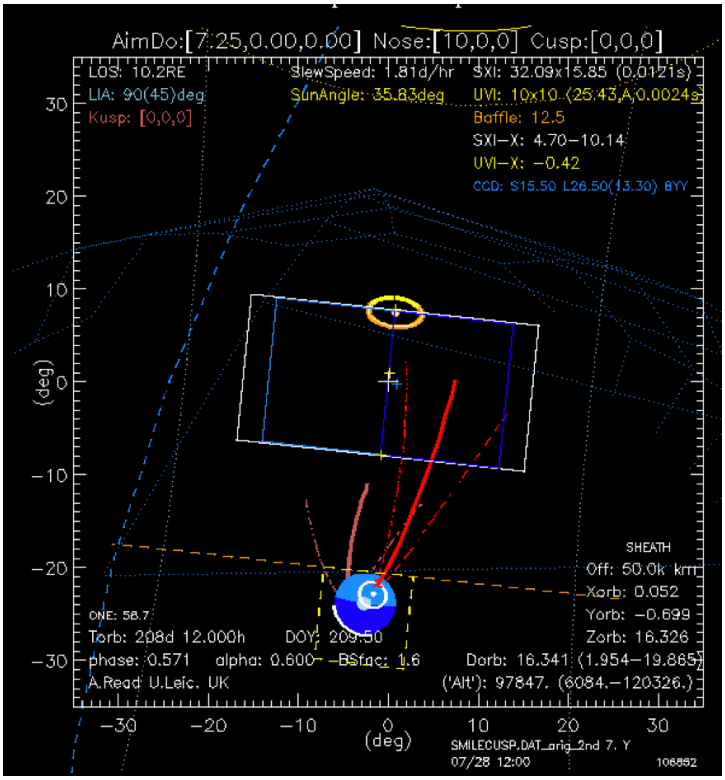

Figure 16. SXI instrument FOV (white rectangle for the baffle and blue squares for the CCDs) and UVI instrument FOV (yellow square). The nose of the magnetosphere is shown with a yellow oval at (10.0, 0.0, 0.0) R_E and the cusps are shown by the red (North hemisphere) and pink (South hemisphere) magnetic field lines (from Tsyganenko, 1997). The SXI Earth avoidance baffle angle is shown with the orange dashed line. The sun avoidance angle is shown by the large yellow unbroken curve.

The simulator takes a spacecraft orbit and these parameters as input and predicts what can be observed during the orbit. It is used to explore a number of high-ellipticity, high-inclination orbits in order to determine the optimal choice. Figure 16 shows the FOVs of SXI and UVI at a time when both the Northern cusp (red curved lines) and the subsolar point (yellow oval) are in the FOV of SXI (blue squares).

The simulator was also run to cover a complete year for various orbits with different inclinations or apogee altitudes in order to choose the orbit parameters that maximize the observation times of the science targets. Figure 17 shows the coverage of the target regions (the magnetopause subsolar point or nose and the Northern and Southern cusps) during a full year. The coverage varies as the orbit plane scans local time, being perpendicular to the Sun-Earth line in January and parallel to the Sun-Earth line in May. The regions were SXI observations are not possible are the radiation belts around perigee (below 50000 km altitude), when the Sun

(purple) or the Earth (pink) is close to or enters the SXI baffle. At all apogees the targets can be observed and during some seasons down to 50000 km of altitude. In autumn as the spacecraft is descending toward perigee SXI would have to be switched off before 50000 km since the Sun is entering or is very close to its SXI FOV (purple). The percentage of the observing time for each target is given in the 4th line at the bottom of Figure 17. For instance, the nose of the magnetosphere is observable 49.8% of the time, the Northern cusp 47.4% and the Southern cusp 21.6%. SXI would be off for 21.4% of the time due to radiation belt passage or Sun in the FOV.

Such simulations were used to choose the orientation of the SXI FOV: the long side of the FOV was chosen to be perpendicular to the Sun-Earth line since it minimizes the amount of time that the Sun is in or is close to the FOV. The simulator was also used to select the orbital period around 51 h rather than a 48h orbit which could have bad cusp coverage for certain launch dates.

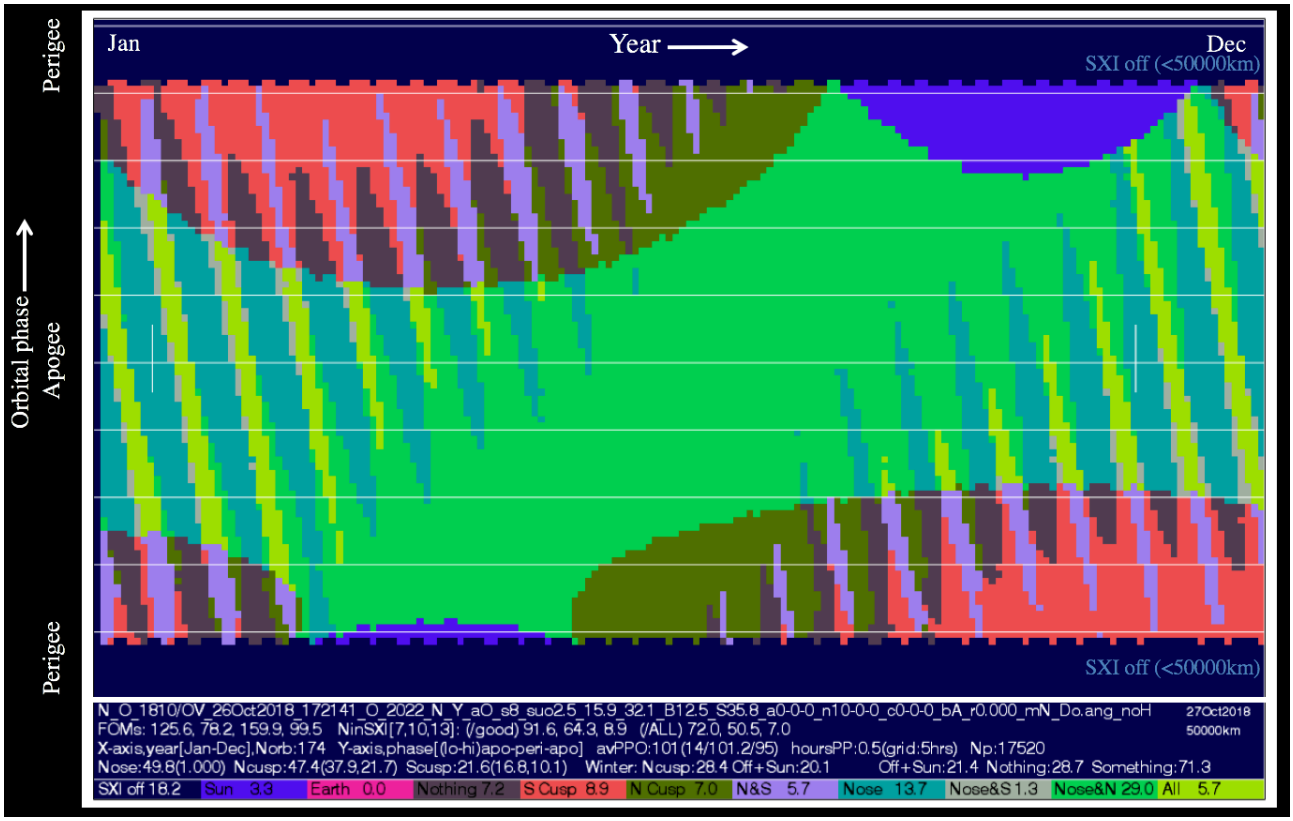

Figure 17. SXI target region coverage during one year. The x-axis shows the time during 1 year and the y-axis the time from perigee to apogee and back to perigee. Colours indicate when SXI points to the Sun (to be excluded) (purple), Earth (to be excluded) (pink), none of the targets (granite grey), the Southern cusp (orange), the Northern cusp (dark green), Northern and Southern cusps together (light purple), the magnetopause subsolar point or nose (dark cyan), nose and Southern cusp (grey), nose and Northern cusp (green), nose and Northern and Southern cusps (green-yellow). The orbit with 70° inclination and 20 R_E apogee provided by CAS was used in the simulation. SXI is switched off and its door closed in the radiation belts, below 50000 km (dark blue), to avoid CCDs degradation when subject to high radiation doses. The percentage of observability for each target region is indicated at the bottom in line number 4. Each horizontal line marks a 5h increments starting from the perigee at the bottom.

Table 1 summarises the percentages of time that the nose of the magnetosphere, the Northern and Southern cusps would be observable for the 8 different orbits analysed. Three apogee geocentric distances were analysed from 18 to 20 R_E as indicated in column 2. A 20 R_E apogee is preferred since it allows longer time above 50000 km altitude and little additional amount of fuel is needed to go from an 18 R_E to a 20 R_E apogee. A simulation was done for both 50000 km and 80000 km altitude SXI switch-off, indicated in column 6, and although the latter leads to some decrease in observation time this is not major since most observation time is spent at apogee when the spacecraft's speed is minimum. ESA and CAS are indicated in column 4 since ESA provided the initial orbits, and CAS provided the latest ones.

ID	Apo.	Launch	Source	Torb_days	Altitude	Nose	N Cusp	N Cusp (Win)	S Cusp	Any	SXI_off+Sun	SXI_off	Sun
F	18	Vega	ESA	1.9175	50000	40.18	47.03	26.81	23.51	67.08	23.36	20.13	3.23
F	18	Vega	ESA	1.9175	80000	37.37	38.02	22.73	14.6	51.52	41.82	41.47	0.35
K	19	Vega	CAS	1.96917	50000	31.49	45.96	34.31	22.69	64.21	25.03	19.32	5.72
K	19	Vega	CAS	1.96917	80000	30.67	37.12	29.12	14.95	50.08	42.11	39.45	2.67
L	20	Vega	CAS	2.11313	50000	42.13	44.41	33.27	21.88	68.32	23.63	17.85	5.78
L	20	Vega	CAS	2.11313	80000	41.42	36.67	27.96	14.7	55.66	38.96	35.96	2.99
H	20	Vega	ESA	2.10854	50000	49.86	47.54	28.8	21.54	71.19	21.39	18.14	3.25
H	20	Vega	ESA	2.10854	80000	47.16	40.03	24.21	13.94	58.06	37.	36.5	0.5
G	18	Soyuz	ESA	1.86167	50000	38.57	55.35	47.79	17.69	67.93	24.09	20.13	3.96
G	18	Soyuz	ESA	1.86167	80000	35.63	44.49	37.89	9.61	52.93	41.68	41.64	0.05
M	19	Soyuz	CAS	1.97042	50000	42.16	53.26	45.73	18.14	67.42	24.44	19.47	4.97
M	19	Soyuz	CAS	1.97042	80000	39.34	44.14	40.15	10.47	53.96	40.82	39.65	1.16
N	20	Soyuz	CAS	2.11479	50000	49.12	51.71	45.02	16.41	70.14	23.01	17.89	5.12
N	20	Soyuz	CAS	2.11479	80000	46.77	44.04	38.06	9.37	57.91	37.45	35.99	1.46
I	20	Soyuz	ESA	2.10875	50000	51.69	53.49	45.75	15.37	71.9	21.55	17.44	4.11
I	20	Soyuz	ESA	2.10875	80000	49.59	45.67	37.98	8.58	60.07	35.51	35.1	0.41

Table 1. Percentage of time when SXI observations of the science targets are possible: magnetosphere nose, Northern cusp, Norther cusp in winter, Southern cusp, any of the targets, SXI off + Sun in FOV, SXI off, and Sun in FOV (columns 7 to 14). Each line is for a given orbit with parameters given in the first 6 columns. The source of orbits is given in column 4 and the altitude considered for SXI switch off in column 6.

3 Scientific requirements

3.1 Science requirements

Science requirements are derived from the three main science questions listed below (Table 2). These are broken down in four sub-questions that address detailed science regions or physical process to be studied. Optional questions have been raised by the science study team, however, they will not drive additional requirements derived from the three main questions.

Table 2: Traceability matrix from science questions (Level 0) to the scientific measurement requirements (Level 1).

Cosmic Vision	**2. How does the Solar System work?**									
SMILE Science Theme	**Dynamic response of the Earth's magnetosphere to the solar wind impact**									
Science Questions		**L1 Requirements**								
		R1	**R2**	**R3**	**R4**	**R5**	**R6**	**R7**	**R8**	**R9**	**R10**
Q1. What are the fundamental modes of the dayside solar wind/magnetosphere interaction?	Steady/unsteady solar wind variations	●									
	Steady/unsteady motion of the dayside magnetopause		●								
	Transient brightenings and equatorward leaps in the dayside auroral oval			●	●						
	Transient brightenings and equatorward leaps in the mid-altitude cusp					●	●				
Q2. What defines the substorm cycle?	Location and motion of the dayside magnetopause boundary							●			
	Location and motion of the auroral oval								●		
	Substorm brightenings of the auroral oval									●	
	Solar wind input	●									
Q3. How do CME-driven storms arise and what is their relationship to substorms?	Location and motion of the dayside magnetopause boundary							●			
	Location and motion of the auroral oval								●		
	Substorm brightenings of the auroral oval										●
	Solar wind input	●									
Optional questions											
Q4. What are the characteristics of the aurora at small scales in the Southern hemisphere?											
Q5. What is the interaction of solar wind at comets and how does this compare with at Earth?											
Q6. How are transpolar cap arcs created during Northward IMF and how do they evolve?											

Table 3 lists the scientific measurement requirements (level 1) and the derived instrument performance requirements (level 2).

Table 3: The scientific measurement requirements (Level 1) and their traceability to the payload performance requirements (Level 2).

Scientific Measurement Requirement Level 1	Instrument Performance Requirement Level 2
R1: The solar wind and magnetosheath plasma and magnetic field should be measured at better than 2 min. time resolution	**RP1:** H+ moments (density, velocity and temperature) shall be measured at 2 min. or better time resolution with at least 20 % accuracy **RP2:** H+ velocity shall be measured up to 800 km/s **RP3:** The three components of the magnetic field B shall be sampled with at least 2 min. time resolution, 0.1 nT resolution in the solar wind and an absolute accuracy of 2 nT.
R2: For solar wind Flux > 4.9x10^8/cm^2s, the location of the subsolar magnetopause shall be determined with an accuracy better than 0.5 Earth radii (R_E) and better than 5 min. time resolution from locations on orbit greater than 15 R_E geocentric	**RP4:** X-ray images of emission gradients corresponding to the magnetopause shall be obtained with 1.5° (=arctan(0.5 R_E/20 R_E)) or better angular resolution at least every 5 min. for solar wind flux > 4.9x10^8 /cm^2s from locations on orbit greater than 15 R_E geocentric
R3: Transient brightenings of 100R or more in the dayside aurora shall be measured with a time resolution of at least 1 min	**RP6:** UV images shall have a sensitivity of 100R or better at 1 min resolution
R4: The position of features in the aurora shall be measured with an accuracy of at least 150 km at 1 min. time resolution from locations on orbit greater than 15 R_E geocentric.	**RP7:** Global UV images of the aurora shall have 150 km or better spatial resolution at 1 min. time resolution from locations on orbit greater than 15 R_E geocentric **RP8:** Auroral structures (e.g. arcs) shall have a position accuracy of 500 km with respect to the Earth's surface
R5: The poleward and/or equatorward edges of the mid-altitude cusp shall be determined with a spatial resolution of at least 0.25 R_E and a time resolution of at least 5 min for solar wind Flux > 4.9x10^8/cm^2s from locations on orbit greater than 15 RE geocentric.	**RP9:** The poleward and/or equatorward edges of the mid-altitude cusp in X-ray images shall be identified to within 0.75° (arctan(0.25 RE/20 R_E)) angular resolution at time resolution of at least 5 min for solar wind flux > 4.9 x10^8 /cm^2s) from locations on orbit greater than 15 R_E geocentric
R6: The cadence and spatial resolution of the soft X-ray imager shall suffice to determine angular equatorward/poleward motions of the mid-altitude cusp at speeds between 0.1 and 0.5° (ILAT)/min.	**RP10:** X-ray images of the mid-altitude cusp shall have a spatial resolution of 0.4° (=arctan(900 km/20R_E)) or better at temporal resolution of 4 min. from locations on orbit greater than 15 R_E geocentric and for solar wind flux > 9x10^8 /cm^2s .
R7: For solar wind flux >3.6e8 /cm^2s , the location of the subsolar magnetopause shall be determined with a spatial accuracy better than 0.5 R_E and a time resolution better than 10 min. from locations on orbit greater than 15 R_E geocentric	**RP11:** The position of the subsolar magnetopause shall be identified with at least 1.5° (arctan (0.5 R_E/20 R_E)) angular resolution at time resolution of 10 min. from locations on orbit greater than 15 R_E geocentric
R8: The poleward and equatorward boundaries of the auroral oval shall be identified at all local times with a spatial resolution of at least 300 km at 1 min. time resolution from locations on orbit greater than 15 R_E geocentric	**RP12:** UV auroral images with better than 300 km spatial resolution shall be obtained at 1min time resolution from locations on orbit greater than 15 R_E geocentric

R9: Transient brightenings of 100R or more in the aurora shall be measured with a cadence of at least 1 min.	**RP6:** UV images shall have a sensitivity of 100R or better at 1 min resolution
R10: 200R changes in brightness of 30 kR aurora shall be identified and measured with a cadence of at least 1 min.	**RP13:** UV variations of as little as 200R upon backgrounds of 30kR shall be obtained at 1 min time resolution.
R2, R5, R6, R7	**RP14:** X-ray images in the energy band 0.2 - 2.5 keV shall be obtained **RP15:** The field of view of SXI shall be at least 26.5x15.5°

3.2 Mission requirements

Table 4 summarizes the major requirements at the mission level.

Table 4 Mission and spacecraft level requirements

Mission requirements
R11 Orbit requirements
• The apogee of the orbit shall be 20 Re +/- 2 Earth radii geocentric distance • The perigee of the orbit shall be above 5000 km altitude • The inclination of the orbit shall be 90+/-27° • The argument of perigee shall be in the range 225-315°
R12 pointing requirements
The spacecraft pointing accuracy shall be: • Absolute Pointing Error (0.5°), • Attitude Knowledge Error (0.5°), • Attitude stability 0.05°/1 min (UVI), 0.5°/10 min (SXI) or better
R13 Electromagnetic compatibility (EMC) requirements
• The magnetic disturbance from the spacecraft shall be less than 10 nT DC at the outboard MAG sensor • The absolute spacecraft surface potential relative to the surrounding plasma shall be less than 30V in solar wind and magnetosheath.

An example of the orbit fulfilling the mission requirements is shown on Figure 18. During moderately strong solar wind flux (B=6 nT, Nsw=12 cm^{-3} and Vsw=400 km/s), the spacecraft will reach the solar wind near apogee and a direct comparison between the solar wind strength impacting the Earth and the X-ray images of the cusps/magnetostheath and the auroral UV images will be made.

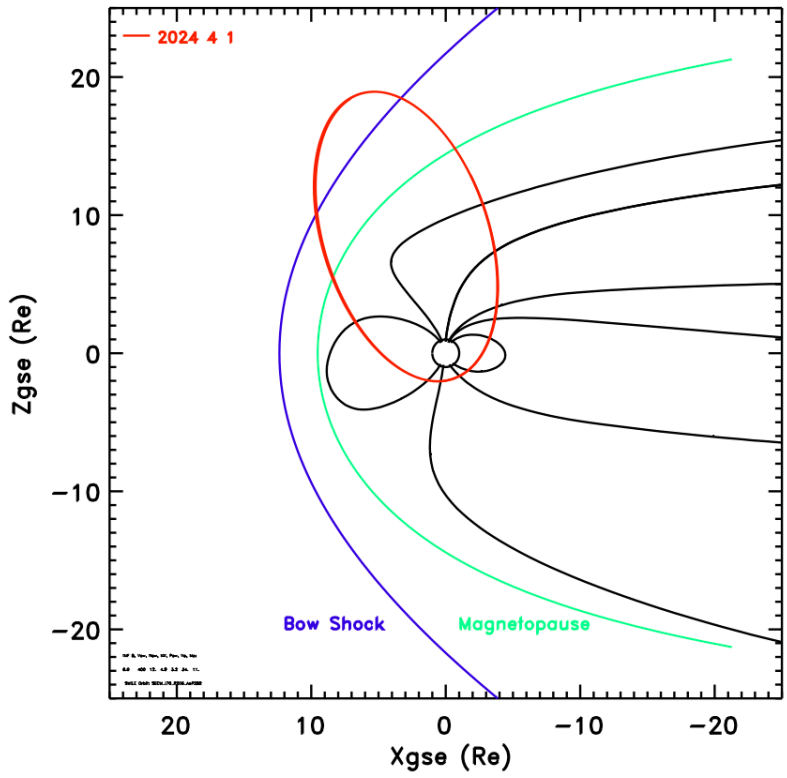

Figure 18. SMILE orbit (red) on 1 April 2024 with an inclination of 67° in X-Z_{GSE} coordinate system. The Earth magnetic field lines (black lines connected to the Earth), the magnetopause model from Shue et al. (1997) (green) and the bow shock model from Merka et al. (2005) (blue) are shown for the solar wind parameters: B=6 nT, Vsw=400 km/s, Nsw=12 cm^{-3}, NV=4.9 x 10^8 $cm^{-2}s^{-1}$).

4 Payload and Performance

The SMILE mission payload consists of the Soft X-ray Imager (SXI) which will spectrally map the Earth's magnetopause, magnetosheath and magnetospheric cusps, the Ultraviolet Imager (UVI) dedicated to imaging the auroral regions, the Light Ion Analyser (LIA) and the MAGnetometer (MAG), which will establish the solar wind properties simultaneously with the imaging instruments. As it will be detailed in this section, the expected sensitivity, accuracy, time resolution and remote sensing field-of-view of these instruments are in line with the SMILE science requirements. In other words, their key technical characteristics will enable to fulfil the scientific objectives of the mission.

4.1 The Soft X-ray Imager: SXI

The soft X-ray Imager (SXI) is developed by the University of Leicester with contributions from other institutes in the UK, Austria, Hungary, Spain, the Czech Republic, Norway, Ireland and China. SXI will observe the location, shape, and motion of dayside magnetospheric boundaries, including the bow shock, magnetopause, and cusp regions in the soft X-ray band. SXI will also measure the time-dependent solar wind composition from the brightness of the SWCX X-ray emission lines.

4.1.1 SXI Instrument Description

The Soft X-ray Imager (SXI) is shown in Figure 19 and consists of four major hardware units described below.

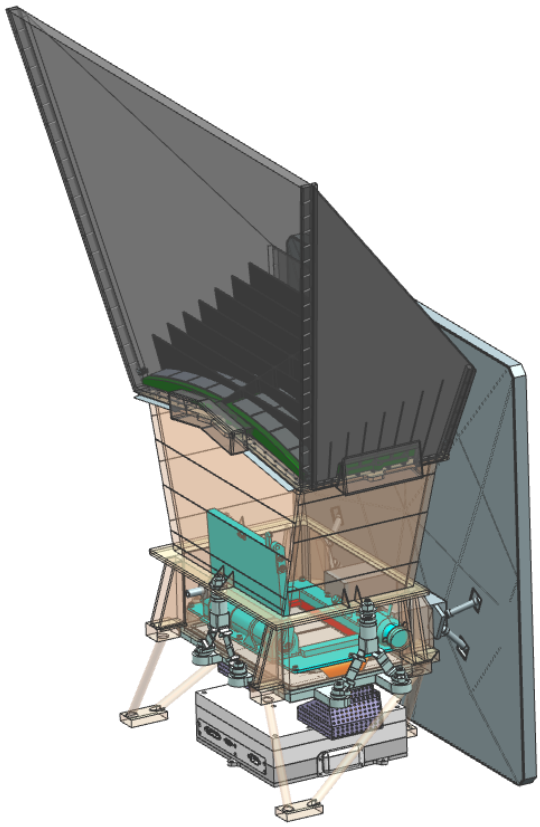

Figure 19. CAD model of the SXI Telescope and Front End Electronics

4.1.1.1 *SXI Telescope*

The SXI telescope comprised the actual image forming and detecting system of SXI and includes:

- the Telescope Tube Structure,
- the micro pore optic (MPO) plates with optical filters, MPO mounting frame and electron diverter,

- the Straylight Baffle Structure with internal baffle vanes,
- the Detector Plane Assembly with the CCD detectors, thermal disconnects to the telescope tube and a set of thermal straps to the SXI radiator
- the Radiation Shutter Assembly with the actual radiation shield door and door mechanism.

The SXI Telescope interfaces mechanically to the PLM base plate via three bi-pods made from titanium alloy.

4.1.1.2 *Thermal Control System*

The thermal control system provides the required thermal environment for the focal plane arrays. The thermal control system encompasses the actual radiator, radiator support structures and thermal blankets.

4.1.1.3 *Front End Electronics Assembly*

The Front End Electronics (FEE) assembly comprises the actual front end electronics and its housing. The FEE assembly is mounted to the PLM base plate and interfaces with the focal plane detectors and the back end electronics.

4.1.1.4 *Back End Electronics Assembly*

The back end electronics is mounted in a separate chassis and includes the Power Supply Unit (PSU) providing secondary supply power to all SXI electronics units, the Data Processing Unit (DPU) with associated boot and flight software and the Radiation Shutter Electronics (RSE). The Back End Electronics Assembly is mounted to the PLM base plate and interfaces with the FEE assembly, the radiation shutter assembly and the PSU and mass memory unit of the PLM.

4.1.2 SXI System Architecture

SXI development is led by the University of Leicester with involvement from many European institutes . ESA is responsible for the procurement of the SXI CCDs and PSU. In the case of the CCDs, the Open University, UK, are responsible for their testing and calibration once issued to the project. Responsibilities for individual tasks within the instrument ground pipeline software (PPS) are split within the SXI consortium and the University of Leicester has overall responsibility for the delivery of the PPS.

4.1.3 SXI Instrument Design

4.1.3.1 *Optic Assembly and Straylight Baffle*

The SXI uses micro pore optics (MPOs) in a Lobster-eye configuration (Figure 20). MPOs are essentially square pore microchannel plates heat slumped to a hemispherical radius of curvature. They are manufactured by PHOTONIS France S.A.S., and have been developed by the University of Leicester in collaboration with PHOTONIS with input from ESA. The same technology is used in the MIXS Instrument on the ESA BepiColombo Mission.

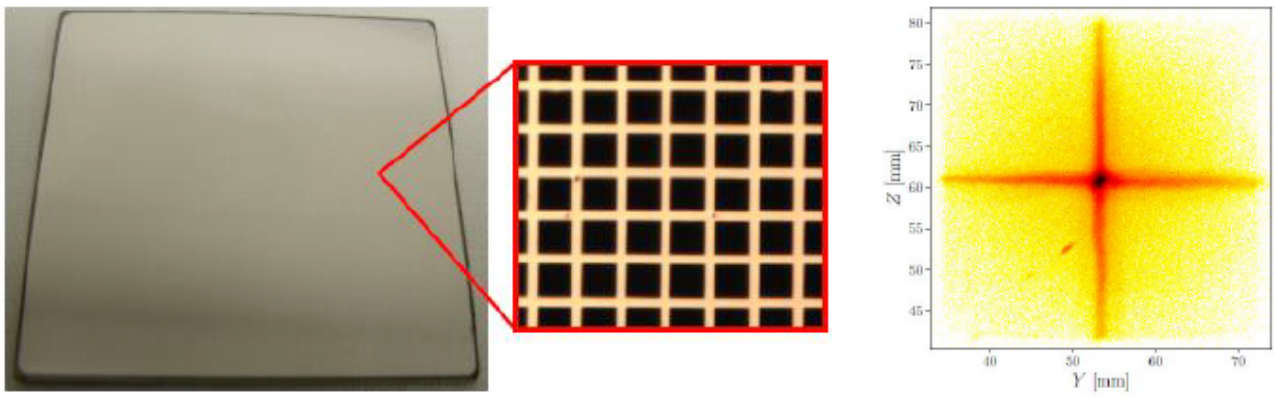

Figure 20. SMILE SXI breadboard MPO plate (left) with micrograph of pore structure (centre) and measured point-spread function (PSF) showing the typical cross arm structure. The offset "blob" is a detector defect.

The SXI MPOs are 4 cm x 4 cm plates with a 600 mm radius of curvature (300 mm focal length). Each plate is 1.2 mm thick with channels of width 40 μm (the open area fraction is around 60%). The channel walls are coated with iridium to enhance the reflectivity and a film of aluminium (baseline 100 nm thickness) is applied to the top surface of the MPO to block optical and UV photons.

Sitting above the optic plane is the straylight baffle (see Figure 19) designed to block sunlight and earthlight entering the aperture of the instrument.

4.1.3.2 *Detector Plane Assembly and CCD Detectors*

The SXI detector plane consists of two e2v CCD370 devices. The CCDs are derivatives of the CCD270 devices used for the ESA PLATO mission but optimised for X-ray detection and enhanced radiation hardness. The CCD native pixel size is 18 μm but will be on-chip binned by a factor of 6 leading to a 108 μm effective pixel size. The total physical dimensions (area) is 8.12x 8.12 cm (including store area) per CCD. The CCDs will be operated using 719 rows as an asymmetric frame store. The frame integration time is anticipated to be around 4 seconds. Two thermal straps connect the CCDs to the radiator assembly (Section 4.1.3.4). The CCDs expected energy resolution is ~50 eV (FWHM) at 0.5 keV and are expected to be able to detect X-ray photons between an effective energy range of ~0.15 to 2.5 keV. Above this energy the expected induced particle background will dominate the signal.

4.1.3.3 *Radiation Shutter*

A radiation shutter mechanism (Figure 21) is employed to limit the radiation dose accumulated by the CCDs to a range acceptable for standard CCD technology. The radiation shutter is closed during each perigee pass below an altitude of around 50000 km. During each orbit the radiation shutter remains in the closed position for around 9 hours. The radiation shutter may also be closed if the spacecraft needs to change its pointing direction to avoid sunlight entering the SXI Telescope aperture or if a particularly strong solar energetic particle event is detected.

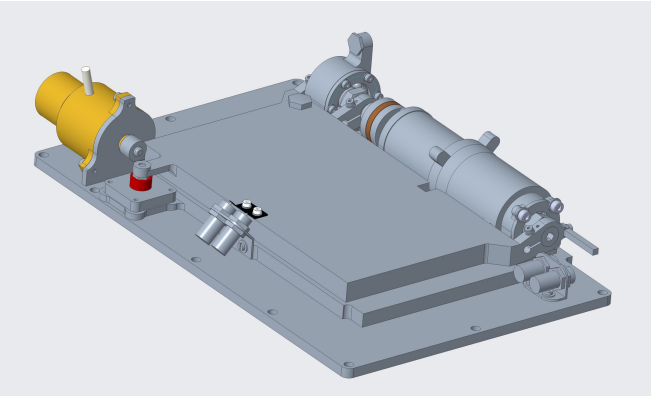

Figure 21. Radiation Shutter Mechanism in the closed position. The pin-puller which releases the launch lock is shown on the top left. To the right is the motor mechanism with redundant windings.

4.1.3.4 *Thermal Control System*

The Thermal Control System (TCS) is designed to keep the CCDs within an acceptable temperature range for science operations (between -95ºC and -120ºC). The TCS is a passive system consisting of an external radiator and heaters and temperature sensors near the CCDs. Two thermal straps connect the CCDs to the radiator. Temperature sensor data is communicated via the FEE to the DPU which controls the heater outputs.

4.1.3.5 *Front End Electronics*

The Front End Electronics (FEE) box is connected to each CCD via flex cables protected by EMC shields. The FEE also benefits from PLATO heritage except for the need for an FPGA programmed to run the on-board event detection algorithm. (SXI detects individual X-ray photons whereas the PLATO CCDs are operated in an optical integration mode).

4.1.3.6 *Back End Electronics*

The Back End Electronics DPU and associated on-board software (OBSW) controls the SXI instrument. It receives telemetry (TM) from the FEE (photon lists) and packages it with housekeeping data (with or without compression) and sends it to the spacecraft mass storage. It can intelligently throttle the information content of the telemetry to ensure SXI keeps within the TM allocation. The DPU switches between instrument modes where necessary to ensure the instrument is safely operated. The OBSW will be designed to independently detect enhanced radiation or optical signatures within the CCD data and close the RSM if required according to programmable thresholds. The back end electronics contain both a nominal and redundant DPU/RSE/PSU chain.

4.1.4 SXI Interfaces and Resources

4.1.4.1 *Mass*

Unit	Design mass [kg]	Maturity margin	Nominal mass [kg]
Telescope	14.98	19.30%	17.87
PSU/DPU	8.02	15%	9.22
Thermal control	6.34	20%	7.62
Harness	1.07	20%	1.28
Total mass			**35.99**

Table 5. SXI Mass budget. Margin depends on heritage.

4.1.4.2 *Power*

The total power used by the instrument varies between 17 and 66 W and the nominal operation power is 51 W.

4.1.5 SXI Instrument Performance

The SXI instrument parameters are shown in Table 6.

Parameter	Value (at 0.5 keV if relevant)	Comment
Optic focal length	300 mm	
MPO pore size	40 μm	
MPO pore length	1.2 mm	L/D = 30:1
Optic coating	Iridium	
PSF FWHM	8.1 to 9.6 arcminutes	Across 60% of the detector plane
PSF HEW	~2.8 degrees	
Optic total effective area	14.6 cm^2	At centre of FOV
Optic FOV	32.1° x 15.8°	
Straylight baffle vignetting	~0.9	
CCD QE	0.89	
CCD energy resolution	50 eV (FWHM)	Assuming 4.5 e^- noise, No CTI
CCD frame integration time	~4 seconds	

Filter Transmission	0.82	Assuming 100 nm Aluminium
Total instrument effective area	9.6 cm^2	
Instrument FOV	26.5° x 15.5°	For a flat detector plane at ~302 mm from centre of optic.

Table 6. SXI Instrument Parameters

The ability of the SXI to meet the science requirements of the mission and instrument are demonstrated by simulation. This depends not only on calculations of the expected signal strength of the primary science target (solar wind charge exchange emission within the magnetosheath and cusps) but also the expected background signal from the astrophysical soft X-ray background and the particle induced background. In the band 0.15 to 1.1 keV containing the bulk of the foreground SWCX signal, the dominant source of background are astrophysical X-rays.

SW Flux	**2.0 x 10^8 cm^{-2} s^{-1}**	**4.9 x 10^8 cm^{-2} s^{-1}**	**1.5 x 10^9 cm^{-2} s^{-1}**
SWCX rate	0.024	0.097	0.41
SXRB rate	0.078	0.075	0.075
PB rate	0.0012	0.0012	0.0012
Time for SNR = 3σ	1572 s	167 s	26 s

Table 7. Indicative sensitivities for a 1.0 degree pixel in the SXI FOV towards the magnetopause sub-solar point for three solar wind strengths. SWCX is the charge exchange signal, SXRB the soft X-ray background signal and PB the particle background. Rate is given in counts per pixel per second integrated over the energy band 0.15 to 1.1 keV.

Table 7 shows the indicative sensitivity (time to achieve SNR = 3 to detect the SWCX signal above the background) for a 1 degree size pixel in the SXI FOV in the line of sight towards the expected sub-solar magnetopause position derived from three MHD (PPMLR) simulations of varying solar wind strength.

To demonstrate that SXI meets the science requirements, simulations are performed for the detection of the magnetopause boundary within an SXI image. Two methods have been applied to date. Forward Modelling uses a parameterised empirical model of the 3D X-ray emissivity to derive a simulated SXI image (representing the model) which is then compared with a simulated SXI image derived from an MHD simulation. The parameters of the input model are adjusted to minimise the least-squares difference between the model SXI image and the representative SXI dataset. The technique automatically returns the magnetopause location (a parameter of the model) and its error. The second technique is to associate the peak of the image in the SXI dataset with the subsolar magnetopause location and derive the error on the location with an X-ray peak finding technique. Figure 22 shows the derived error on the magnetopause location for both techniques for similar solar wind strengths. The results are consistent.

Method	Flux	ΔRO_{mp}
Forward Model	4.9 x 10^8	~0.22 RE
	9.0 x 10^8	~0.13 RE
X-ray peak finding*	4.5 x 10^8	~0.36 RE
	8.0 x 10^8	~0.23 RE

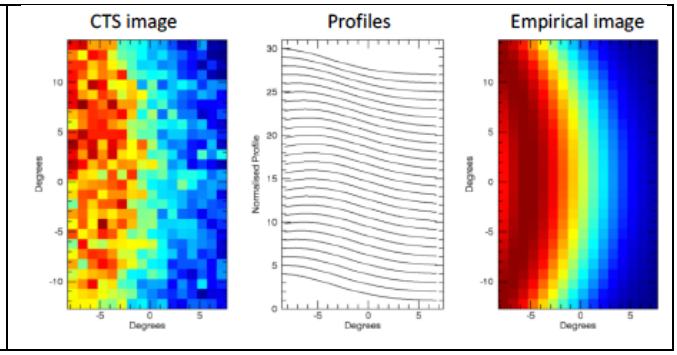

Figure 22. (Left Panel) Determination of the error on the magnetopause boundary for two different methods; Forward Modelling and X-ray peak finding. (Right panel) Example SXI image (left) and empirical model image used to find the X-ray peak position and error along the Earth-Sun line (horizontal line at Y=0 degrees).

4.2 The Ultraviolet Imager: UVI

Simultaneously with the SXI observations the UVI instrument will monitor Earth's Northern aurora to link the processes of solar wind injection into the magnetosphere with those acting on the charged particles precipitating into the cusps and eventually the aurora. The UVI will employ new filter technologies and an innovative telescope design to obtain UV images of the aurora even in sunlit conditions. UVI is developed by the University of Calgary and the Canadian Space Agency with contributions from Belgium and China.

4.2.1 UVI Instrument Description

The Ultraviolet Imager (UVI) is shown in Figure 23 and consists of two major hardware units described below.

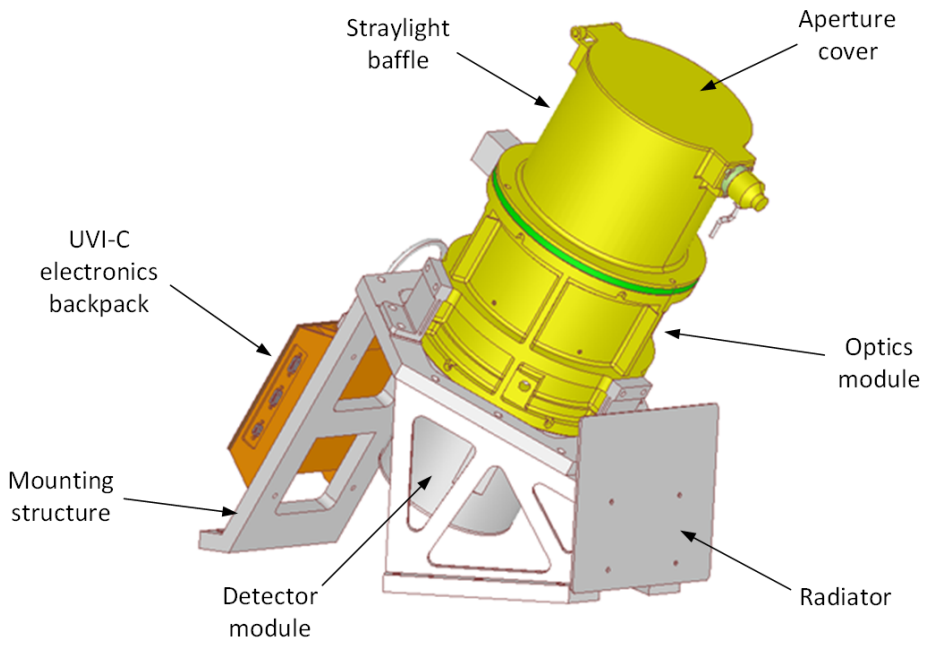

Figure 23. CAD model of the UVI camera (UVI-C).

4.2.1.1 *UVI Camera Unit (UVI-C)*

The UVI-C unit consists of the following sub-assemblies:

- The Optics Barrel Assembly comprising the telescope optics and the telescope tube,
- The Detector Assembly consisting of a MgF2 window, micro channel plate (MCP) image intensifier, fibre optics taper and CMOS detector,
- The Digital Electronics Assembly containing the detector readout electronics and the components for the interface to UVI-E.
- The Baffle Assembly comprising the actual stray light baffle, an aperture cover and associated aperture cover release mechanism,
- The Radiator Assembly including the radiator, radiator mounting structure and thermal straps to the Optics Barrel and Detector Assembly.

The UVI-C Optics Barrel Assembly, Detector Assembly, and Baffle Assembly are mounted on the PLM via the Spacecraft Interface Mount, which also provides thermal insulation to the PLM base plate.

4.2.1.2 *UVI Electronics Box (UVI-E)*

The UVI-E unit (Figure 24) is contained in a separate chassis and comprises the high voltage power supply, thermal control electronics, power conditioning electronics and instrument control electronics/DPU. The UVI Electronics Box is mounted on the PLM base plate and interfaces with UVI-C as well as the PSU and the mass memory unit of the PLM. UVI-E and UVI-C are connected via an instrument internal harness (UVI-H).

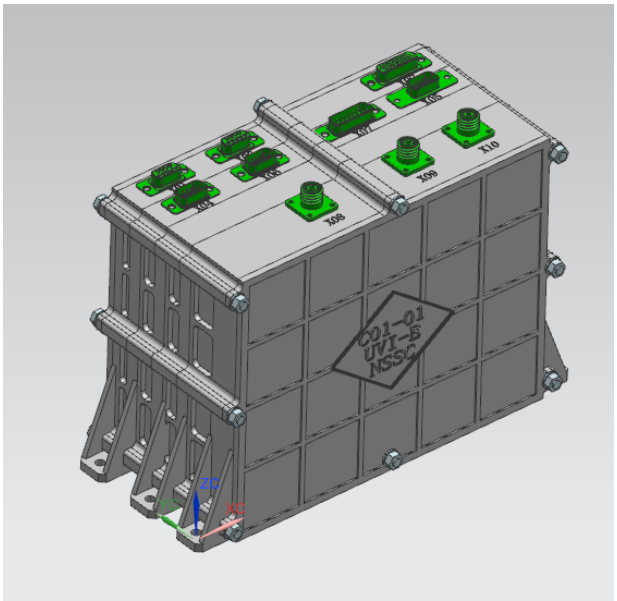

Figure 24. CAD model of the UVI Electronics Box (UVI-E).

4.2.2 UVI System Architecture

At the top level, UVI is broken into three logical partitions: UVI-Camera (UVI-C) and UVI-Electronics (UVI-E) connected via a harness (UVI-H). This partitioning also represents the division of responsibilities between the Canadian (UVI-C & UVI-H) and CAS contributions (UVI-E). The UVI-C unit further contains contributions from CSL, Belgium in the form of mirror coating design and manufacture. In order to de-risk this contribution, a backup plan based on commercial filter coatings is pursued in parallel.

4.2.3 UVI Instrument Design

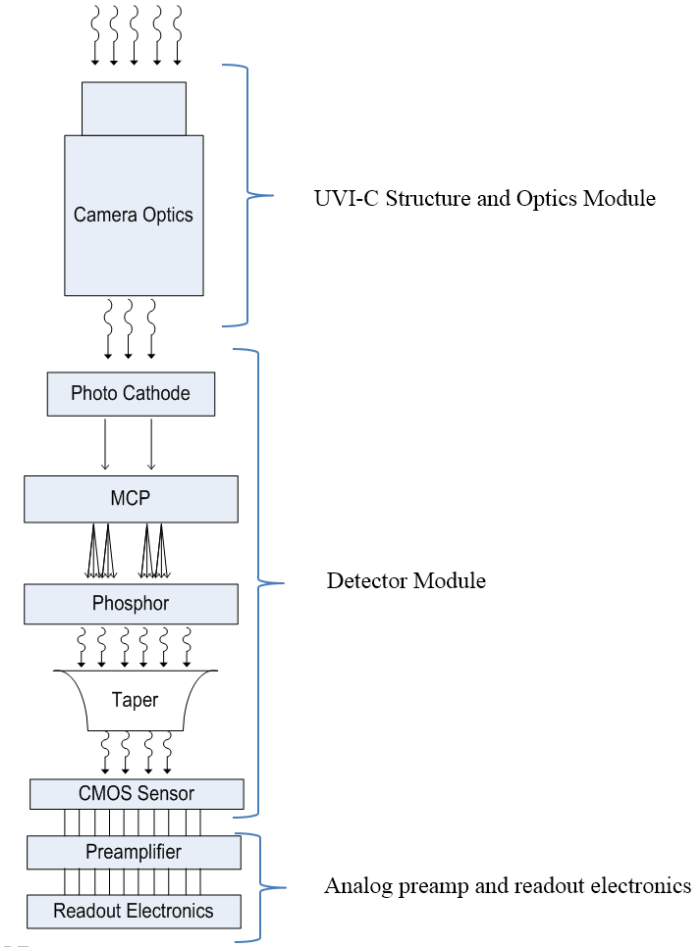

Figure 25. The main components of UVI-C.

4.2.3.1 *Optics module*

The optics module comprises the optical mirrors themselves, the mechanical housing for the mirrors (the optics barrel) and the mechanical mount to the PLM. The UVI optical design philosophy is based on an on-axis, 4-mirror system (see Figure 26), optimized for the SMILE orbit and the required cadence and spatial resolution. The 4-mirror on-axis telescope has been shown to outperform off axis imagers in the area of light gathering ability per unit mass and provides an optimal solution for low light imaging on a mass limited platform. The four mirror system also has the advantage of providing four reflecting surfaces for depositing thin-film reflective coatings to enable isolation of the desired passband.

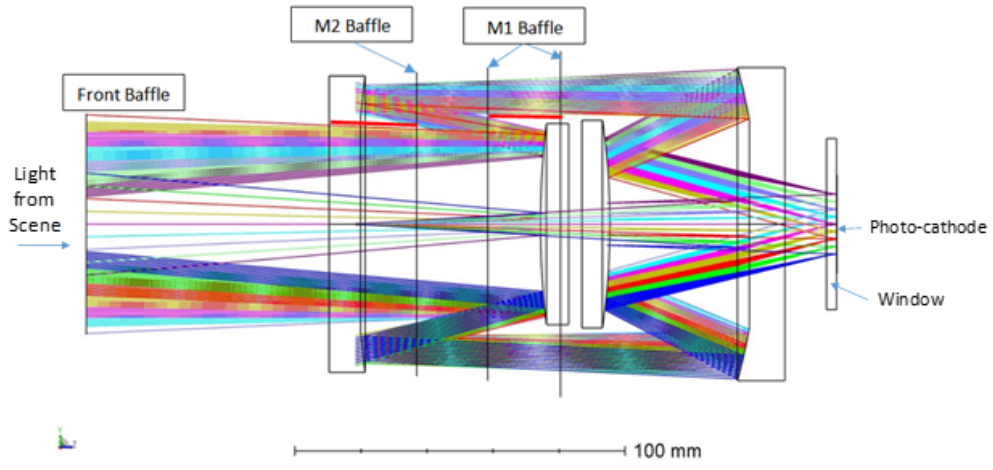

Figure 26. Optics layout of UVI. Light enters the system from the left.

Recent advances in UV filter technology coupled with the 4-mirror design provides orders of magnitude greater visible light suppression than previous auroral missions and is an enabling factor for the UVI science objectives. The mirror coatings will be developed by Centre Spatial de Liege (CSL) in Belgium.

The actual optical mirrors are contained inside the optics barrel, which will provide the mounting points for optical mirror mounts, the straylight baffle and the detector module. The barrel will also contain stray light control surfaces (i.e. vanes) as required by the optical performance, and will connect to the isostatic mounts of the UVI-C structure, which is the interface to the PLM.

4.2.3.2 *Detector module*

The detector module is mounted to the optics module such that the image plane is formed at the entrance window of the detector module. The detector module comprises a micro-channel plate (MCP) based image intensifier optically coupled to a CMOS detector. The telescope optics images the light onto the MCP which is coated with a suitable photocathode material. The photoelectrons are amplified by the MCP and converted back to light again with an aluminium coated phosphor. A fibre taper transfers the light from the MCP to the CMOS detector. As a result of the image sizes in the system, a straight fibre taper is anticipated. The baseline detector is a 1024×1024 pixels STAR1000 CMOS sensor. A 5 mm thick magnesium fluoride window is forming the entrance to the sealed detector system. This type of window was utilized on Polar UVI and has shown successful performance in this application. A simplified image of the detection system is shown in Figure 25.

The mechanical structure of the detector module will house the entire detection system and is subject to the mechanical, thermal and radiation requirements of the components. The mechanical system will connect directly to the telescope tube and provide an interface to the readout electronics and preamp.

4.2.3.3 *Straylight baffle and aperture cover*

The stray light baffle will be mounted at the “front” of the telescope, meaning at the entrance of the optical assembly. The stray light baffle will be designed to minimize stray light at the focal plane during operations and protect the optical telescope from contamination during AIT and during transfer to the final orbital configuration. In addition, an “open once” aperture cover will enable cleanliness and contamination requirements applicable to the UVI optical components, particularly the thin-film coatings. It is anticipated that the aperture cover can be open and manually closed several times during ground testing, remain closed throughout launch and transfer orbit, and be opened and stay open for the remainder of the mission.

4.2.3.4 *UVI-C thermal control*

The Detector Assembly requires thermal control to be operated in the temperature range of -5°C ±5°C. For this, a passive radiator is attached to the UVI structure providing a heat sink while the cold side connects to a thermal strap that interfaces with the CMOS sensor in the detector module. In coordination with the external radiator, heaters are used to maintain the temperature range and stability required by the components of the focal plane detection system. Temperature sensors are placed at optimized locations in the focal plane assembly to assess and control the temperature of the focal plane detection system and maintain performance. In addition, a set of decontamination heaters will be attached to the main telescope structure allowing in-orbit bake-out as required.

4.2.3.5 *UVI-C electronics backpack*

UVI-C comprises a set of front end electronics (derived from the UVIT mission) that serve to interact with the CMOS array, control the imaging parameters, provide the safety interlock for a bright object detection algorithm and control the trim heaters for the detector and optics modules.

The readout and preamp electronics will directly interact with the CMOS detector, reading the images from the CMOS array and controlling the cadence, on-chip binning, readout rate, etc. The analogue readout electronics are connected to the digital electronics, together comprising the UVI-C electronics system. The

digital electronics will provide a buffer between the analogue electronics and UVI-E electronics. It will record metadata (e.g. temperatures) for the purpose of controlling the heaters housed in the telescope and detector assembly and internal to the electronics. Other functionality foreseen is the implementation of a safety control for the detection of bright objects in the field of view and the subsequent shut-down of the HV power to the intensifier. A main driver of the digital electronics is to minimize the complexity of the interface between UVI-E and UVI-C, allowing for a simpler ICD and reduced risk. The digital electronics are the connection point on UVI-C to UVI-E.

4.2.3.6 *UVI-E electronics*

The all FPGA-based UVI back end electronics (UVI-E), contained in a separate chassis mounted on the PLM base plate, provides the support infrastructure for the operation of UVI-C and is the spacecraft interface for the instrument. The UVI-E provides low voltage for all elements of UVI, including the thermal control electronics, tuneable high voltage for the image intensifier system of UVI-C and science data handling and the TM/TC interface to the PLM on-board computer. The National Space Science Center (CAS/NSSC) is independently responsible for the design, construction and test of UVI-E.

UVI-E will have an independent mechanical housing (see Figure 24) mounted on the PLM base plate. The housing is connected to UVI-C via the UVI-H harness.

4.2.4 UVI Interfaces and Resources

4.2.4.1 *Mass*

Unit	Design mass [kg]	Maturity margin	Nominal mass [kg]
UVI-C	9.25	21.19%	11.21
UVI-H	0.39	30.77%	0.51
UVI-E	3.58	12.01%	4.01
Total mass			**15.73**

Table 8. UVI mass budget.

4.2.4.2 *Power*

UVI operating mode	UVI-C			UVI-E		Total [W]
	Analogue electronics	Heater	Digital electronics	Computer board	Power module	
Imaging – hot case	0.881	0.15	1.586	4	6	15.917
Pin puller active	0.881	0	1.581	4	9	18.762
Imaging – cold case	0.881	5.5	2.272	4	8	23.953
Safe mode – cold survival	0	7.5	0	4	4.5	19.3
Idle – hot case	0.881	0.15	1.586	4	6	15.917
Idle - cold case	0.881	5.5	2.272	4	9	24.953

Table 9. UVI power budget. All values in Watts.

4.2.5 UVI Instrument Performance

A summary of the top-level performance requirements for the UVI instrument is shown in Table 13.

Field of View	10×10 degrees
Spatial Resolution	150 km @15 Re
Temporal Resolution	60 s
Spectral Band	160 - 180 nm
Detection Threshold	100R @60 s cadence, SNR greater than 1
Dynamic Range	30kR

Table 10. Top-level performance requirements for UVI.

4.2.5.1 *Instrument design parameters*

Given the science requirement to instantaneously image the entire region above 40° geomagnetic latitude at altitudes of greater than 15 R_E, the UVI imager was designed with a field of view of 10 degrees. This field of view is sufficient to image the entire Area of Interest from 15R_E altitude and will allow for a full view of a typical oval down to approximately 11R_E altitude.

Considering constraints given by the relatively low signal expected on orbit and the intrinsic connection between spatial and temporal scales of the auroral precipitation, there is a fundamental limit on spatial resolution averaged over the entire auroral region as well as an optimum image cadence for any given spatial resolution. For UVI, a combination of 150 km spatial resolution at apogee and 60 seconds imaging cadence was found to be optimal.

The need to image the aurora at all local times places requirements on the spectral band of UVI. The identification of a spectral band in which it is functionally possible to distinguish aurora from Earth's albedo and nominal dayglow processes is critical to the success of the mission. The baseline design of UVI will target the 160 - 180nm LBH-L (Lyman-Birge-Hopfield Long) band, based on the following assessments: First, images in the LBH have been historically utilized to image the dayside aurora, allowing the use of previous data to base instrument models on. Second, analysis of the LBH-L vs. for example LBH-S (Lyman-Birge-Hopfield Short) signals has shown that at lower incident flux levels the LBH-S can more readily become overwhelmed with in-band dayglow signals, and lastly, the LBH-L band alone is enough to determine the incident electron energy flux.

Detection threshold and dynamic range of the UVI imager are driven by the scientific requirement to observe weak auroral structures in the same image as relatively bright ones. This enables identification of aurora features and weak boundaries within the same auroral image. Through detailed analysis of previous auroral UV data e.g. from the Polar-UVI mission, an upper bound on luminosities expected in the SMILE-UVI images could be derived. Including a wide margin on these numbers the requirement that the instrument shall be capable to detect luminosities up to 30kR was set. Likewise through analysis of heritage data, the requirement for the lower threshold or detection limit was derived. Figure 27 shows a two dimensional histogram (panel a on the left) derived from Polar-UVI data of the dependence of photon count rate variability on the intensity of the aurora for an object of 20 km scale size. The minimum in the curve means that objects of this scale will not vary on a luminosity scale of less than this threshold. Panel b to the right summarises these results for all spatial scales studied and indicates a physical tie between the spatial scale of an object and its variability in terms of luminosity. The baseline spatial resolution of 150 km results in a detection threshold of approximately 1 photon/cm2/s, equivalent to ~100R to reasonably view objects on those scales in the LBH bands. Further, to facilitate the identification of objects at this luminosity level, the baseline SNR at the detection limit will be greater than 1, with a target of 2.5.

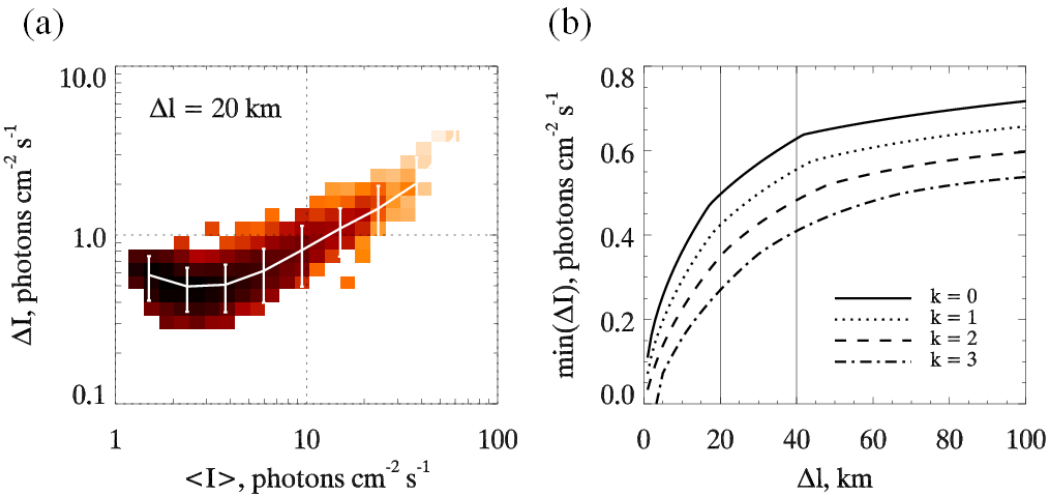

Figure 27. Characteristic variability of the photon flux emitted from the nightside auroral oval as a function of spatial scale based on scale-invariant extrapolation of POLAR UVI data.

4.2.5.2 *Modelled instrument performance*

The modelled spatial resolution of the system is shown in Figure 28. This MTF curve is inclusive of the detector sampling with no binning.

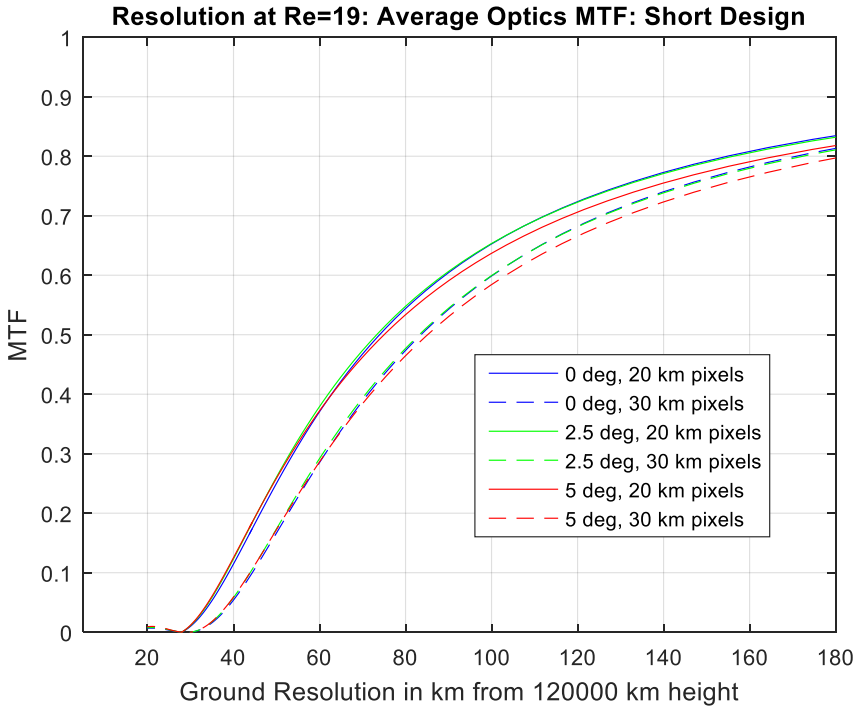

Figure 28. Modelled spatial resolution of the UVI system.

The MTF value is above 0.5 for all ground resolutions of greater than ~85 km for all field angles within the image. This implies that two structures separated by ~85 km will be resolved by the UVI instrument @19Re altitude, in the absence of binning. The nominal baseline is to make use of 4x4 binning. There is sufficient SNR to support imaging at this system MTF level (0.2). Binning at the 2x2 level would provide improved contrast and may be used as the data rates and volumes allow.

From a throughput standpoint, the analysis of photon hit rates within the radiometric budget shows that at detection threshold (100R), in 60 seconds 3.5 photons are maintained. This includes a 2.0 photon requirement, and a 1.5 photon system margin. Within the full radiometric model, the system meets the detection threshold requirements set out for UVI.

4.3 The Magnetometer: MAG

The magnetometer experiment MAG is developed by the National Space Science Center in China with contributions from Austria. The scientific goal of MAG is to measure the orientation and magnitude of the solar wind magnetic field.

4.3.1 MAG Instrument Architecture

The MAG instrument employs a digital fluxgate magnetometer system consisting of two individual tri-axial fluxgate sensor heads mounted on a deployable 3 m boom. The deployable boom is mounted on the PLM on a set of PLM owned mounting brackets. The sensor heads are connected by harness to an electronics box mounted on the PLM. The electronics unit consists of a FPGA based digital processing unit, a DC/DC converter and dedicated front-end electronics for each of the magnetometer sensors. The main parameters of the MAG instrument are summarised in Table 11:

Dynamic range	±12800 nT
Digital resolution	24 bit
Sampling rate	40 Hz
Accuracy	2.0 nT
Data rate	6 kbps

Table 11. Main parameters of the MAG instrument. MAG also provides a ground mode with a dynamic range of ±64000 nT.

4.3.2 MAG Instrument Design

4.3.2.1 *Fluxgate sensor*

Each of the two MAG sensor heads comprises three ring-core fluxgate sensors oriented along three orthogonal axes, thus sampling the three spatial components of the local magnetic field. The fluxgate sensors are mounted on an aluminium platform and are covered with a polyimide lid. The design of the MAG sensor heads is illustrated in Figure 29. Both sensor heads of MAG are designed identically.

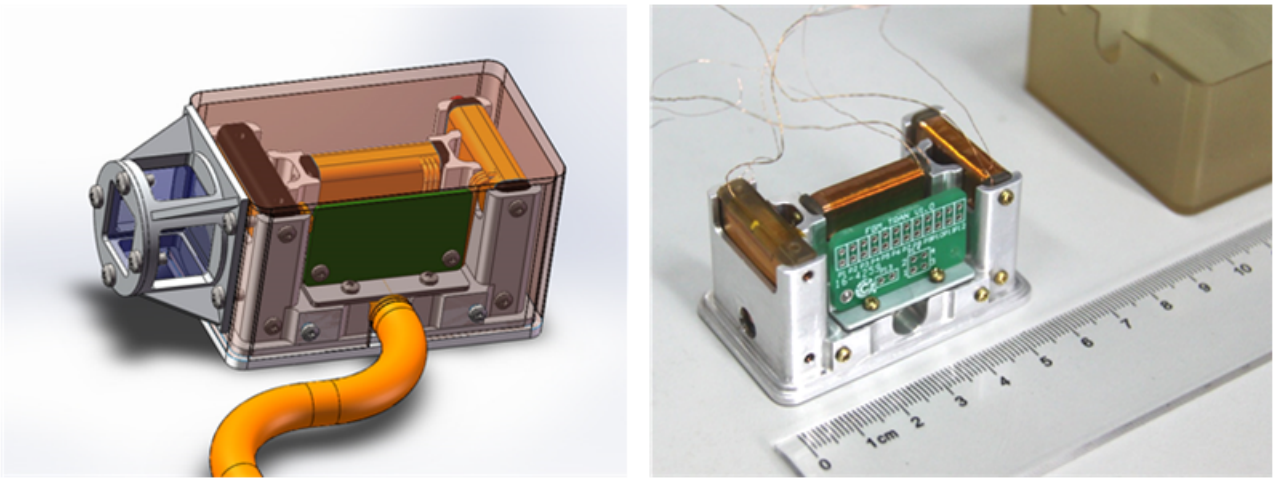

Figure 29. The MAG sensor head. Left panel: 3D rendition from CAD model. Right panel: Finished engineering model.

An optical alignment cube is mounted on one side of each sensor head enabling the alignment of the sensors with respect to the spacecraft reference frame during the S/C AIT activities. The alignment cubes will not be removed after alignment and remain mounted on the sensor heads. The sensor heads are connected by harness to the electronics box mounted on the PLM.

4.3.2.2 *Read-out chain*

The magnetometer electronics combines analogue front end circuits with digital electronics realised in a Field Programmable Gate Array (FPGA). A block diagram of the MAG electronics is shown in Figure 30.

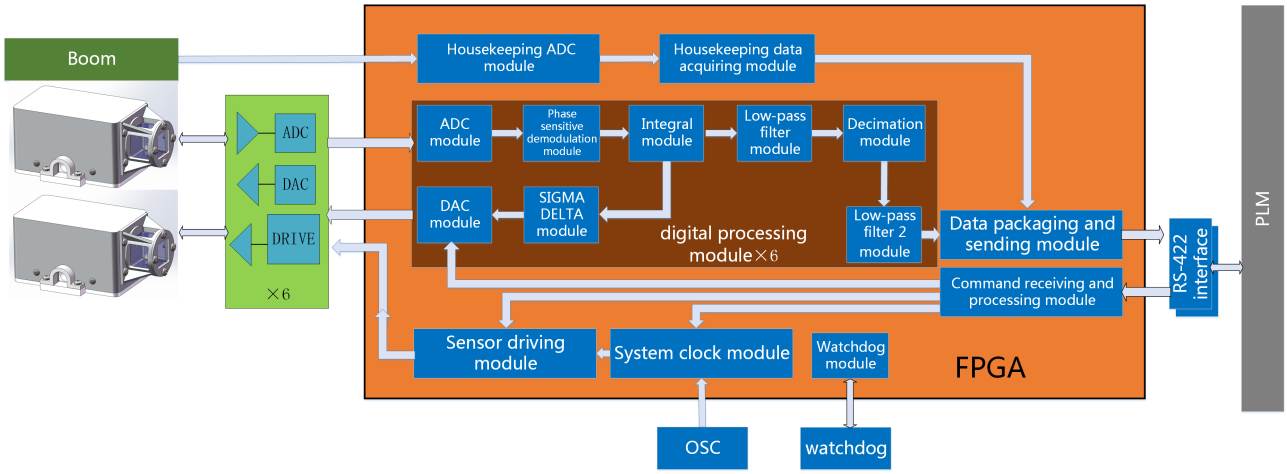

Figure 30. Functional block diagram of the MAG electronics.

The analogue front end electronics includes a dedicated pre-amplifier, low pass filter and 24bit A/D converter for each sensor coil. The analogue electronics furthermore includes the drive electronics for the sensor excitation coils as well as D/A converter and drive electronics for sensor feedback coils. The digital part of the read-out chain provides digital data processing of the individual sensor signals including phase sensitive de-modulation, low pass filtering, sigma-delta processing and signal decimation. Sensor excitation signals derived from an internal clock signal and the feedback compensation signals are also generated by the digital electronics. Additional service circuits and components in the FPGA furthermore collect housekeeping data from the MAG electronics as well as the MAG boom (end-switch status) and provide the TM/TC interface to the PLM CU.

4.3.2.3 *Electronics box*

The MAG electronics box is a four-layer aluminium chassis. Each layer consists of a mounting frame for each of the individual electronics boards, and are stacked on top of each other to form the electronics box. The first layer contains redundant DC/DC power supply modules and redundant RS-422 communication interfaces, drive circuits for both sensor heads and a clock unit. The second layer contains the FPGA based digital processing unit and housekeeping A/D converters. The third layer contains drive circuits and amplifiers, as well as A/D and D/A converters for the first sensor head. The forth layer contains the same functional units as layer three but for the second sensor head. The MAG electronics box is mounted on the PLM base plate, conductively cooled through the mounting interface.

4.3.2.4 *Deployable boom*

The MAG boom is a three-segment deployable boom, heritage of the Chinese FengYun-4 mission (Figure 31). The total length of the boom is 3028 mm in unfolded configuration. The two sensor heads are mounted on the third segment, one close to the tip of the boom and the other at a position around 2185 mm from the boom-PLM mounting flange. All segments of the MAG boom including the sensor heads will be covered with MLI. No part of the MAG boom nor the MAG sensor heads will require active thermal control.

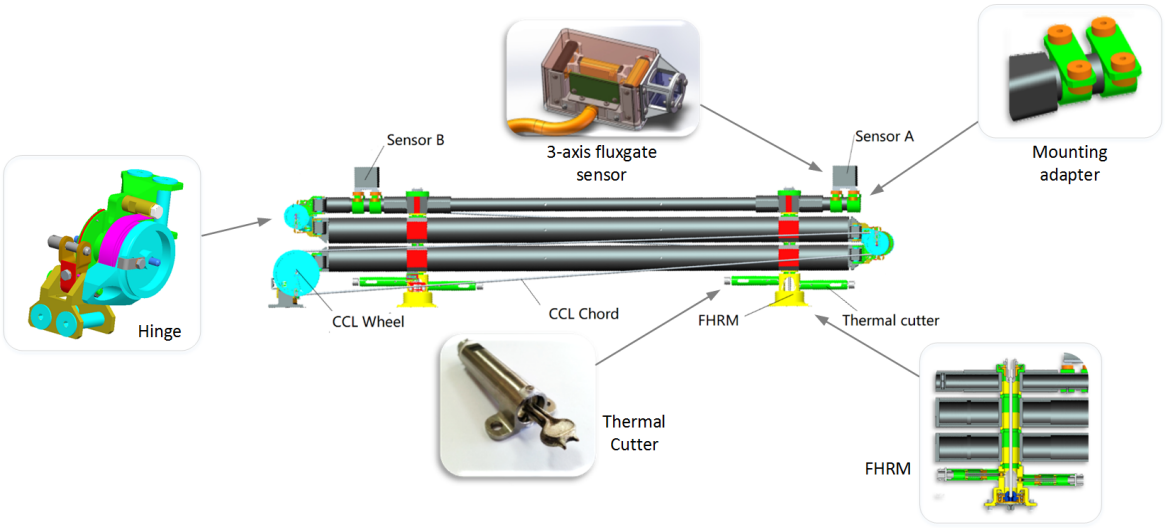

Figure 31. MAG deployable boom highlighting some of its main elements.

The MAG boom will be in folded configuration during launch. A set of two flexible hold-down and release mechanism (FHRM) will keep the boom in its folded configuration and act as launch locks. The FHRMs are non-pyrotechnical mechanism, which use a fibre rope and double redundant, electrically heated thermal cutters. To initiate boom deployment, the PF will issue a release command to the PLM CU and the PLM PDU will power the boom release cutters. After successful operation of the FHRMs, the boom will deploy driven by springs at its hinges. A set of Closed Cable Loop (CCL) mechanisms will synchronize the three boom segments during deployment and control the deployment envelope. Mechanical locks and end switches at the hinges will finally hold the boom in the deployed position and provide confirmation of the boom deployment. The MAG boom will be deployed within 40 days after launch, after deployment of the S/C solar panels.

4.3.3 MAG Interfaces and Resources

4.3.3.1 *Interfaces*

The MAG E-box is mechanically and thermally coupled to the PLM panel The MAG boom is also mounted on the PLM panel, but boom and FHRMs are thermally decoupled from the PLM. Primary power (nominal and redundant) to the E-box as well as the FHRMs is provided and controlled by the PLM Power Distribution Unit. The MAG communication system provides a set of redundant UART RS-422 serial receive and send signals for communication with the PLM CU.

4.3.3.2 *Instrument budgets*

Table 12 and Table 13 summarise the mass and power budget for the MAG instrument. The instrument will produce data throughout the SMILE science orbit at a rate of 6 kbps, resulting in a total data volume of 1.06 Git per orbit, including housekeeping data.

Unit	Design mass [kg]	Maturity margin	Nominal mass [kg]
Sensor heads	0.36	10%	0.4
E-box	1.83	20%	2.2
Boom	5.18	10%	5.7
Harness	0.36	10%	0.4
Total mass			**8.7**

Table 12. MAG mass budget (kg)

	Average power at 29V [W]	Maturity margin	Nominal power at 29V [W]	Maximum power at 34.5V [W]
During science operations	4.17	20%	5.0	6.0
Boom FHRMs	190.48	5%	200	317.4
During boom release	194.65	5.3%	205	323.4

Table 13. MAG power budget (W)

4.3.4 MAG Instrument Performance

4.3.4.1 *Error sources and measurement accuracy*

A number of error sources need to be considered when modelling the measurement accuracy of the magnetometer, including: errors caused by sensor offset drift, sensor orientation and non-orthogonality errors, system non-linearity, system thermal drift and errors caused by the stable (DC) and varying (AC) stray magnetic fields originating from the spacecraft. Some measurement errors e.g. sensor offset and thermal drift, non-orthogonality and orientation errors, can be reduced or compensated by suitable ground calibration and alignment activities. Other errors (sensor offset and DC stray magnetic field) can only be compensated by suitable in-orbit calibration e.g. solar wind/magnetosheath calibration or spacecraft rotations along at least two independent axes. The later introduces another error source caused by variations of the local plasma magnetic fields during the calibration procedure. Finally, both sensor heads can be used to compensate for AC stray magnetic fields, reducing the error by around 80%. If the magnetometer is operated in dual-sensor configuration i.e. information from both sensors is considered, both sensors also contribute to the resulting error budget, causing an increase of the aforementioned measurement errors by a factor of $\sqrt{2}$. The expected contributions from the main error sources and the total resulting measurement accuracy with a single, ground calibrated sensor, a single sensor considering in-orbit calibration and the magnetometer in dual-sensor configuration are summarised in Table 14.

Errors (in nT rms)	Thermal Drift	Non-linearity	Non-orthogonality	Orientation error	AC stray field	DC stray field	Sensor Offset	Field variation during calibration	**Resulting measurement accuracy**
Single sensor	0.25	0.05	0.09	0.87	2.5	7.5	2.0	n/a	**8.58**
In-flight calibration	0.25	0.05	0.09	0.87	2.5	0.8		2.5	**3.74**
Dual-sensor	0.35	0.07	0.35	0.87	0.5	1.13		0.5	**1.64**

Table 14. Contributions of main error sources and resulting measurement accuracy for main operating conditions.

4.3.4.2 *Resolution*

The predicted performance of the instrument will achieve the science requirements on the magnetic field measurement (Table 15). The resolution of the magnetometer critically depends on the sensor noise and stray

magnetic field from the spacecraft. The magnetometer resolution is also a function of the instrument bandwidth, with the resolution decreasing with increasing bandwidth.

	Science Requirement	Predicted Performance
Accuracy	2 nT	1.64 nT
Resolution	0.1 nT (2 min cadence)	0.099 nT (2 min cadence)
		0.17 nT (40 Hz)

Table 15. Modelled MAG performance vs. science requirements

4.4 The Light Ion Analyzer: LIA

The in-situ plasma analyzer LIA is developed by the National Space Science Center in China with contributions from the UK and France. LIA will measure the solar wind and magnetosheath ion distributions and determine its basic moments such as density, velocity, temperature tensor, and heat flux vector.

4.4.1 LIA Instrument Architecture

The LIA system consists of two identical instruments located on opposite sides of the CAS provided spacecraft Platform. Each of the instrument covers a solid angle of 2π, such that both instruments together have a 4π field-of-view. Each LIA consists of an electrostatic analyser directly mounted to a back end electronics box. The instruments only have TM/TC interfaces with the PLM; all mechanical, thermal and power interfaces are with the spacecraft Platform. The main parameters of the LIA system are summarised in Table 16:

Ion energy range	0.05 – 20 keV/q
Energy resolution ($\Delta E/E$)	≤ 10% for 3D velocity distribution function
Field of view	2π (single instrument) 4π (full LIA system)
Time resolution	min 0.5 sec
Azimuth range (each instrument)	360°
Elevation range (each instrument)	0.05 – 13.2 keV: 0 - 90° 13.2 – 20 keV: 0 - 62°
Max. angular resolution	Azimuth: 30° coarse / 7.5° fine Elevation: ≤6°

Table 16. Main parameters of the LIA system. Note that the achievable angular resolution in Azimuth direction is a function of the elevation angle. At 90° Elevation, the system resolution in Azimuth is 26.86°.

4.4.2 LIA Instrument Design

4.4.2.1 *LIA sensor*

The LIA sensor is designed as a top-hat type electrostatic analyser with scan-able field of view deflection system (FDS) added at its entrance. A schematic representation of the LIA electron-optical system is shown in the right panel of Figure 32.

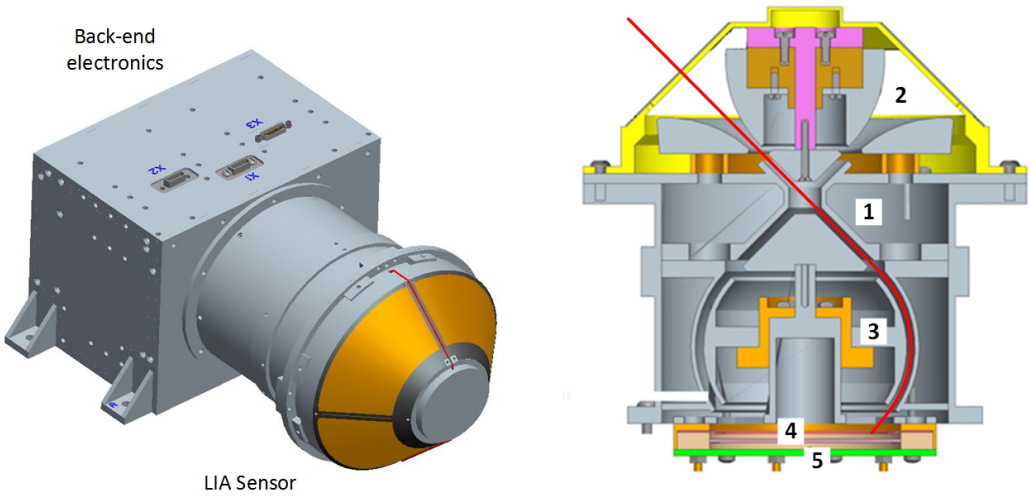

Figure 32. Left panel: 3D rendition of LIA highlighting the main sub-systems. Right panel: cut-away view of the LIA electro-optical sensor. A typical path of a detected ion is shown as a red line.

The actual energy analyser, denoted as (3) in Figure 32, consists of a pair of nested electrodes forming a part of a two concentric hemispheres, the "inner hemisphere" and the grounded "outer hemisphere". When a negative voltage is applied to the inner hemisphere, an electric field is created in the gap between the two hemispheres. Charged particles entering the analyser will be deflected in the electric field and follow the curvature of the hemispheres to hit a position sensitive detector system (4) comprising an annular microchannel plate (MCP) with a system of 48 radial anode segments. The ion-optical system thus acts as monochromatic detector which is sensitive to ions entering the analyser from a pre-determined direction and have an energy/charge ratio set by the applied voltage. The direction of arrival of the ions in the Azimuth direction is determined from the position at which the ions hit the detector. The highest achievable Azimuth angular resolution set by the number of anode segments is 7.5° and can be reduced to 30° when the signals of four adjacent anodes are added.

The analyser will have an instantaneous undeflected field of view of 360° (Azimuth) × 3° (Elevation). The full field of view covering a solid angle of 2π is realised with a "Field of View Deflector System" (FDS) (2) which allows the electrostatic deflection of incoming ions by up to ±45° relative to the undeflected field of view. In addition, the LIA design will also feature a "Variable Geometric Factor System" (VGFS), denoted as (1) in Figure 32. Application of a voltage to an inner electrode reduces the overall bandpass, allowing a variation of the instrument sensitivity in order to optimise its response to the ions of different plasma populations encountered at different locations in the orbit.

4.4.2.2 *LIA electronics box*

The LIA sensor is mounted directly onto the electronics box (see left panel of Figure 32) to form one single instrument unit. The electronics box contains four dedicated electronics boards containing: the sensor readout electronics including charge sensitive amplifiers for each anode segment, a low voltage power supply board generating the secondary instrument voltages, a HV power supply board to generate sweeping voltages for energy and elevation scans as well as the voltages for the VGFS and MCP elements,. In addition, the FPGA-based sensor control electronics and DPU board for digital data processing will interface to the spacecraft platform and PLM on-board computers. The LIA electronics block diagram, showing the LIA electrical architecture and electrical interfaces to the payload module and platform, is shown in Figure 33. Both LIA instruments have the same electronics architecture, housed in dedicated electronics boxes for each sensor.

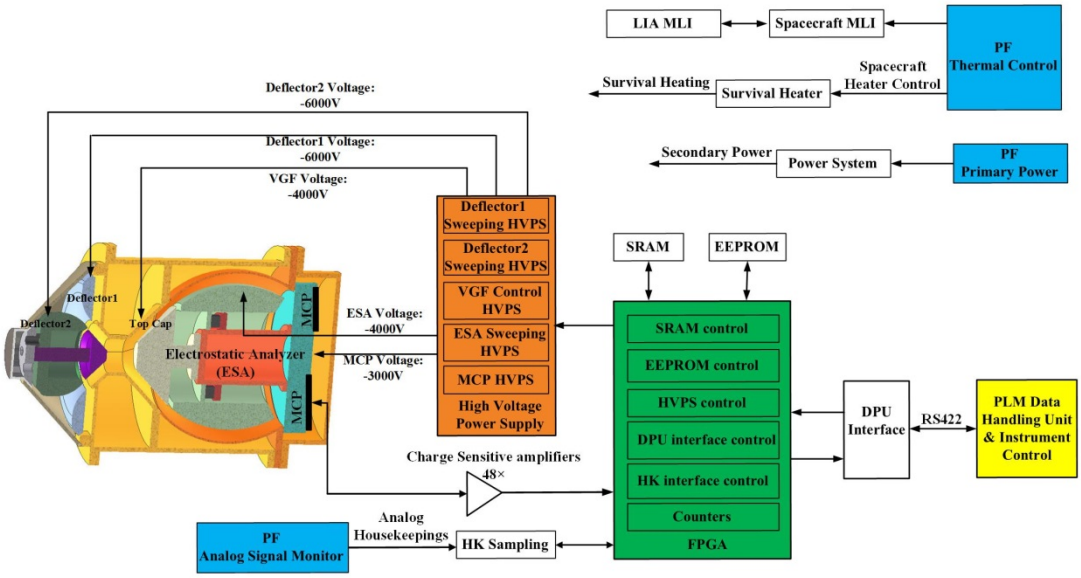

Figure 33. Electronics block diagram of LIA. Interfaces to the spacecraft platform (PF) and the PLM are highlighted.

4.4.3 LIA Interfaces and Resources

4.4.3.1 *Interfaces*

The LIA instruments are mounted on two opposite sides of the spacecraft platform. The two instruments have most interfaces, including mechanical, thermal, power and housekeeping data interfaces with the platform and only TM/TC interfaces, realised in the UART RS-422 standard, with the PLM. The individual instruments do not include any redundant elements mainly due to mass constrains. A certain level of redundancy is provided through the implementation of two individual instruments, although with reduced performance in case of one instrument failing.

4.4.3.2 *Instrument budgets*

Table 17 and Table 18 summarise the mass and power budget for the LIA instrument system. The instruments will produce data throughout the SMILE science orbit at a rate of 48 kbps, resulting in a total data volume of 8.36 Git per orbit, including housekeeping data.

Unit	Design mass [kg]	Maturity margin	Nominal mass [kg]
Charged particle optics	0.57	5%	0.6
Read-out element	0.14	20%	0.17
E-Box	2.03	10%	2.23
Sub-total, per instrument			3.0
Total mass, 2 instruments			**6.0**

Table 17. LIA mass budget.

Unit	Design power [W]	Maturity margin	Nominal power [W]
Read-out element	0.20	20%	0.24
Back end electronics	5.01	15%	5.76
Sub-total per instrument			6.0
Total power, 2 instruments			12.0

Table 18. LIA power budget.

4.4.4 LIA Instrument Performance

A trade study was carried out to investigate the general instrument requirements and in particular the performance of the system implementing two LIA instruments to cover the entire 4π field of view versus a single LIA only covering a 2π field of view. The system performance was derived through a statistical study based on data collected over 92 orbits by the Cluster mission, including almost 650000 individual 3D measurements. A comparison of the full 3D data from Cluster with the moments derived from the 2π field of view of only one LIA instrument and interpolations for the remaining 2π solid angle is shown in Figure 34. The results show that, while the ion velocity is reproduced fairly well, the measurements of the ion density as well as temperature are far outside the required accuracy of 20% as defined by the SMILE science requirements. A system with two LIA instruments located on either side of the SMILE spacecraft has therefore been selected.

The two LIA instruments are designed to operate simultaneously and synchronously throughout the entire science orbit. The LIA system has 2 different scientific operating modes: Normal Mode (NM) and Burst Mode (BM). Normal Mode will primarily be used to provide full 3-D moments of the plasma ions at a cadence of 2 second. In this mode, the sensor will scan 62 energy values for 8 Elevation angles, acquiring 24 Azimuth angles simultaneously with each sample. The instruments will be in this mode for most of the science orbit. Burst Mode is providing a mode to increase the time resolution from 2 seconds (NM) to 0.5 second but at the same time decrease the number of energy steps from 62 to 30 and reduce the number of Elevation steps and the Azimuth resolution. Burst Mode will primarily be used near apogee.

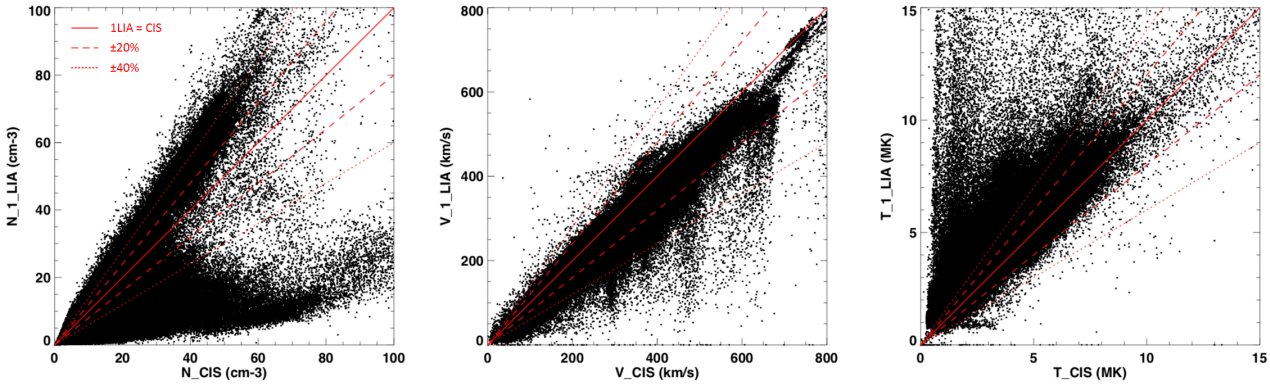

Figure 34. Results of a trade study comparing the ion moments measured with Cluster (horizontal axis) with the ones derived from the data obtained by a single LIA instrument covering a 2π field of view (vertical axis). Panels from left to right show results for ion density, velocity and temperature.

The performance of the LIA instruments is ultimately limited by the system measurement errors which include systematic errors resulting from specific instrument properties like limited measurement range and resolution as well as statistical errors i.e. noise due to statistical processes within the detection chain. The instrument measurement errors have been quantified through simulations of the instrument performance based on the propagation of simulated populations of ions with a drifting Maxwellian distributions for density, velocity and temperature through the instrument. A typical result of the measurement error simulations for ion density, velocity and temperature is shown in Figure 35. The simulations in general verify the performance of the LIA instrument near apogee and the overall compliance to the science requirements.

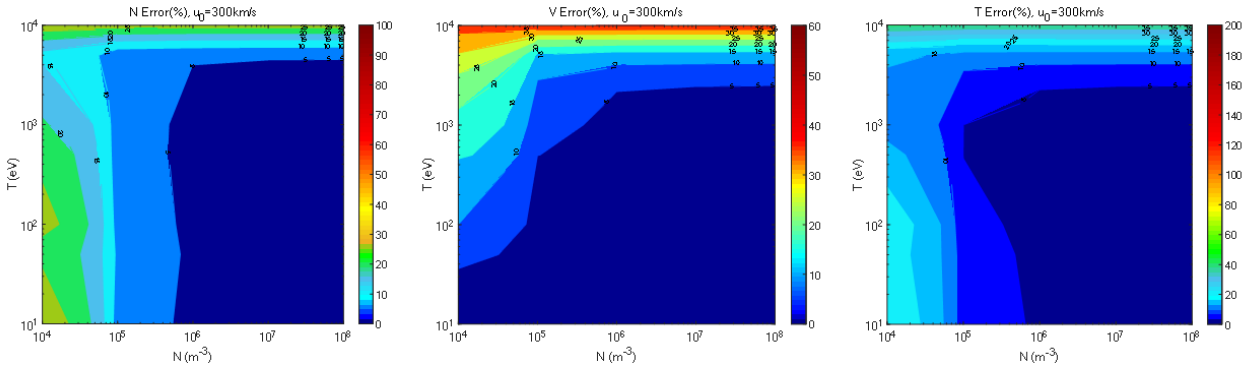

Figure 35. Simulation results showing the measurements errors (in percent) for ion density (left panel), velocity (centre panel) and temperature (right panel) as a function of ion density and temperature for ion velocity of 300 km/s.

5 Mission design

5.1 Mission description

The mission consists of a single spacecraft which will be launched from the Centre Spatial Guyanais, Kourou. It is compatible with a launch on VEGA-C (option 1 – single launch) and Ariane 6 (option 2 – dual launch). VEGA's capability is not sufficient for SMILE. Both launch vehicles are at critical design review (CDR) stage with a maiden flight for VEGA-C planned end 2019, therefore long before the PLM and Mission CDR foreseen respectively in December 2020 and September 2021. At that point, the VEGA-C performances will be fully confirmed as well as the spacecraft mass budgets following STM tests. The intention is to down-select the baseline launch vehicle by Mission CDR.

In option 1, it will be launched into a 70° inclined LEO orbit, typically 700 km circular. In option 2, it will be launched into an SSO orbit, 700 km circular, to increase the likelihood to find a primary passenger (Earth observation). In that scenario, waiting in LEO is necessary in order to reach the Right Ascension of the Ascending Node range, which could be up to 6 months. In order to minimise orbital variations due to third body perturbations, comply with a re-entry within 25 years and maximise science return, a RAAN of 206º is selected for option 1 and between 345 – 15° or 165 – 195° in option 2. The argument of perigee ~ 288° is such as to allow communications to the baseline ground station in Antarctica. This orbit ensures a long observation time around apogee for observing the regions of interest with a relatively low perigee for downloading the scientific data without diving too deep into Earth's radiation belts.

After launcher separation in LEO, the spacecraft will then transfer to the final HEO science orbit using chemical propulsion. Eighteen burns of the main engine will be performed to increase the perigee and apogee altitudes requiring a delta-V of 2.97 km s^{-1} (Figure 36). Upon arrival in HEO and following a commissioning period of 2 months, the spacecraft starts science operations on its 51-hour orbit. The nominal science operations along the orbit can be broken down into 5 mission-level modes depicted as below and supplemented by basic idle, stand-by and safe modes:

- Full Science Mode: All 4 instruments are able to operate. Spacecraft attitude driven by SXI LoS pointing to the magnetopause.
- Reduced Science Mode 1: UVI is not allowed to operate due to Sun exclusion constraints.
- Reduced Science Mode 2: SXI is not allowed to operate due to Sun exclusion constraints or because altitude is lower than 50000 km. At that altitude a shutter closes in front of the focal plane to limit radiation doses on the SXI CCD detector.
- Reduced Science Mode 3: Only MAG and LIA operate and the spacecraft attitude is power-optimised.
- X-band Communication Mode: PLM transmits in X-band all science and telemetry data collected along one orbit to either Troll (baseline, ESA GS) or Sanya (support, CAS GS).

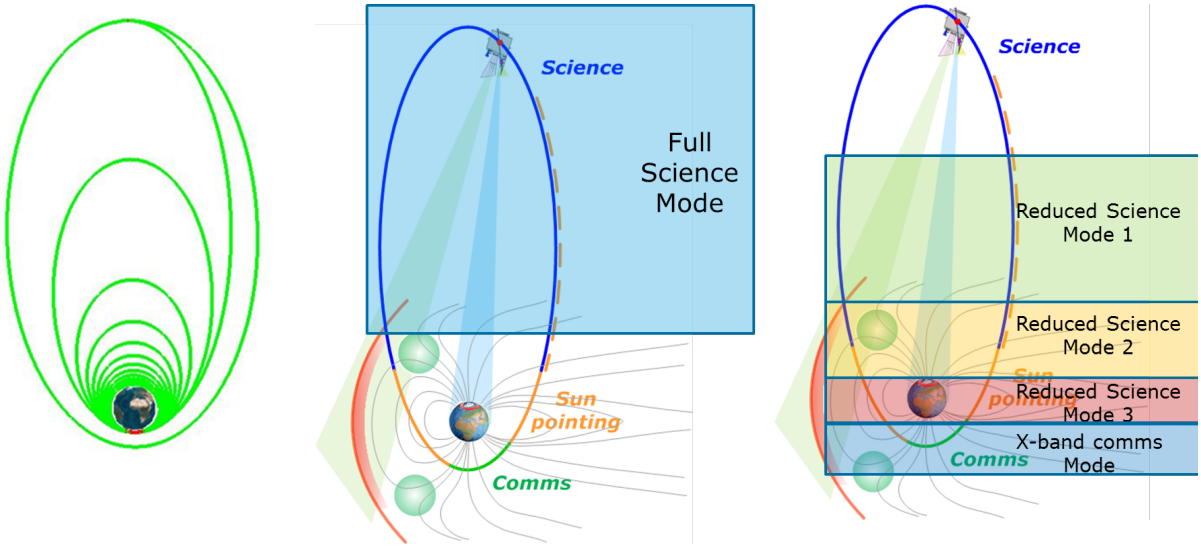

Figure 36. SMILE transfer strategy (left) and SMILE main science operating modes (centre and right)

While the mission concept is innovative by providing simultaneously imaging of the magnetosheath, polar cusps and aurora, using both X-ray and UV, and in-situ solar wind measurements, the spacecraft (including the scientific instruments) makes use of state-of-the-art technologies. The mission has no major launch window constraints, but in order to stay within its programmatic boundaries, a development phase of ~ 5 years is foreseen with a nominal launch date in November 2023. Platform and PLM units shall be at TRL 7 by their respective PDR while instruments units shall be at TRL 6 by instruments PDR. The above essentially requires the use of qualified units or involving very limited development. This poses strong constraints on the CAS-ESA interfaces definition on both sides and the innovative nature of the collaboration scheme, involving different engineering standards and technologies, implies very close and iterative interface engineering. Given its programmatic context, reliability requirements are not specifically defined for this mission but best ECSS PA practices have been specified jointly wherever possible, e.g. avoidance of single point failure.

5.2 Spacecraft description

The SMILE spacecraft as foreseen during the CAS/ESA joint Phase 0 Study is shown in Figure 37

Figure 37. SMILE spacecraft 3D model during the phase 0 study.

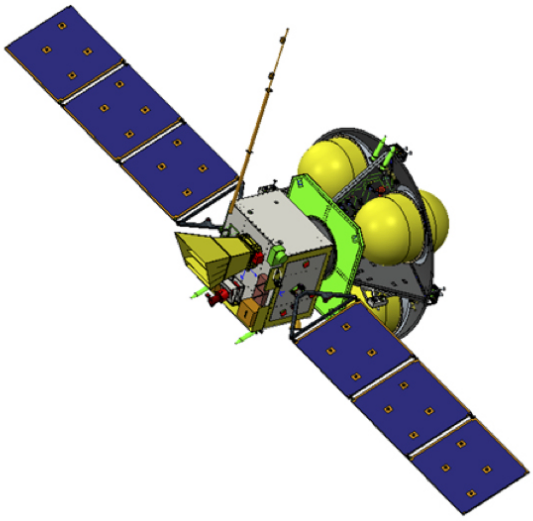

5.2.1 Spacecraft Design Drivers

The SMILE spacecraft is designed to meet the mission science and lifetime requirements. Beyond this primary driver the design of the spacecraft is driven by the division of the ESA and CAS responsibilities. This separation has resulted in a logical separation between the Platform (PF) and the PayLoad Module (PLM). This is a separation with respect to responsibilities and design authority. The propellant mass required to reach and maintain the science orbit represents two thirds of the spacecraft launch mass, and this, coupled with the mass limitations of the VEGA-C launch performance, constitutes a strong design driver which affects decisions made in all subsystems.

In order to meet the stringent schedule and programmatic constraints, the use of existing hardware based on a flight qualified designs and a minimum of mission specific changes have been prioritised. This requirement for existing hardware results in specific design constraints based upon heritage.

Specific instrument and hardware constraints are considered primary drivers for the mission as a whole. For example, the radiation environment for this mission is relatively severe and the science orbit has been selected to avoid the spacecraft passing through the lower Van Allen belt (trapped protons) as they degrade the performance of the CCDs of the Soft X-ray Imager (SXI). The shielding requirements for the electronic units and instruments are more substantial than a typical LEO platform. The thermal environment required for the science operations of the SXI instrument is another key driver considered in the design of the mission.

5.2.2 SMILE Spacecraft at System Level

The spacecraft is combining the CAS led PF and the ESA led PLM. They are designed and developed separately, tested independently, and then integrated, and tested at system level. The PF and PLM are connected through electrical and data interfaces, which are coordinated at ESA/CAS level through interface requirements and interface control documents. The PLM maintains its own PLM timeline and mass memory, and is responsible for downlinking the data to the ground. The electrical and data flow architecture is summarised in Figure 38.

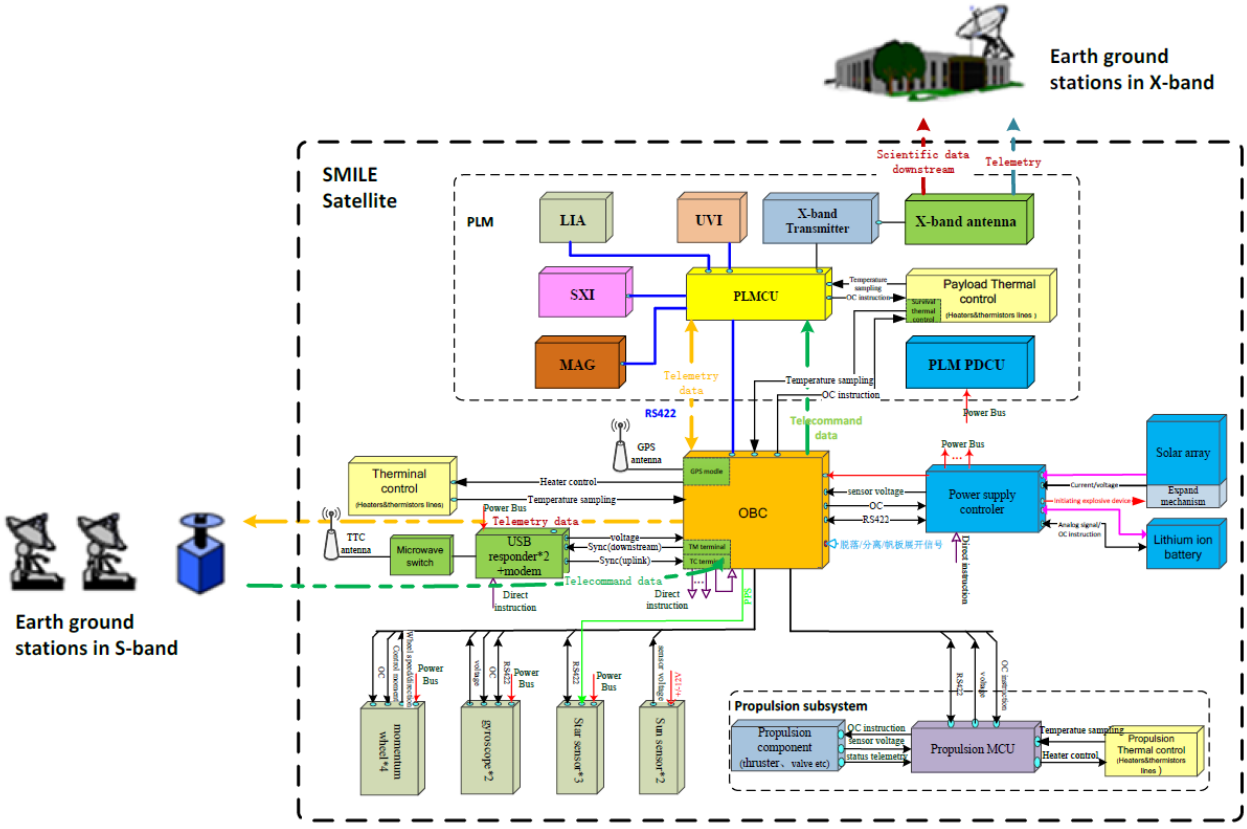

Figure 38. SMILE spacecraft electrical and data flow schematic

The spacecraft is responsible for maintaining the attitude control required for the various Science and communication modes. The Operational modes and transitions are summarised in Figure 39.

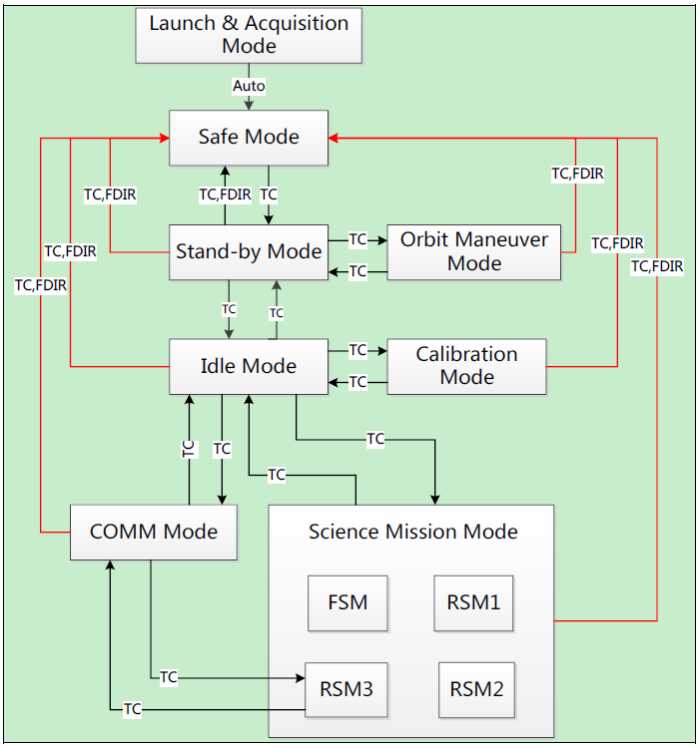

Figure 39. Smile spacecraft modes of operation.

5.2.2.1 *Mass Budget*

The launch mass constrained by the performance of the VEGA-C launch vehicle is 2200kg. The current design including system margin is shown on Table 19. The total PLM mass is 132kg and includes SXI, UVI, and MAG instruments. The total spacecraft dry mass is 679 kg which is less than half of the propelant mass of 1521 kg.

Module	**Subsystem**	**Mass at Launch [kg]**		
		Mass Allocation	System Margin	Total Mass
Platform	Electrical Power System	37.7	26.1kg (5%)	547 kg
	Harness	20.0		
	On-Board Data Handling	12.0		
	Telemetry, Tracking, and Command	13.0		
	Attitude Orbit Control System	56.2		
	Propulsion	145.0		
	Structure	200.0		
	Thermal	31.0		
	LIA Instrument	6.0		
PLM	PLM Hardware	47.5	25.3 kg (23%)	132 kg
	SXI	36.0		
	UVI	14.5		
	MAG	8.7		
Spacecraft	*Total Dry Mass*			*679 kg*
Wet Load	Propellant	1365	151 kg (11%)	1516 kg
	Pressurant	4.2	0.8 kg (20%)	5 kg
Spacecraft	**Launch Mass**			**2200 kg**

Table 19. The Spacecraft mass budget.

5.2.2.2 *Power Budget*

The SMILE power budget is shown in Table 20 for the main spacecraft modes. The total payload power needed in science mode is 94 W. The minimum power required is 447 W in survival mode and the maximum power of 665W is required during the communications and transfer of data to the receiving ground station.

Module	**Subsystem**	**Mode [W]**			
		PLM OFF	Survival	Full Science	Communications
Platform	Electrical Power System	15	15	15	15
	On-Board Data Handling	15	15	15	15
	Telemetry, Tracking, and Command	45	35	45	45
	Attitude Orbit Control System	117.5	117.5	117.5	160
	Propulsion	20	20	20	20
	Thermal	100	100	100	100
	LIA Instrument	0	0	12	12
	Margin	62.5	60.5	65	73.4
PLM	PLM Hardware (+ Margin)	84	60	72.4	165.7
	SXI	0	0	44.6	21.3
	UVI	0	0	32.0	32.0
	MAG	0	0	6	6
Spacecraft	**Total**	**459**	**447**	**544.4**	**665.4**

Table 20. Spacecraft power budget.

5.2.2.3 *Pointing Budget*

In order to satisfy the pointing requirements and knowledge requirements for the instruments, a breakdown between PF and PLM has been done. Table 21 shows such breakdown for the various instruments. The requirements (R) are needed to meet the science objectives of the mission, while the goals (G) reflect enhanced performance benefiting the instrument science return.

	Inst.	**Absolute Pointing Error**			**Absolute Knowledge Error**			**Relative Pointing Error**			
		Total	PF	PLM	Total	PF	PLM	Total	Time Basis	PF	PLM
Across Line of Sight (X)	SXI	0.5	0.3	0.2	0.5	0.15	0.35	0.15	2 sec	0.05	0.1
	UVI	0.5	0.3	0.2	R: 0.25 G: 0.024	0.15	0.1	R: 0.07 G: 0.024	1 min	0.05	0.02
	MAG	-	-	-	0.5	0.15	0.35	R: 0.5 G: 0.06	1 min	0.03	0.47
Around Line of Sight (Y&Z)	SXI	1.9	1	0.9	1.9	1	0.9	0.6	2 sec	0.5	0.1
	UVI	N/A	N/A	N/A	0.75	0.25	0.5	0.33	1 min	0.23	0.1
	MAG	-	-	-	0.5	0.15	0.35	R: 0.5 G: 0.06	1 min	0.03	0.47

Table 21. The pointing allocations considered (in degrees)

5.2.3 The Platform

The spacecraft platform (PF), under CAS responsibility, is functionally and physically separated between a service module and a propulsion module (illustrated in Figure 40). The service module design has heritage from previous CAS missions such as Beidu, Hard X-ray Modulation Telescope, Quantum Experiments at Space Scale, and Dark Matter Particle Explorer. The propulsion module is based on a previous structure but scaled to the needs of SMILE, the main engine being derived from Chang'E 2 heritage. The Payload module is the top panel of the Service Module and is under ESA responsibility (addressed in detail below in Section 5.2.4).

The propulsion module will be mainly used to raise SMILE from the initial LEO orbit to the final science orbit. The propulsion module hosts the LIA instruments. The service module provides the power, S-band link with the ground, and the central command and control of the spacecraft including to the PLM.

Figure 40. The SMILE platform (PF) in launch configuration.

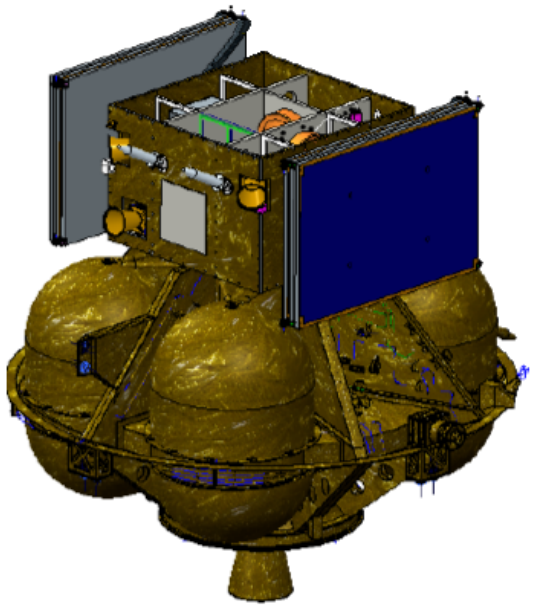

The main platform drivers are the spacecraft total launch mass, radiation, AOCS pointing, and power provisions. The platform has been optimised with respect to mass in order to meet the launch mass requirements for VEGA-C. The SMILE radiation environment has been considered for the selection of all platform hardware. The AOCS system is designed to ensure the spacecraft pointing and knowledge requirements. The solar arrays and battery have been sized for the mission requirements and the eclipse conditions.

The platform TRL is stated to be level 8 or 9 for all elements except the S-band transponder which is modified from the QUESS mission and the solar arrays which are to be modified for the low shock environment needed for the instrument performances.

The primary technical parameters of the platform subsystems are listed in Table 22.

Platform mass	547 kg with 5% System Margin 1521 kg propellant (Wet load)
Platform Dimensions	Φ 2762 mm x 2537 mm
Power Bus	24-34V ±0.5V Unregulated
Solar Array Power	5.8m^2 – 850W

Battery Size	60Ah Li-Battery
S-band	22Mb/day 2,4,8, and 16 kbps rates
AOCS Hardware	4 Reaction Wheels 3 Star trackers 2 fibre gyroscopes Sun sensors GPS receiver
Propulsion System	Bi-propellant Hydrazine system 490N Main Engine 315s ISP 2x6 – 10N Thrusters 1600kg maximum tank capacity

Table 22. The Platform technical performance figures.

5.2.4 The Payload Module (PLM)

The Payload Module (PLM) is one of ESA's responsibilities within the SMILE project and will be contracted to one of the three industrial consortia involved in SMILE study: EADS (Spain), Thales (UK), or Qinetiq (Belgium). The PLM is acting as the top panel of the service module in order to save mass (see Figure 40). The equipment on the PLM is accommodated only on the top side of the panel and the panel is thermally isolated both radiatively and conductively to facilitate the independent verification. The top panel architecture was chosen at the end of the Phase 0 study, primarily as a mass saving option.

Most PLM sub-systems are at TRL 9. Some additional development may be needed at the level of electronic boards but all components are qualified.

The primary PLM functions required are to host three instruments (SXI, UVI, and MAG) and to provide telecommand and telemetry connections to the LIA instruments hosted on the Platform. The PLM is required to provide:

- Command and control functions for the PLM units and the hosted instruments,
- Interface with the Platform for commanding, FDIR, PF telemetry, and power,
- Storage of science data from the instruments and telemetry from the Platform which is downlinked by the X-band,
- power distribution to all PLM units on the PLM,
- high data rate (~40Gb/orbit) X-band transmission to the ground,
- design and implementation of the PLM thermal control and mechanical.

The main PLM technical drivers are to:

- Minimise mass,
- Utilise as much heritage as possible (high TRL),
- Provide a suitable thermal environment for SXI,
- Provide mechanical environment for the instruments,
- Design for the radiation environment,
- Provide the magnetic environment required for MAG,
- Provide a suitably clean environment for the SXI and UVI.

As a result of the mission requirements the three PLM designs are very similar; however, each company's particular heritage and unit availability differentiate the various designs from each other.

The SXI accommodation location is constrained to being on the anti-sun edge of the PLM to provide the maximum efficiency of the SXI dedicated radiator. In order to avoid straylight concerns UVI is accommodated on the same edge of the PLM baseplate. The three possible contractors have their own solutions with respect to units and thermal designs, both with and without heat-pipes. The primary technical parameters of the PLM subsystems are given in Table 23.

PLM mass	132 kg including instruments 57 kg excluding instruments
PLM Power Allocation	155W Nominal 225W Communication
X-band	Earth Observation X-band 35.5Gb Science data 2.5+ Gbit Housekeeping
Mass Memory	Required to store 2 orbits data
Interfaces	Spacewire (SXI option) RS-422 (all other data links)

Table 23. The payload module (PLM) technical performances

5.3 Integration and testing

Each Party will develop the elements under their responsibility independently and will deliver them qualified to the receiving party. Interfaces will be managed as described in chapter 7.1. The PLM follows a PFM approach, justified by the need to build on heritage and/or qualified units, whereas the PF follows a QM/FM approach. Eventually the flight models of the PF (CAS), including LIA, and the PLM (ESA), including MAG, SXI and UVI, will be delivered to ESTEC (The Netherlands) for final spacecraft integration and system-level tests and verifications. This campaign will last about 10 months. Finally the spacecraft will be shipped to Kourou for a 2-month launch campaign. The entire development process up to end of spacecraft AIT follows the logic depicted in a simplified manner on Figure 41.

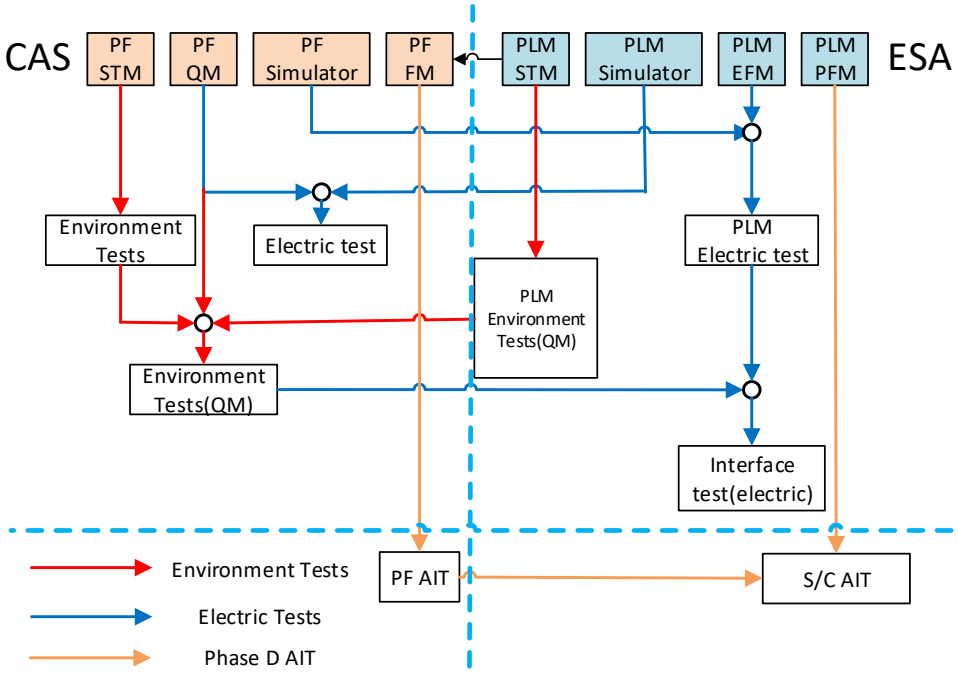

Figure 41. SMILE development process high-level logic

6 Ground Segment

6.1 Ground Segment Architecture

The ground segment and operations consist of the following split across CAS and ESA responsibility:

CAS Ground Segment

- Ground Support System (GSS) is composed of the Mission Centre (MC), the Chinese Space Science Data Centre (CSSDC), and the CAS X-band ground stations.
- Chinese Control Centre (CCC) and the S-band ground stations (prime) belong to CLTC (China Satellite Launch and TT&C General).
- Science Application System (SAS) is composed of the Strategic Planning and Operation Support Subsystem (SPOSS), Chinese Science Operation Subsystem (CSOS), and Chinese Science Data Processing Subsystem (CSDPS).

ESA Ground Segment

- ESAC includes the Science Operations Centre SOC and ESDC.
- ESOC including ESTRACK connecting to the ESA S-band ground stations and X-band ground stations.

The architecture of the SMILE ground segment is shown in Figure 42.

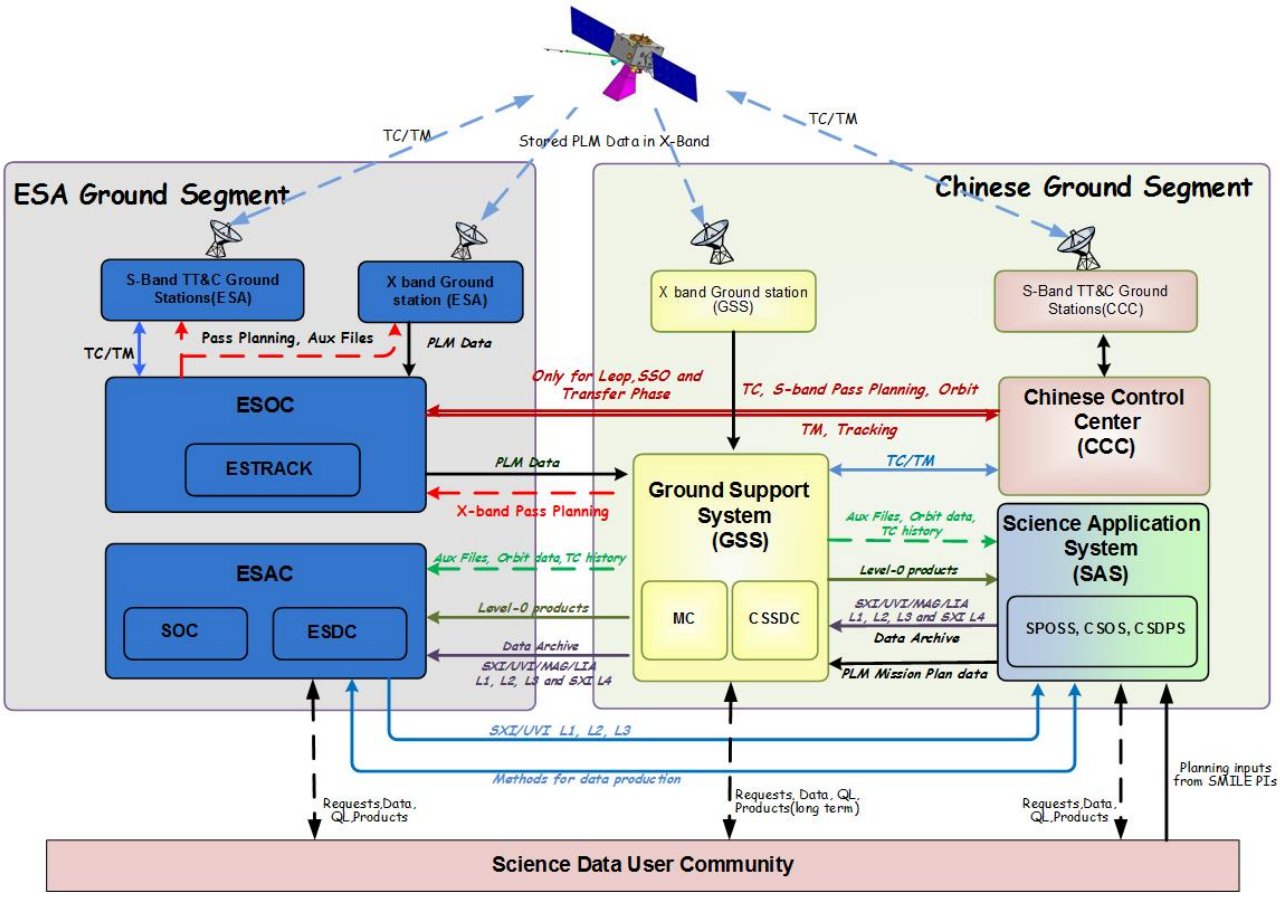

Figure 42. SMILE Ground Segment Architecture

6.2 Ground Segment Functional Areas and Operational Responsibilities

6.2.1 CAS Ground Segment

6.2.1.1 *Ground Support System (GSS)*

6.2.1.1.1 Mission Centre (MC)

MC will produce the mission planning and scheduling, payload and PLM operations and their prior coordination, payload and PLM TC compilation and generation, payload health and status monitoring, trend analysis, payload data management, and payload maintenance engineering.

The Mission Centre is under CAS responsibility and located in NSSC/CAS/Beijing.

6.2.1.1.2 Chinese Space Science Data Centre (CSSDC)

The CSSDC will be producing Level-0 products and auxiliary data products. Auxiliary data products are used in data processing and analysis and include satellite attitude, satellite orbit data, satellite ephemeris data, satellite-ground time difference, etc. The Level-0 and auxiliary data products will be immediately distributed to ESAC, SAS, Satellite and PI teams.

CSSDC is the CAS permanent archive site holding all data products from all four instruments as well as any higher-level products combining data from several or all instruments. CSSDC will transfer the archived files to ESAC to maintain synchronized file content at both sites. CSSDC provides the interface to the science data user community, providing access to all its data products.

6.2.1.1.3 CAS X-band ground stations

Sanya receiving station provides X-band downlink data reception, recording and data formatting capability. Downlinked data is transferred from the Sanya ground station to the GSS for further processing.

6.2.1.2 *Science Application System (SAS)*

6.2.1.2.1 Strategic Planning and Operation Support Subsystem (SPOSS)

The SPOSS will generate L4 data products as well as distribute data to the public during the mission cycle. SPOSS supports public outreach and education programs.

6.2.1.2.2 Chinese Science Operation Subsystem (CSOS)

The CSOS consolidates the science observations plan from all four instrument PIs and provides the consolidated mission planning inputs to the MC. Science exploration plans are made under direction of the science working team.

The CSOS monitors the status and performance of the instruments through the data services provided by MC. The science data quality is monitored by examining the quicklook (QL)/level 1 (L1) data. In case of malfunction of the instrument, CSOS will use the Payload User Manual to handle the operational response to the malfunction. Commanding response to any payload anomaly will be uplinked form the CCC. CSOS will contact PIs as necessary.

6.2.1.2.3 Chinese Science Data Processing Subsystem (CSDPS)

The CSDPS receives L0 and auxiliary data products from CSSDC and monitors data acquisition status.

The L1 to L3 data processing methods/software (custom software and common software) of LIA and MAG are provided by CSDPS and sent to ESAC before the end of Commissioning Phase. The L1 to L3 data processing methods/software (custom software and common software) of the UVI and SXI instruments are

provided by ESAC and sent to CSDPS before the end of the Commissioning Phase. CSDPS and ESAC then both have the same processing methods/software (custom software and common software) for all four instruments.

CSDPS produces the QL pipelines and L1 data for all four instruments. CSDPS produces the scientific products (L2, L3) for LIA and MAG. CSDPS checks the data products (L2, L3) of UVI and SXI received from ESAC. L4 products are both received and produced by CSDPS. All these products are sent to CSSDC for long-term archiving and distribution.

6.2.1.3 *Chinese Control Centre (CCC)*

CCC will perform the SMILE satellite operational control, telemetry monitoring, and orbit tracking of both PLM and PF. This includes both satellite tracking and orbit determination, the accuracy of which is designed to meet the mission requirement. CCC receives and processes the satellite housekeeping telemetry data and uses this to monitor satellite status and health. On-board time correlation is maintained by the CCC by measuring the time difference between S/C and ground. CCC implements the satellite monitoring and control according to the SMILE operational procedures for both PLM and PF. Specific planning and mission task inputs are received from GSS defining the payload operations plans, attitude pointing requests and PLM data dump planning. In the event of satellite emergency/anomalies CCC provides the operational response and control of the satellite. Recovery activities are coordinated between CCC, GSS, SAS, ESAC ad PI teams.

CCC provides the interface and access to the CAS provided S-Band ground stations used for TT&C.

6.2.2 ESA Ground Segment

6.2.2.1 *European Space Operations Centre (ESOC)*

ESOC's participation in the SMILE mission is the provision of the ESA X-band and S-band ground station contribution via the ESOC ESTRACK facility.

ESOC will support preparation and conduct of the RF Compatibility tests using the S-Band and X-Band RF suitcase models at the ESA reference station (no need to execute at physical ground stations sites). RFCTs are envisaged to test all up and downlinks to establish both functional and performance characteristics. These tests include verification of all telemetry, telecommand and ranging functions (as applicable) as well as spectral analysis and link budget verification.

ESOC supports routing of the downlinked X-band Telemetry data from the ESA provided X-band ground stations to GSS point of presence.

ESOC supports routing of the downlinked S-Band Telemetry data from the S-Band ground stations (Kourou, Troll, and other S-Band ground station) to CCC point of presence, as well as routing of the uplinked S-Band Telecommand data from CCC point of presence to the S-Band ground stations (Kourou, Troll, and other S-Band ground station). Ancillary data (e.g. tracking data) is provided to CCC. The provision of ESA S-Band station support is currently foreseen during LEOP, transfer to HEO phases and ad-hoc support for satellite emergencies.

The ESTRACK facility provides 24/7 support availability for X-band data acquisition during the nominal operational phase and for S-Band TT&C during LEOP and manoeuvre phase.

ESTRACK will receive the S-Band station pass planning requests for LEOP and transfer to HEO phases as well as ad-hoc emergency requests for S-Band support from CCC (S-Band station planning). ESTRACK will receive the PLM Data reception program from GSS defining the X-Band ground station pass requirements (X-band pass planning).

ESTRACK will receive orbit data from GSS for ESA generation of the Spacecraft Trajectory Data Messages (STDM) to be passed to the ESA's S and X-band ground stations for the antenna pointing control.

ESTRACK will coordinate the S and X-Band scheduling requests into an overall X-band and S-Band station schedule. ESTRACK provides remote monitoring and control of the Kourou ground station from the ESTRACK Control Centre (ECC) as well as remote monitoring of the Troll ground station.

6.2.2.2 *European Space Astronomy Centre (ESAC)*

6.2.2.2.1 Science Operation Centre (SOC)

The SOC receives L0 products and auxiliary data products from CSSDC and monitors data acquisition status.

A L0 data server is provided for the SXI and UVI instruments. Support is provided to the instrument teams in the definition, construction and operations of the data processing software.

The L1 to L3 data processing methods/software (custom software and common software) of LIA and MAG are provided by CSDPS and sent to ESAC before the end of Commissioning Phase. The L1 to L3 data processing methods/software (custom software and common software) of the UVI and SXI instruments are provided by ESAC and sent to CSDPS before the end of the Commissioning Phase. CSDPS and ESAC then both have the same processing methods/software (custom software and common software) for all four instruments.

ESAC develops and operates the QL pipelines and L1 data software of all four instruments. ESAC receives, validates and ingests the scientific data products of the UVI and SXI instruments from the instrument teams, and transfers them to SAS

Support is provided to the project scientists in public outreach and education.

6.2.2.2.2 ESAC Science Data Centre (ESDC)

ESAC receives, validates and ingests the archived data of the LIA and MAG instruments as well as auxiliary data from CSSDC. It also receives and sends the status of archived data from/to CSSDC to keep the data synchronized at both sites and provides a permanent data service to the user community.

6.3 Overview of Operational Processes

The SMILE ground segment operational processes have been split into the following areas:

Downlink: Description of all processes and activities dedicated to downlink data [Telemetry] i.e. dump of stored platform and payload telemetry data, and real time housekeeping telemetry data. Downlink processes include the whole processes of data processing and management activities such as satellite downlink data reception, data transferring, data processing, data management, data archiving and data distribution. All of the GS parties (SAS, GSS, ESAC, ESOC, and CCC) are involved in the downlink processes.

Uplink: Description of all processes and activities dedicated to uplink activities [Telecommanding]. Uplink processes include science observation plan generation, payload operation plan generation, mission scheduling, payload and PLM TC compilation and generation, and TC uplink. The SAS, GSS together with CCC implement the whole uplink process, to realize the satellite and payload operation and control.

Archive: Description of all processes and activities dedicated to archiving activities, both in CAS and ESA ground segments.

Support: Description of all processes involved in the whole system except for downlink and uplink.

6.3.1 Downlink processes.

Downlink processes transfer the real time housekeeping data and PLM stored data to ground. S-band is used for the real time housekeeping TM data transfer while X-band is using for the dumping of the PLM stored data which includes both PF and PLM HKTM as well as all the PLM Science data. SMILE mission uses Sanya, Kourou and Troll ground stations to download X-band data (see Figure 45 in Annex 1).

6.3.1.1 *X-band Downlink*

The X-band downlink data includes the dump of the stored PF and PLM HKTM as well as all the PLM Science data. For the PLM science data, the process is as follows:

1. Each orbit during the perigee passage either an ESA X-band station or a CAS X-band station receives the PLM data dump, then via the VPN link, this data is transferred to the GSS for data processing and management.
2. On arrival at the GSS, it will automatically trigger the processing line to generate L0 products, Engineering QL, and auxiliary data products.
3. GSS distributes the L0 products and auxiliary products to ESAC, SAS and PI teams immediately for high level product generation.
4. ESAC, SAS and PI teams produce L1, QL, L2, L3 and L4 products, and transfer them back to GSS for archiving.
5. SAS and ESAC will publish these data to the science community. GSS will provide long-term data publish service to the science users. Science data is available to all registered users from the moment it is available in the archives.

For the stored PF and PLM HKTM received from X-band stations, GSS will process the data and then send the data of PF, PLM and payload to SAS, payload teams and Satellite System teams (CCC).

6.3.1.2 *S-band Downlink*

S-band ground stations are the ground elements which support the telemetry downlink of the HK telemetry generated on board SMILE released for immediate transmission to ground.

1. HK data received by ESA S-band stations and CAS S-band stations will be transferred to GSS through CCC. ESA S-Band stations are foreseen to support SMILE only during Launch, LEOP, transfer to HEO and for ad-hoc support in the event of emergencies.
2. Using the HKTM, GSS and CCC monitors the health status of platform, PLM and payloads.
3. GSS will provide the status to the SAS and payload teams for PLM and payload health analysis and diagnosis.

6.3.2 Uplink process

CCC uses the S-band ground stations for telecommand uplink to SMILE. The whole uplink process is shown in Annex 1, Figure 46.

The planning concept for SMILE is split into different levels of planning with increased levels of granularity. Initially a top-level plan is devised for the science life cycle of SMILE including science objectives, detection projects, and cooperation with other space-based and ground-based programs. This top-level Science Exploration Plan is the guidance document to create all lower levels of plans. Lower level plans are then created from which the eventual Telecommand schedules are generated i.e.; long-term plan: planning cycle of one year, middle-term plan: planning cycle of three months, short-term plan: planning cycle of one week, payload plan: schedule of operating mode in one week.

1. SAS consolidates the science observations plans from all four instrument PIs. These inputs are merged and planned by SAS under the direction of the science working team, taking into consideration orbital constraints and payload status into a science observation plan. This science observation plan is then finalised by SAS and sent to GSS.
2. After receiving science observation plans, GSS carries out comprehensive task arrangements, making payload operation planning and PLM data receiving plan. The data receiving plan is sent to the appropriate Sanya, Troll and Kourou X-band Ground Stations to allow for scheduling of the specific ground station pass times.
3. According to the payload operation plan, GSS generates payloads control instructions and sends them to CAS Control Centre (CCC)
4. CCC combines the payload operations plan together with the platform control instructions and transfer those Telecommands to the available S-band ground stations for subsequent uplink to SMILE.

Emergency command uplink to the spacecraft is evoked in Annex 1.

6.3.3 Archive process

All levels of SMILE data will be archived in both GSS and ESAC archives. GSS and ESAC will share all the archived data.

The data archiving process is as follows:

1. ESAC receives, validates and ingests the science data products of the UVI and SXI instruments and delivers these to SAS.
2. SAS validates these data and transfers them together with LIA and MAG products to GSS for archiving and distribution.
3. ESAC will get all the archived files from GSS (excluding UVI and SXI that are already in the ESAC database).

7 Management

7.1 Procurement scheme

ESA and CAS share the overall responsibility for developing, implementing, qualifying, procuring, launching and operating as required all space and ground segment elements necessary to fulfil the mission and scientific objectives laid out above. Responsibilities are defined in the Implementing Arrangement approved by ESA Council (ESA/C(2016)113) between ESA and NSSC/CAS and are shown on Figure 43. Both parties are responsible for the development and tasks of the elements under their respective responsibility, by following their own standards and procedures for all aspects, i.e. ECSS for ESA, incl. PA and CAS standards for CAS provisions. This requires clear and separate technical and management interfaces and has been a driver in defining the roles of each partner.

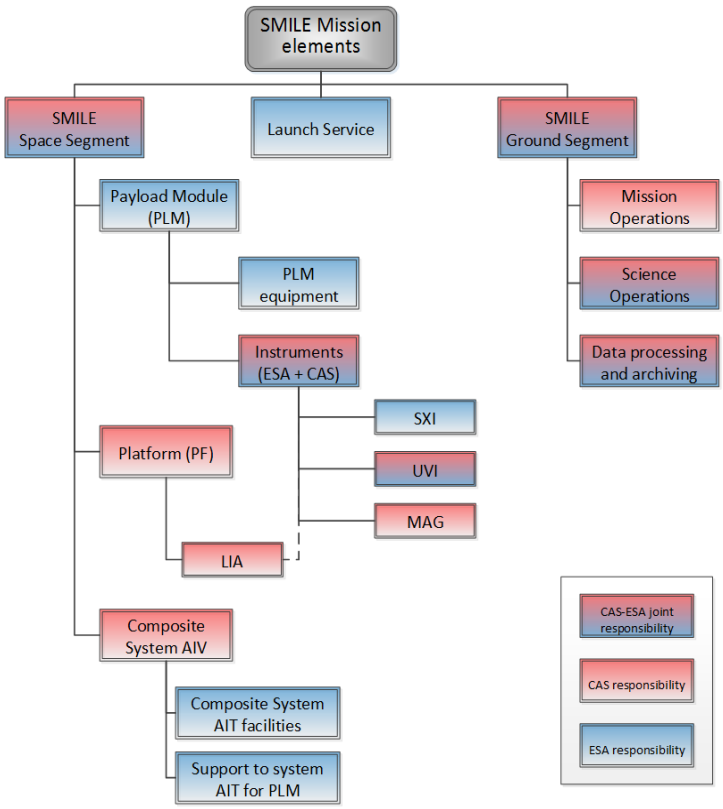

Figure 43. CAS (red) and ESA (blue) responsibilities. Red-blue boxes show shared responsibilities

ESA's responsibilities are:

- Develop and qualify the SXI and UVI instruments (provision from the ESA Member States), with participation of NSSC;
- Provide and operate the test facilities in Europe where the System AIT will be performed;
- Provide the launch services for the SMILE Space Segment Composite;
- Perform the SMILE Launch Campaign, with the support of NSSC and the PLM contractor for all activities related to the PF and the PLM;
- Contribute to the Mission and Science Operations Centre;
- Lead the joint review for Qualification and Flight Acceptance.

The Payload Module procurement follows standard practices in ESA but particularly tailored to a fast-track mission similarly to CHEOPS. The Industrial Policy Committee approved the PLM procurement in 2016, based on a definition phase (A/B) following an Invitation To Tender. This phase will end with the delivery of

the PLM PDR Data Package and updated proposal for the implementation phase (C/D/E1), including cost at a Firm Fixed Price. Three of the Prime Contractors are currently in competition through the definition phase. The PLM PDR takes place in December 2018 – April 2019 and the implementation phase is subject to Mission Adoption by the SPC. The PLM Contractor will be selected after Mission Adoption in spring 2019. ESA will also procure the launcher and the launch services as well as the spacecraft-level test facilities and services in Europe. The current foreseen test facilities are in ESTEC. All PLM-related activities throughout the spacecraft-level integration and tests will be under the responsibility of ESA and the European PLM Contractor.
Procurement of time-critical components (sensors, EEE, radiation hard and high reliability parts, and other long lead items) needs to start early and in sufficient quantities (i.e. including spare items) to alleviate the possibility that late deliveries jeopardise the schedule.

CAS's responsibilities are:

- Develop and qualify the Platform (PF);
- Develop and qualify the LIA and MAG instruments, with participation of European teams;
- Perform the System AIT, with the support of ESA for operating the test facilities and for PLM related activities;
- Provide the Mission and Science Operations Centre;
- Perform the operations of the SMILE spacecraft after its separation from the launcher and during the entire operational Phase which includes ensuring compliance to the Space Debris mitigation requirements;
- Lead the Mission PDR and CDR, including for the Ground Segment.

The interfaces have been simplified as much as possible which for example explains why the PLM duplicates some of the platform functions, e.g. computer, power distribution. All interfaces are managed and controlled through interface requirements and control documents (IRD and ICD) including through definition phase. The ICDs will be formally agreed, signed, and change control implemented before or latest by Mission PDR.

The interfaces with the instruments will be managed through the standard Experiment Interface Documents usually specified at the interface of payload and platform for science missions. A similar interface requirements document has been produced for all interfaces involved in this mission:

- Spacecraft (CAS/ESA) - Launcher (ESA/Arianespace)
- Platform (CAS/IAMC) – PLM (ESA/Contractor)
- PLM (ESA/Contractor) – Instruments (SXI, UVI, & CAS for MAG/LIA)
- Space to Ground (S-band & X-band) (ESA & CAS)
- Ground to Ground (ESA MOC/SOC & CAS-GSS/CCC/SAS)

ESA National agencies, CAS and CSA will provide all the scientific instruments. *Table 24* shows the institutions with a planned hardware contribution to the SMILE payload and their responsibility within the instrument consortia. In addition to hardware provision, the national agencies will support instrument operations, data calibration and data processing, at least through the nominal phase of the mission.

Instrument	PI	Co-PI
LIA	L. Dai (NSSC, CAS, China)	D. Kataria (MSSL, UK)
MAG	L. Li (NSSC, CAS, China)	R. Nakamura (IWF, Austria)
SXI	S. Sembay (Leicester U., UK)	F. Wei (NSSC, CAS, China)
UVI	E. Donovan (Calgary U., Canada)	J. Wang (PRIC, China)

Table 24 PI and Co-PIs of the SMILE payload

7.2 Project management

7.2.1 ESA management

Once the SMILE mission is confirmed for implementation by both parties (ESA SPC adoption and CAS confirmation of the mission implementation), a project team is formally appointed for the mission implementation, led by a Project Manager. Following in-orbit commissioning, the Project is generally handed over to a Mission Manager, who will be appointed for conducting the ESA part of the mission operations from the end of the commissioning phase until the end of the mission.

The SMILE Project Manager is charged with the overall responsibility for the management, implementation and execution of all technical and programmatic aspects of the mission that are under ESA responsibility. As such s/he is the formal point of contact at project level for CAS. The SMILE Project Manager directly reports to SCI-F Head of Department.

The SMILE Project Scientist, is in charge of all scientific aspects including monitoring of the science performance and interface with the science community. He directly reports to SCI-S Head of Office.

The Project Team supports the Project Manager in fulfilling his/her tasks and is constituted of the following key people:

- The System Engineer, in charge of the overall monitoring and control of the mission requirements, performances and interfaces, in particular for what concerns the PLM, but also with the launcher;
- The Payload Manager, in charge of the monitoring and control of the instruments activities (design, schedule, interfaces, AIV, …);
- The Assembly, Integration and Verification Manager, in charge of all AIT activities,
- The Science Operations Manager

Furthermore:

- A Product Assurance Manager, from ESA Directorate of Technical and Quality management, supports the Project Manager for all quality aspects and ensures the work is executed in accordance to ESA quality standards.
- A number of engineer experts from ESA Directorate of Technical and Quality management, covering the various technical domains, provide regular support to the Project Team on the Project Manager request,
- Experts from the Directorate of Operations support the Project for all matters related to the spacecraft operations or the mission profile.

7.2.2 CAS management

The chief commander of Steering Committee of Space Science Program (SCSSP) will be the vice president of CAS, who is in charge of all the space science missions of CAS. The vice chief commander of SCSSP is the general director of NSSC, who is responsible for the space science mission selection and execution. The top level leadership of SMILE mission, including Chief Scientist (CS), Chief Engineer (CE) and Vice Chief Commander (VCC) will be appointed by CAS.

The Chief Scientist is responsible for achieving the scientific goal of SMILE mission and monitor the quality, plan of the project to satisfy the scientific requirements.

The Chief Engineer will lead the implementation of the hardware development to achieve the SMILE engineering goals, will coordinate the interface between the systems, and identify the key technology and risk of the project.

The Vice Chief Commander is responsible for quality control, plan, rate of progress, funds, and coordinates the institute which are responsible for the development of the systems.

NSSC has already established a SMILE Project Management Office (SPMO) and the project manager is already appointed by NSSC, he is also the contact point for the CAS part.

SMPO is under the control of the Chief Scientist, Chief Engineer and Vice Chief Commander and execute all of the decisions made by them. It will be the contact with ESA and manage all the affairs of the project management.

The SMILE project of CAS consists of four systems, namely satellite system, Science Application System (SAS), TT&C system and Ground Support System (GSS).

System Engineers are in charge of the system design, system key technology, risk, system quality and system AIT.

7.3 Programme participation

The possible modes of participation to the SMILE programme are:

(1) **Mission Co-Principal Investigator** (Mission Co-PI), heading the mission proposal to ESA and CAS and coordinating science activities within the SMILE mission and community;

(2) **Principal Investigator** (PI), heading a consortium providing an instrument;

(3) **Co-Principal Investigator** (Co-PI) may be appointed if a major development is carried out in a country/institution different from the one of the PI; A Co-PI will have similar rights as a PI, but the PI will remain the formal interface to the SMILE ESA and CAS project teams;

(4) **Co-Investigator** (Co-I), a member of an instrument consortium;

(5) **Guest Investigator** (GI), a scientist participating in the data collection and/or analysis of one or more instruments and/or performing laboratory studies, theoretical or numerical investigations essential for the mission success.

7.4 Science management

ESA and CAS will each appoint a **Project Scientist** (PS) on SMILE, who will jointly be responsible for all scientific issues within the Project, including the interface with the scientific community.

The PSs will support the project aiming at maximising the scientific performance, within the mission programmatic boundaries. The PSs will co-chair a joint Science Working Team (SWT) and coordinate its activities. During the implementation phase, the two PSs will advise the ESA and CAS Project Managers on technical matters affecting the scientific performance. The PSs will monitor the state of implementation and readiness of the instrument operations and scientific data processing infrastructure. During the operational phase, i.e. after in-flight commissioning, the PSs will continue to act as the main interface with the scientific community, will support the planning of scientific payload operations in conjunction with relevant PIs, and will monitor the adequate creation of scientific products, their archiving and distribution to the scientific community.

The members of the SMILE **Science Working Team** (SWT) will be the ESA and CAS SMILE PSs, the Principal Investigators, and the SMILE mission Co-PIs. Co-Investigators, Guest Investigators, and other interested scientists will be invited to participate in SWT meetings, as appropriate. The PSs will co-chair the SWT.

The SWT will monitor and advise ESA and CAS on all aspects of the SMILE mission that will affect its scientific performance. It will assist the PSs in maximising the overall scientific return of the mission within the established boundary conditions. It will act as a focus for the interests of the scientific community in SMILE.

Five working groups have been established in order to support the SMILE Science Study Team in ensuring that the mission science objectives are achieved and optimised, and in adding value to SMILE science through the contributions of complementary measurements on the ground and in space.

These are:

- In Situ working group: The activity of this working group is centred on optimising the design, operations and calibrations planning of the in-situ instrument package. A report reviewing science objectives, pointing and measurement accuracy requirements, operational modes, calibration plans and data products is being prepared.

- Data Formats and calibration working group: his tasks are to define the formats to be used in data deliveries from the PI teams and to the user community as well as to prepare the calibration activities to be performed once SMILE will be in orbit.

- Ground-Based and Additional Science working group: it will coordinate and encourage support for SMILE in the ground-based Solar-Terrestrial Physics community, ultimately with the aim of maximising the uptake of the data and therefore also maximising the science output. It will coordinate future joint observation campaigns (e.g. with EISCAT 3D, SuperDARN) and produce a suitable interface to combine disparate ground-based and additional science data with SMILE data into a common workable format.

- Outreach working group: his activities are to contact organisations promoting science in primary and secondary schools, to hold workshops promoting careers in science, focusing on SMILE as a practical example of how space projects are developed, and to encourage pupils to follow its progress up to launch and beyond.

- Modelling working group: the aims are to coordinate and drive the simulation and modelling activities ongoing in many SMILE collaborating institutes and leading to predict the soft X-ray images which SXI will generate. This work, simulating the changes which can be expected in magnetospheric boundary locations under differing solar wind conditions, coupled with investigations of how to extract magnetospheric boundary and cusp positions, is essential in order to optimise the SXI observing strategy once SMILE is operational.

7.5 Schedule

As a standard practice, verification will be performed at lower levels first, i.e. equipment and instruments, then at PLM and platform levels and finally at spacecraft level. The mission programmatic constraints impose a fast-track approach. The instrument flight model is foreseen to be delivered 3 years after adoption, the full payload module including instruments ~ 4 years after adoption. The launch is planned 5 years after adoption. In order to verify interfaces but also to increase efficiency a minimal number of deliveries will be made to China, i.e. PLM STM to CAS for spacecraft STM tests in China and exchanges of PLM and platform simulators. No other hardware will be delivered outside of Europe. The high-level schedule is depicted on Figure 44.

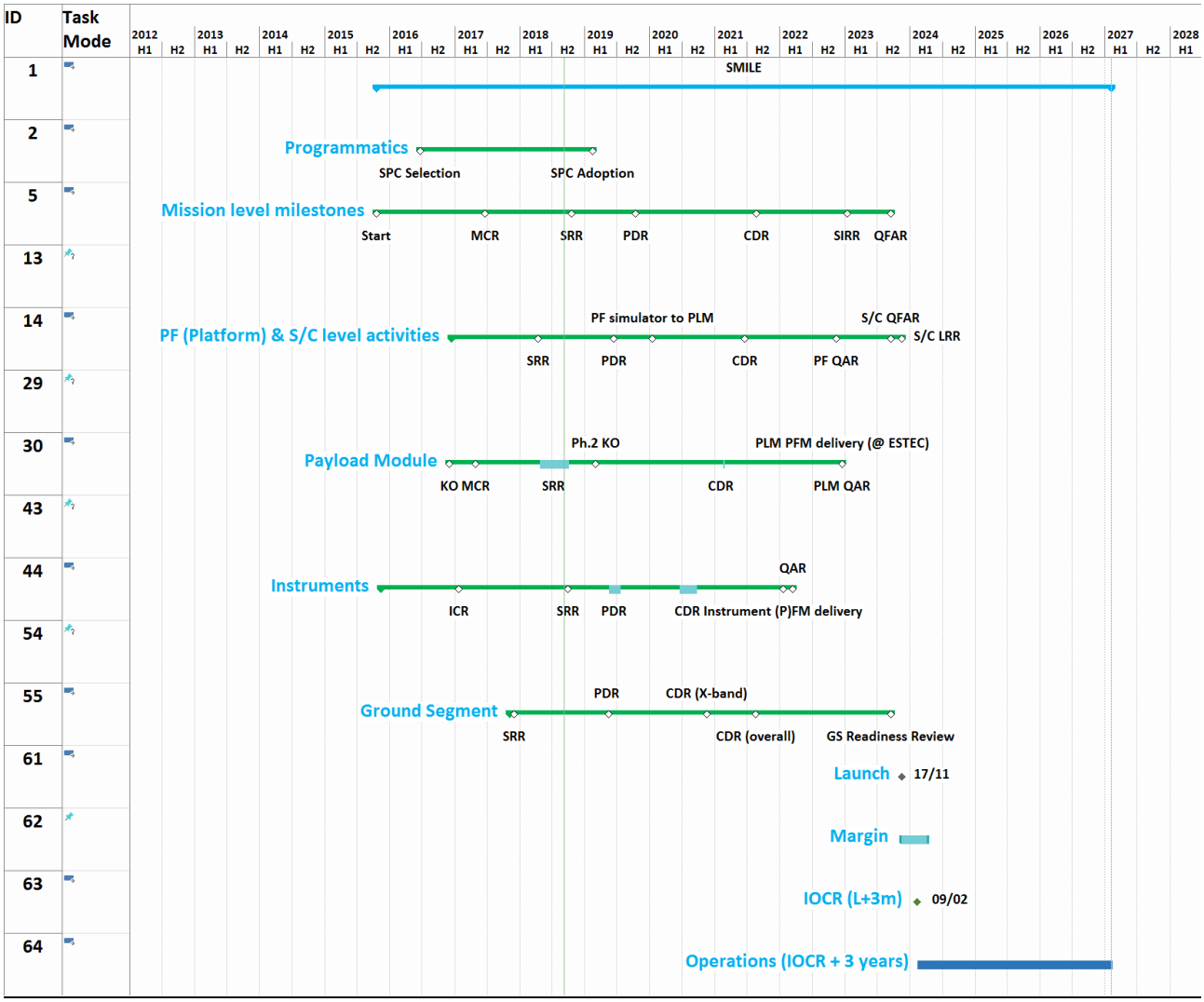

Figure 44. SMILE Mission schedule

7.6 Data rights

Reduction of science data is under the responsibility of PI teams. According to the Implementing Arrangement approved between ESA and NSSC/CAS (ESA/C(2016)113) the PIs instruments retain exclusive data rights for the purpose of calibration and verification for a period of 1 year after the receipt of the original science telemetry and auxiliary orbit, attitude and spacecraft status information. By the 1-year deadline, the PIs will provide calibrated and verified data, with all relevant information on calibration and instrument properties, to ESA and CAS. The ESA and CAS science data archives will be the repository of all mission products.

The PI teams will also be required to share data with the GIs (see Section 7.3) as needed, also during the proprietary period, so as to enhance the scientific return from the mission. The PI teams will provide ESA and CAS (and where applicable, the Lead Funding Agencies) with processed and useable data for Science Communication purposes as soon as possible after their receipt.

8 Communication and Public Engagement

The database of SMILE observations will be an unparalleled resource providing a global view and a direct measure of the response of the Earth' magnetospheric system, from its outer dayside boundaries to deep into the ionosphere, under the influx of the solar wind, and especially of changes in the wind conditions. As such it will constitute a golden reference data bank for validation of solar-terrestrial interaction models and for understanding space weather effects. Moreover, the visual nature of SMILE imaging data will be particularly effective in attracting the general public, young and old, school children and non-experts, by making visible for the first time complicated physical processes which are difficult to grasp being essentially invisible to the naked eye. SMILE has the potential to revolutionise the general understanding of solar-terrestrial interactions and of space weather by providing 'X-ray' images of the magnetospheric bubble shielding our Earth from inclement solar wind conditions.

Communication, with both the scientific community and the public, will be paramount in order to maximise the exploitation of SMILE observations. According to ESA and CAS policies all processed and calibrated SMILE data will be made public after one-year proprietary period; the instrument teams are actually considering releasing the data earlier than that, in order to build up and cultivate a strong interest and engagement by the scientific community. Space weather, magnetospheric plasma and planetary science communities all will be keen and welcome to examine and participate in the interpretation of these data, as well as in applying them to the validation of global models, in a manner never realised so far. Astrophysicists may take advantage of SMILE observations to estimate the level of magnetosheath X-ray signal that needs to be taken into account when observing the Universe through it.

The nature of the SMILE data (in particular X-ray images of magnetic boundaries normally invisible, and associated UV views of the auroral oval) will catch the imagination of the general public and lend much weight to outreach purposes.

The solar-terrestrial plasma interaction can have a dramatic and potentially dangerous impact on society. Space weather affects life in many ways – e.g. overloading power transmission grids, enhancing pipeline corrosion, interfering with commercial air travel communications, causing anomalies on satellites that underpin key infrastructure such as global positioning systems and communication systems, and endangering the health of people travelling on trans-polar flights and in space – both as part of national and international space programmes and, now growing ever faster, as a commercial activity. It is therefore crucial for the specialists in the field to effectively and inclusively communicate their research in this area to the world. However, as already said, the key obstacle to effective communication is that solar-terrestrial physics involves the study of processes which are, except for the aurora and the solar corona during eclipse, invisible to the naked eye. Furthermore, many of the physical processes at the heart of space plasma physics do not easily relate to everyday experience.

SMILE has the potential to revolutionise the world public's understanding of solar-terrestrial physics by providing an "X-ray" of the magnetosphere surrounding our Earth. Magnificent images (such as those in Figure 12) and movies showing the solar wind interacting with the magnetosphere will constitute a natural hook through which the general public of all ages can engage with space science, and will open a path by which more complex ideas can be disseminated and thus used to improve scientific literacy and education the world over. The SMILE websites (at ESA, CAS, and the hardware institutes) will be the central focus of the SMILE communication and outreach programme. All images and videos will be made freely available as soon as possible (and the data, as explained above). Different portals will target different communities: the general public, school children, the broader scientific community and the space plasma physics community itself, for example.

Preparations for this activity have already started: SMILE dedicated websites have been setup and a SMILE promotional video produced by CAS/NSSC has been posted; a database of images and videos recording the development phase of SMILE has been created; contacts have been established with primary and secondary schools, especially some with 'special needs' where contributions towards science activities, lessons/workshops and the opportunity to work on SMILE-related projects are particularly sought after because of the shortage of science teachers; funding applications have also been submitted to support these activities. Efforts are on-going to involve older pupils in the analysis of real science data, so that these pupils

may run a short research programme, in collaboration with a university researcher. A children book telling the story of a girl finding out about the Sun's activity, already in many languages, is being translated from Spanish into Chinese; SMILE team members often take up opportunities to present the mission not only to scientific, but also amateur and public gatherings. SMILE outreach momentum is definitely on the way up!

9 References

Aguilar-Rodriguez, E., et al. Adv. Space Res., 38, 522, 2006

Angel, J. R. P. ApJ, 233, 364, 1979

Angelopoulos, V. et al. Science, 321, 931, 2008

Bodewits, D. et al. A&A, 469, 1183, 2007

Borovsky, J. E. et al. J.Geophys.Res., 98, 3807, 1993

Boudouridis, A., et al. J. Geophys. Res., 108, doi: 10.1029/2002JA009373, 2003

Burch, J.L. et al. Space Sci. Rev., DOI 10.1007/s11214-015-0164-9, 2015

Cargill, P. J. et al. Space Sci. Rev., 118, 321, 2005

Carter, J.A., S. Sembay, A.M. Read Astron. Astrophys. 527, 115, https://doi.org/10.1051/0004-6361/201015817, 2011

Chasapis, A. et al. Astrophys. J. Lett., 804, L1, 2015

Collier, M. R., & Connor, H. K. Journal of Geophysical Research, https://doi.org/10.1029/ 2018JA025763, 2018

Cravens, T.E. Geophys. Res. Lett. 24, 105–108, https://doi.org/10.1029/96GL03780, 1997

Cravens, T.E. et al. J. Geophys. Res. 106, 24883–24892, https://doi.org/10.1029/2000JA000461, 2001

Cravens, T. E. Science, 296, 1042, 2002

Eastwood, J. P. et al. Space Sci. Rev., doi: 10.1007/s11214-014-0050-x, 2015

Escoubet, C. P. et al. Ann. Geophys., 19, 1197, 2001

Escoubet, C. P., et al. J. Geophys. Res., 113, A07S13, doi:10.1029/2007JA012771, 2008

Finch, I. and Lockwood M. Ann. Geophys., 25, 495, 2007

Forbes, T. G. J. Geophys. Res. 105, 23153, 2000

Frey, H. U. et al. Nature, 426, 533, 2003

Gonzalez, W. D. Planet. Space Sci. 38, 627, 1990

Gonzalez, W. D. et al. Space Sci. Rev. 88, 529, 1999

Goodrich, C.C. et al., Geophys. Res. Lett. 25, 14, 2537, 1998

Henderson, M. G., Ph.D. thesis, University of Calgary, 1994

Henderson, M. G., and et al. J. Geophys. Res., 111, A06206, doi: 10.1029/2005JA011366, 2006

Hsu, T.-S. and R. L. McPherron, J. Geophys. Res., 107, 1398, 2002

Hu, Y. Q., et al. J. Geophys. Res. 112, A07215, doi:10.1029/2006JA012145, 2007

Huang, C.-S. Geophys. Res. Lett. 29, 2189, doi:10.1029/2002GL016162, 2002

Hubert, B., et al. Geophys. Res. Lett. 33, L10105, doi: 10.1029/2006GL026008, 2006

Hubert, B. et al., J. Geophys. Res. 114, A07211, doi:10.1029/2008JA013813, 2009

Johnstone A. D. et al. Space Sci. Rev., 79, 351, 1997

Jorgensen A. M., et al. Journal of Geophysical Research: Space Physics, under review, 2018

Kalmoni, N.M.E. et al. Nature Coms, DOI: 10.1038/s41467-018-07086-0, 2018

Koutroumpa, D. et al. A&A, 475, 901, 2007

Kozyra, J. U., et al. J. Geophys. Res. Space Physics, 119, 5401–5448, doi:10.1002/ 2013JA019748, 2014

Kuntz, K. et al. IACHEC Meeting, 2014 (http://web.mit.edu/iachec)

Kuntz, K.D. et al. Astrophys. J. 808, https://doi.org/10.1088/ 0004-637X/808/2/143, 2015

Lee, L. C. and Z. F. Fu Geophys. Res. Lett., 12, 105, 1985

Lisse, C.M. et al. Science 274, 205–209, https://doi.org/10.1126/science.274.5285.205,,1996

Liu, Z. X. Annales Geophysicae, 23, 2707, 2005

Lyons, L. R. et al. J. Geophys. Res. 102, 27039,1997

Lui, A. Space Sci Rev 113, 127. https://doi.org/10.1023/B:SPAC.0000042942.00362.4e, 2004

Mauk, B.H., et al. Space Sci Rev 179: 3. https://doi.org/10.1007/s11214-012-9908-y, 2013

Merka, J. et al. J. Geophys. Res. Space Phys. 110, https://doi.org/10.1029/2004JA010944, 2005

Milan, S. E. et al. Ann. Geophys. 21, 1121, 2003

Milan, S. E., et al. J. Geophys. Res. 109, A04220, doi: 10.1029/2003JA010350, 2004

Milan, S. E., Geophys. Res. Lett., 36, L18101, doi: 10.1029/ 2009GL039997, 2009

Milan, S. E., et al. J. Geophys. Res. 845 117, doi:10.1029/2011JA017082, 2012

Miyoshi, Y., et al. Earth, Planets and Space, 70(1), 2018

Mukai, T., et al. J. Geomagn. Geoelectr., 46, 669–692, 1994.

Morley, S. K. and Freeman, M. P. Geophys. Res. Lett., 34, L08104, 2007

Motoba, T., et al. Geophys. Res. Lett., 39, L08108, doi: 10.1029/2012GL051599, 2012

Murphree, J. S.R A. et al. Space Sci. Rev. 70, 421, 1994

Newell, P. et al. J. Geophys. Res. 94, 8921, 1989

Newell, P., and C. Meng J. Geophys. Res., 99, 273–286, doi:10.1029/93JA02273, 1994

Omidi, N. and Sibeck, D. G. Geophys. Res. Lett. 34, L04106, 2007

Palmroth, M. et al. J. Geophys. Res. 106, 29435, 2001

Phan, T. D. et al. Ann. Geophys. 22(7), 2355, 2004

Pitout, F. et al., Ann. Geophys., 24, 1–16, 2006

Raeder, J. Ann. Geophys. 24, 381, 2006

Raeder, J. et al. Space Sci. Rev., 141, 535-555, doi: 10.1007/s11214-008-9421-5, 2008

Richardson, I. G. et al. Geophys. Res. Lett. 28, 2569, 2001

Robertson, I. P. and Cravens, T. E. Geophys. Res. Lett. 30(8), 1439, 2003a

Robertson, I. P. and Cravens, T. E. J. Geophys. Res. 108(A10), 8031, 2003b

Robertson, I. P. et al. J. Geophys. Res. 111, A12105, 2006

Rodrigues, P. et al. AstroBus Small: an Upgraded Multimission Microsatellite Platform. The 4S Symposium, 2012

Russell, C. T. and Elphic, R. C. Space Sci. Rev., 22, 681, 1978

Samsonov, A. A., et al. J. Geophys. Res. Space Physics, 121, 6493–6508, doi: 10.1002/2016JA022471, 2016

Samsonov, A. A., et al. Geophysical Research Letters, 44, 9159–9166. https://doi.org/10.1002/2017GL075020, 2017

Samsonov, A. A., et al. Journal of Geophysical Research: 123, 3727–3741, https://doi.org/10.1029/2017JA025174, 2018

Scholer, M., Geophys. Res. Lett. 15, 291, 1988

Sembay, S. IACHEC Meeting, 2014 (http://web.mit.edu/iachec)

Shue, J.-H. et al. J. Geophys. Res. 102, No. A5, 9497, 1997

Sibeck, D. et al. Space Sci Rev, 214:79, https://doi.org/10.1007/s11214-018-0504-7, 2018

Smith, M. F. and Lockwood, M. Rev. Geophys., 34, 233, 1996

Snowden, S. L. et al. Astrophys. J. 610, 1182, 2004

Snowden, S. L. et al. Astrophys. J., 691, 372, 2009

Song, P. and Russell, C. T. J. Geophys. Res., 97(A2), 1411, 1992

Southwood, D. J. et al. Planet. Space Sci. 36, 503, 1988

Sun, T. R. et al. J. Geophys. Res. Space Physics, 120, doi:10.1002/2014JA020497, 2015

Taguchi, S. et al. J. Geophys. Res. 114, A02311, 2009

Torr, M. R. et al. Space Science Reviews, 71, 329, 1995

Turc, L., et al. Ann. Geophys., 32, 1247–1261, doi:10.5194/angeo-32-1247-2014, 2014

Yamauchi, M. et al. J. Geophys. Res., 101, 24675, 1996

Wang, C. et al. Science China, 56: 1141, doi: 10.1007/s11430-013-4608-3, 2013

Wild, J. A. et al. Ann. Geophys. 27, 3559, 2009

Wang, Y., et al. J. Geophys. Res. Space Physics, 118, 2173–2184, doi: 10.1002/jgra.50226., 2013

10 List of Acronyms

ADS	Analyser-Detector Subsystem
BOL	Beginning of Life
CAS	Chinese Academy of Sciences
CCD	Charge Coupled Device
CME	Coronal Mass Ejection
CMOS	Complementary Metal-Oxide Semiconductor
CSA	Canadian Space Agency
CTI	Charge Transfer Inefficiency
CX	Charge eXchange
DPU	Digital Processing Unit
EA	Electrostatic Analyser
EPIC	European Photon Imaging Camera
ESA	European Space Agency
FDS	FOV Deflector System
FOV	Field Of View
FWHM	Full Width Half Maximum
GNC	Guidance, Navigation and Control
GNSS	Global Navigation Satellite System
IMF	Interplanetary Magnetic Field
L1	Level-1 data
L2	Level-2 data
L3	Level-3 data
L4	Level-4 data
LBH	Lyman-Birge-Hopfield
LEPIC	Low Energy Plasma Instrument Calibration
LIA	Light Ion Analyser
LLBTF	Leicester Long Beam-line Test Facility
MAG	MAGnetometer
MCP	MicroChannel Plate
MOC	Mission Operation Centre
MSSL	Mullard Space Science Laboratory
MIXS	Mercury Imaging X-ray Spectrometer
NSSC	National Space Science Center
OOT	Out-Of_Time
PCDU	Power Control and Distribution Unit
PF	Platform
PLM	Payload Module
PRIC	Polar Research Institute of China
PSF	Point Spread Function
QE	Quantum Efficiency
QL	Quicklook
SAS	Science Application System
SCSSP	Steering Committee of Space Science Program
SMILE	Solar wind Magnetosphere Ionosphere Link Explorer
SNR	Signal to Noise Ratio
SOC	Science Operation Centre
SSDC	SMILE Science Data Centre
SWCX	Solar Wind Charge eXchange
SXI	Soft X-ray Imager
TEC	ThermoElectric Cooler
TRL	Technology Readiness Level
UCL	University College London
UofC	University of Calgary
UoL	University of Leicester
UVI	UltraViolet Imager
VGFS	Variable Geometric Factor System

11 Annex 1

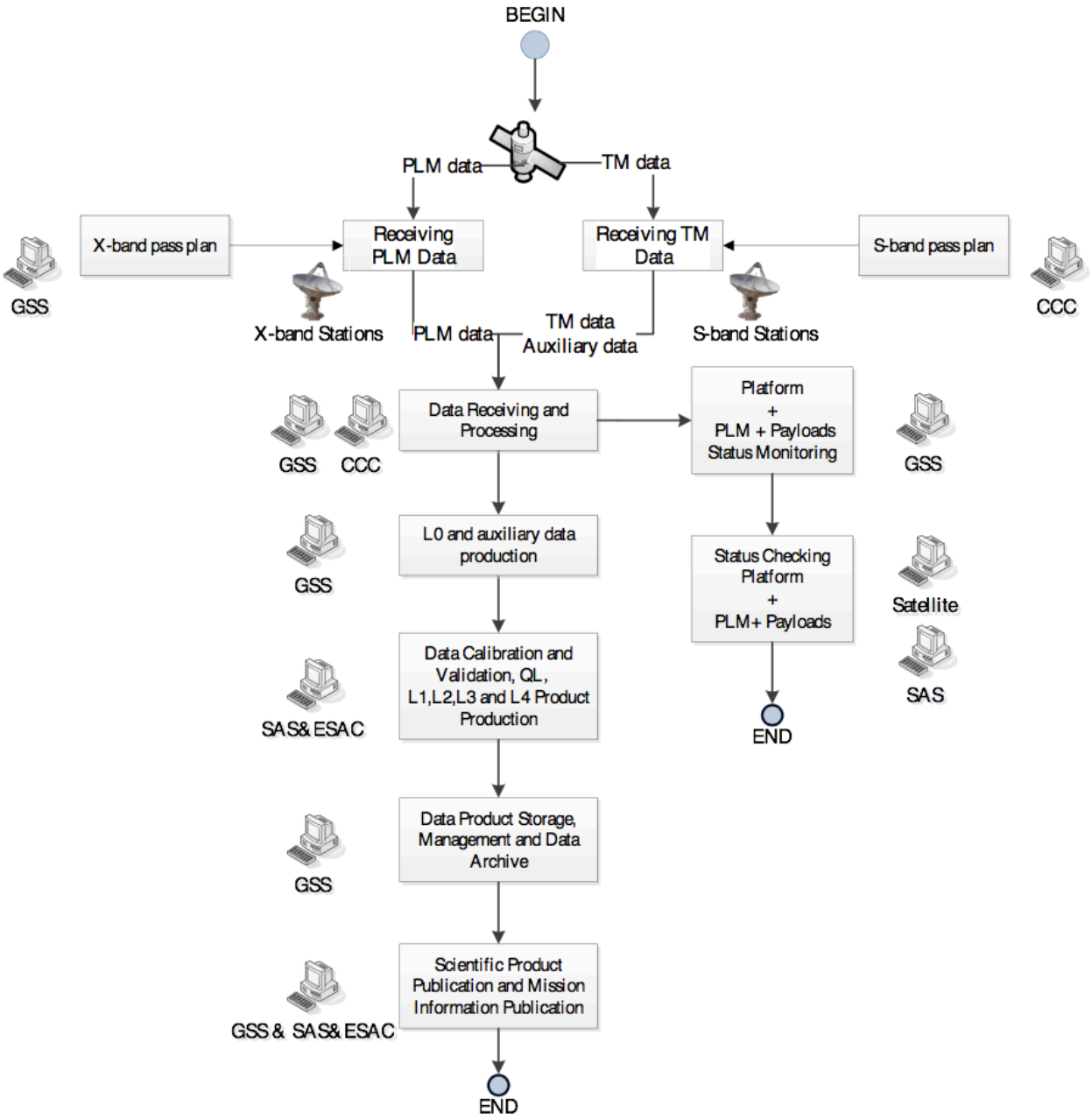

Figure 45. SMILE Mission downlink processes.

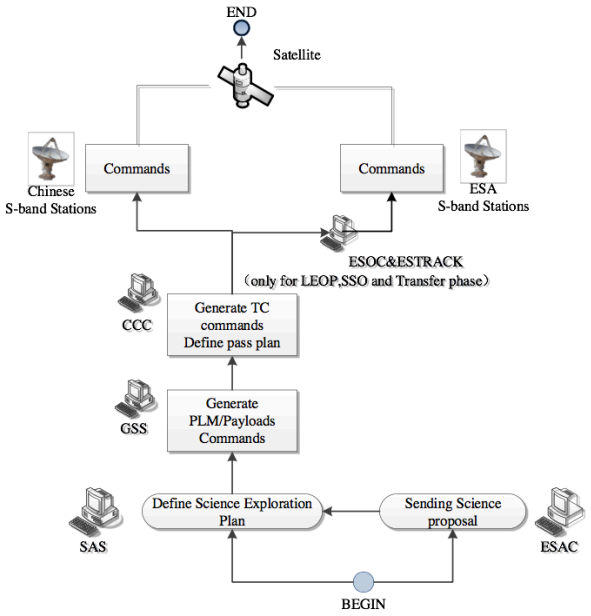

Figure 46. SMILE Mission uplink processes

Emergency command uplink to spacecraft

In the event of a satellite emergency, CCC has the rights and responsibilities to take actions to handle the emergency. CCC has the responsibility to ensure the immediate health and safety of the spacecraft according to pre-defined operational procedures. When emergencies happen, engineers from satellite system, CCC, GSS, SAS, ESAC and PI teams shall all be involved to determine what actions should be taken to recover from the emergency situation (Figure 47).

Figure 47. SMILE Emergency uplink process.